Improved radiative corrections to $(e, e'p)$ experiments and their impact on Rosenbluth measurements

Inauguraldissertation

zur

Erlangung der Würde eines Doktors der Philosophie

vorgelegt der

Philosophisch–Naturwissenschaftlichen Fakultät

der Universität Basel

von

Florian Weissbach

aus Berlin, Bundesrepublik Deutschland

Basel, 2006

Genehmigt von der Philosophisch-Naturwissenschaftlichen Fakultät
auf Antrag von:

Prof. Dr. Dirk Trautmann

Basel, den 02. Mai 2006

Prof. Dr. Hans-Jakob Wirz
Dekan

Don't panic!

Douglas Adams, The Hitchhiker's Guide to the Galaxy

Contents

Preface

This thesis is about QED effects occurring in electron scattering experiments. There is a strong electron scattering community at Basel University and thus a strong demand for high precision data analysis and for simulations. These simulations are the experimental physicists' mean to control all aspects of their electron scattering experiments. Among those effects which need to be fully understood in order to achieve the highest possible accuracy in $(e, e'p)$ experiments are *radiative corrections*.

While we do not want to anticipate the introductory comments on the importance of $(e, e'p)$ experiments and the corrections to them from Chap. 1, we do state here on a preliminary note that radiative corrections are important in electron scattering experiments since they alter the four-momenta of all particles involved. Analyzing such experiments involves unfolding the data from these radiative processes in order to get back the vertex values of the particles' four-momenta.

This thesis is organized as follows:

Its main part is about improving $(e, e'p)$ radiative corrections. After an introduction to $(e, e'p)$ experiments and to radiative corrections, we will calculate in Chap. 2 the multi-photon emission cross section using the soft-photon approximation (SPA) and the peaking approximation. And we will present the exact single-photon bremsstrahlung result. In Chap. 3 we will remove the two approximations mentioned above from the calculations (i) by introducing a full angular Monte Carlo computation not using the peaking approximation any more; and (ii) by introducing another Monte Carlo computation removing partially also the SPA from $(e, e'p)$ data analyses. In Chap. 4 we will present our results, testing them by inserting our Monte Carlo routines into a standard $(e, e'p)$ data analysis code from the Thomas Jefferson National Accelerator Facility (TJNAF).

In Chap. 5 of this thesis we will apply our improved radiative corrections treatment to cross section measurements using the so-called Rosenbluth technique. After reviewing the much discussed discrepancy in the measurements of the proton electric form factor G_{ep}, we will present our results, discussing the impact of the improved radiative corrections onto the G_{ep}-problem.

In Chap. 6 we will review our results, present the conclusions and we will give an outlook, focussing especially on further possible applications in connection with the G_{ep}-discrepancy, namely radiative corrections to e^+e^- collider experiments.

Some of the content of this thesis has been published in nucl–th/0411033 * and is submitted for publication. More papers are in preparation and will be submitted soon.

*Please visit `http://www.arxiv.org/abs/nucl-th/0411033`.

1 Introduction

$(e, e'p)$ experiments are an important experimental tool in the rich and diverse field of nuclear physics. In this introduction we shed light on the importance of $(e, e'p)$ experiments. And we introduce radiative corrections to these experiments. Radiative corrections are part of each $(e, e'p)$ state-of-the-art data analysis. But most data analysis procedures include these important corrections only approximately. The two most important approximations are introduced in this chapter.

1.1 Why $(e, e'p)$ experiments?

Electron scattering experiments with just the scattered electron being detected are called *inclusive* experiments, or (e, e') experiments in nuclear physics nomenclature. *Exclusive* scattering experiments detect more particles. In so-called $(e, e'p)$ experiments, which are subject of this thesis, the scattered electron with momentum $k' = (\epsilon', \mathbf{k}')$ is measured in coincidence with the ejected proton, which has momentum $p' = ({p'}^0, \mathbf{p}')$ (see Fig. 1.1). The momentum transfer between the incident electron with momentum $k = (\epsilon, \mathbf{k})$ and the target proton is $q = k - k' = (\nu, \mathbf{q})$. The unobserved recoiling system bears the 'missing momentum' $\mathbf{p}_\mathrm{m} = \mathbf{p}' - \mathbf{q}$. And the 'missing energy' is $E_\mathrm{m} = T_\mathrm{p} + T_\mathrm{r} - \nu$, where T_p is the kinetic energy of the proton and T_r is the kinetic energy of the $(A-1)$ system. Here, A is the atomic mass number of the target material. The $(A-1)$ system is the target nucleus deprived of the proton which was struck by the exchanged virtual photon (see Fig. 1.1).*

The $(e, e'p)$ experiments considered in this thesis neither use polarized beams nor do they measure polarizations of the final state.†

An important tool for $(e, e'p)$ analysis is the plane wave impulse approximation (PWIA). It assumes the struck proton not to interact with the $(A-1)$ system subsequently to the absorption of the exchanged virtual photon. In PWIA the

*Hence, sometimes the symbol $(e, e'p)$ is extended to $A(e, e'p)(A-1)$.

†Only in Chap. 5 we will briefly discuss $\mathrm{H}(\vec{e}, e'\vec{p})$ polarization transfer experiments in connection with the G_ep-problem.

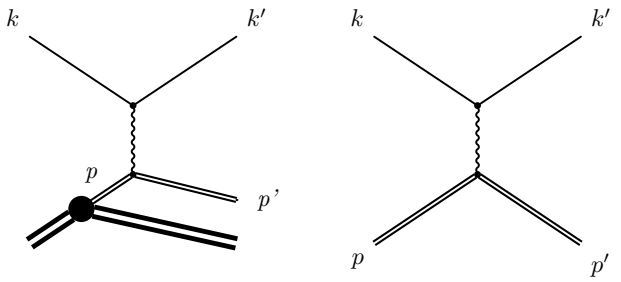

Figure 1.1: First-order Feynman diagrams for $A(e,e'p)(A-1)$ (left) and for $\mathrm{H}(e,e'p)$ (right) scattering. The thick line depicts the target nucleus (atomic number A) before and the recoiling $(A-1)$ system after a proton from the nucleus absorbed a virtual photon. In this simple picture the nucleus is assumed to be a 'spectator nucleus' since there is no interaction between the struck proton and the $(A-1)$ system. This approximation is called PWIA (see description in the text for details).

$(e,e'p)$ cross section factorizes, and we obtain

$$\frac{d\sigma}{d^3\Omega_\mathrm{e} d^3\Omega_\mathrm{p}} = K\sigma_\mathrm{ep} S(\mathbf{p}_\mathrm{m}, E_\mathrm{m})\,, \tag{1.1}$$

where σ_ep is the elastic electron-proton cross section, K is a kinematic factor, and $S(\mathbf{p}_\mathrm{m}, E_\mathrm{m})$ is the nuclear spectral function. It describes the probability of finding a proton with momentum $\mathbf{p}_\mathrm{m}$ and removal energy E_m in the target nucleus.

Like most approximations, the PWIA is an over-simplification. It neglects the so-called final state interactions (FSI), *i.e.* the interaction of the proton with the $(A-1)$ system after the hard scattering process. FSI can be included approximatively using the distorted wave impulse approximation (DWIA) for medium and heavy nuclei [1]. The DWIA treats the interaction with the $(A-1)$ system via an optical potential. Its parameters are obtained by fitting it to elastic scattering data [2]. Further effects which have to be accounted for in $(e,e'p)$ data analysis are, *e.g.*, meson exchange currents (MEC), excited states, and bremsstrahlung effects. The main focus of this thesis are the latter corrections.

$(e,e'p)$ experiments have been carried out at many facilities among which are NIKHEF (The National Institute for Nuclear Physics and High Energy Physics) in the Netherlands, MIT-Bates (Bates Linear Accelerator Center), part of the LNS (Laboratory for Nuclear Science, MIT) in the U.S.A., Saclay ('Accélerateur linéaire d'électrons de Saclay') in France, MAMI (Mainz Microtron) in Germany, and and TJNAF (Thomas Jefferson National Accelerator Facility) in the U.S.A.. MAMI and TJNAF are still operational and there are plans to upgrade them.

Since coincidence techniques became available four decades ago, $(e, e'p)$ experiments have been carried out to study the rich phenomena exhibited by atomic nuclei from all over the nuclear chart. Measuring momenta and energies of both scattered electron and proton reveals more information about the studied nucleus than inclusive scattering, *e.g.* single-particle properties, few-nucleon system dynamics, systematics of electromagnetic excitations, and decay mechanisms of resonance states.

Some of the topics of nuclear structure studied via the $(e, e'p)$ reaction are:

- the validity of the independent particle shell model.
  DWIA mean-field single particle calculations describe the shape of the spectral function (1.1) well. But the absolute value of the measured spectral function consistently falls below these predictions. The ratio between the calculated and the measured spectral function is called the spectroscopic factor and for targets with atomic numbers $A > 4$ it is approximately 0.6. This discrepancy is believed to be due to many-body effects like correlations (*e.g.* short-range repulsion), shifting particles to higher missing energies and momenta [1–3].

- $N\,N$ correlations in few body systems.
  Can we still see $N\,N$ correlations in $(e, e'p)$ experiments or do we have to go for $(e, p'N...N)$ reactions? Recently, evidence for short-range correlations (SRC) has been found in $(e, e'p)$ experiments [4–7]. SRC manifest themselves in the high-momentum component of the nuclear wave function and are essential to provide the binding of the nucleus.

- model dependence of deuteron $N\,N$ data.
  D$(e, e'p)n$ measurements should give access to the $N\,N$ potential and the short-range $N\,N$ interaction. But at high missing momenta the model potentials become very sensitive to small variations. Experimental data in this region is dominated by reaction mechanism effects, obscuring the deuteron structure [1, 8]

- reaction mechanisms.
  The kinematic settings of $(e, e'p)$ reactions can be optimized such that the reaction can be assumed to be a one-body reaction, by *e.g.* choosing parallel kinematics. Still, there is evidence for two-body transverse currents, undermining the one-body character of the reaction [1, 9, 10].

- relativistic effects.
  There are several experiments exhibiting sensitivity to relativistic corrections. For instance, ^{16}O$(e, e'p)$ measurements of the longitudinal transverse

response function, R_{LT}, yielded discrepancies between data from NIKHEF [11] and Saclay [12], which only vanished after taking into account relativistic effects [13]. Another example for the importance of relativistic effects are D$(e,e'p)n$ experiments measuring the longitudinal transverse asymmetry, A_{LT}. These experiments indicated that non-relativistic calculations deviated from the data considerably, while partial incorporation of relativistic effects yielded results closer to the data [14]. Most of the effect turned out to be due to missing relativistic corrections to the eN cross section. Including relativistic effects in the nuclear wave function yielded minor corrections only.

- visibility of the quark degrees of freedom.
  Are the rich collective phenomena (rotations, vibrations, superconductivity) of nuclei also due to a noticeable quark degrees of freedom?

- colour transparency (CT).
  Do electron scattering experiments really probe 'white' quark states which could be less sensitive to FSI? This should lead to a unit 'transparency', which is the ratio of the measured cross section to the PWIA cross section. To date $(e,e'p)$ data do not indicate such a CT effect [1, 20, 21].

- effects of three-body forces (3BF).
  The $(e,e'p)$ reaction only marginally contributes to this field; but since 3BF effects receive a lot of attention in nuclear physics we mention them here. Basic properties of few- or many-body systems such as nuclei cannot be approximated by two-body interactions between all possible pairs of nucleons. Deviations from the two-body approximation are mainly due to a 3BF between nucleons [15–17] (see Fig. 1.2 for some of the 3BF diagrams). Already the triton is under-bound by roughly 1 MeV [18], if only taking into account the two-body force. The 3BF is not reducible to sequential two-body interactions [19].

The $(e,e'p)$ reaction also sheds light on the structure of the nucleons themselves and on their excited states. For the structure of the nucleon the important topics are:

- the G_{ep}-problem.
  How well do we know the proton electric form factor G_{ep}? [22] What are the reasons for the apparent discrepancy between G_{ep} from the H$(e,e'p)$ Rosenbluth technique and the H$(\vec{e},e'\vec{p})$ polarization transfer method?[‡] This much discussed phenomenon usually is ascribed to the two-photon exchange (TPE) contribution which is magnified by the Rosenbluth method.

[‡]In Chap. 5 we will give a short introduction to the Rosenbluth problem and the apparent discrepancy in the proton electric form factor data.

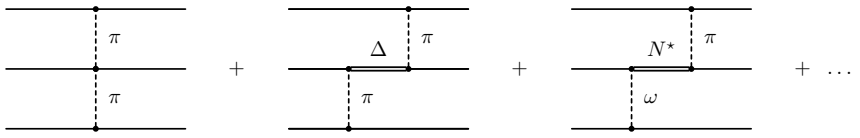

Figure 1.2: Some typical three-body force Feynman diagrams. The plain lines are nucleons, the dashed lines depict mesons like pions or ω-mesons. The nucleons can be scattered into excited states like the Δ or the $N^\star$, shown here as double lines.

- medium modifications.
  In addition to conventional many-body effects in nuclei there are medium modifications ('swelling of the nucleon'). It is hard to distinguish the two experimentally and it can only be done using models [1]. Also, FSI have to be carefully corrected for in order to see medium modifications [23].

- deformation of the Δ.
  Why are the results from $p(e,e'p)\pi^0$ experiments still far from perturbative quantumchromodynamics (pQCD) [1, 24]?[§]

These are some of the nuclear physics questions which can be tackled by means of $(e,e'p)$ experiments and, of course, also using other experimental techniques, including decays and hadronic probes, like (p,p'), $(d,{}^3\mathrm{He})$, (π,π'). This thesis aims at some aspects of $(e,e'p)$ experiments used in nuclear structure investigations and for the Rosenbluth technique.

1.2 Why radiative corrections?

Electron scattering experiments are subject to radiative corrections, going beyond the leading-order Born amplitude (see Fig. 1.3). Vertex correction, vacuum polarization, self-energy diagrams, and the two-photon exchange (TPE) are referred to as internal radiative corrections. The four bremsstrahlung diagrams constitute the external radiative corrections and are the main focus of this thesis. Introducing a small parameter E_0 associated with the photon energy resolution of the detectors, one can show that the cross section can be split up into a non-radiative part including vertex corrections, vacuum polarization, self-energy contributions, TPE, and the emission of soft bremsstrahlung photons with energies below E_0; and into a radiative part, accounting for the emission of bremsstrahlung photons with energies above the low-energy cut-off E_0. The individual contributions from the internal and external radiative correction

[§]In a collaboration with M. Jones from TJNAF, we inserted the full angular bremsstrahlung code from Sec. 3.1 into SIMC-SEMI, a data analysis code for $p(e,e'p)\pi^0$ experiments at TJNAF. The results are still pending.

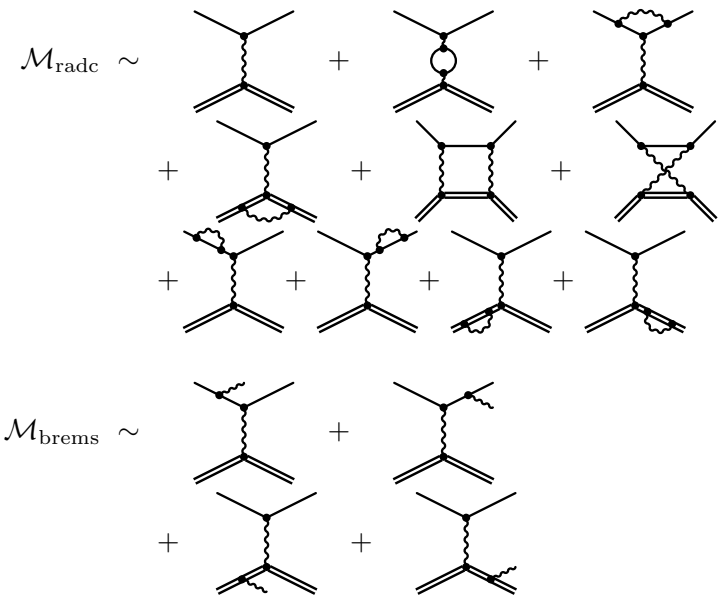

Figure 1.3: Feynman diagrams beyond the leading order. The leading Feynman diagram together with vertex corrections, vacuum polarization and bremsstrahlung are called the Born approximation. The two TPE diagrams go beyond this approximation and have received a lot of attention recently in H$(e, e'p)$ experiments studying the proton electric form factor [22, 29, 30]. But they are non-relevant for $A(e, e'p)$ experiments where $A > 1$. The last four diagrams are the internal bremsstrahlung contributions.

diagrams are infrared divergent. It has first been shown by Schwinger [25] that these divergences cancel when introducing a low-energy cut-off in the limit where this cut-off vanishes. Vacuum polarization, self-energy diagrams, and vertex corrections can be calculated exactly in pure QED and to a good accuracy including hadronic loops. The two TPE diagrams (also called box diagrams, see Fig. 1.3) which compensate divergences from electron-proton bremsstrahlung interference contributions can only be calculated approximately. The divergent TPE parts have been extracted by Mo and Tsai by calculating the two diagrams considering only the nucleon intermediate state in the limit where one of the two exchanged photons carries zero momentum. They applied this approximation both in the numerator and in the denominator of the fermion propagator [26]. Maximon and Tjon improved this calculation by removing this approximation from the denominator of the fermion propagator [27, 28]. The finite contributions to the TPE diagrams are mainly relevant for the Rosenbluth method which is very sensitive to corrections systematically depending on the scattering angle [22, 29, 30]. In order to estimate the TPE correction to the Rosenbluth method Blunden, Melnitchouk, and Tjon employed the full propagator [29, 30]. The finite TPE contributions can be omitted,

however, for $A(e,e'p)$ experiments on nuclei with $A > 1$ where they constitute very minor corrections only, as for most electron scattering experiments [31–34]. In electron scattering off nuclei with $A > 1$ they are known to only be seen in elastic scattering on ^{12}C in the vicinity of the minimum of the form factor.

The emission of bremsstrahlung alters the momenta and energies seen by the detectors and has to be corrected for in data analyses. Mo and Tsai discussed this feature of electron scattering experiments in Refs. [26, 35], considering single-photon bremsstrahlung exactly, aside from the approximation described above in the calculation of the TPE contribution. Multi-photon emission is only included for soft photons with energies smaller than E_0. A review of radiative corrections can be found in Ref. [36].

In order to obtain the desired experimental accuracy one has to take into account higher-order bremsstrahlung processes (multi-photon emission) above the low-energy cut-off [37–39]. In the so called soft-photon approximation (SPA) this is very straight-forward and can be achieved by simply exponentiating the bremsstrahlung contribution to the cross section, because in the SPA the bremsstrahlung cross section factorizes [37, 38, 40]. The factorization is due to the fact that a bremsstrahlung photon of energy ω^0 has no effect on the scattering process in the limit where $\omega^0 \to 0$. Exponentiating soft-photon contributions below the low-energy cut-off E_0 also gives the cross section the correct asymptotic behaviour as $E_0 \to 0$ [25, 36, 37, 41]. The question is, however, up to which upper limit of the bremsstrahlung photon energy domain the SPA is valid. While second-order QED corrections to electron scattering experiments have been calculated exactly, including hadronic loops to a good accuracy [26, 35, 40] and including proton structure [28], multi-photon data analyses are usually performed in the SPA because it allows both for straight-forward inclusion of higher-order bremsstrahlung and for straight-forward Monte Carlo generation of the bremsstrahlung photon angular distribution.

The purpose of this thesis is to improve the multi-photon radiative correction treatment for $(e,e'p)$ experiments at MAMI and TJNAF energies by removing the peaking approximation and the SPA. The latter on is partially removed from data analysis by introducing a novel strategy to deal with multi-photon bremsstrahlung above the low-energy cut-off E_0.

For the sake of completeness we want to add that analyzing experimental data for radiative effects involves two sorts of bremsstrahlung: there is *internal* and *external* bremsstrahlung. The former is the subject of this manuscript. And the latter is bremsstrahlung emitted by the electron or the proton when being deflected by nuclei in the target material other than the one from the hard scattering. The internal bremsstrahlung cross section is independent of the target

thickness, whereas the one of external bremsstrahlung is proportional to it. Its relative importance can thus easily be reduced by considering thin targets [36]. While we will see later that peaking approximation and SPA are bad approximations for internal bremsstrahlung, they are good approximations for external bremsstrahlung, also due to its inclusive nature [40].

1.3 Approximations used in the treatment of radiative corrections

The improved treatment of radiative corrections presented in this thesis includes both the removal of the SPA and the removal of the peaking approximation. These approximations are discussed in detail in the remainder of this section.

1.3.1 Soft-photon approximation

In Sec. 1.2 we mentioned already one important approximation often used in radiative correction calculations — the SPA. Let us write down the QED bremsstrahlung amplitudes both exactly and in the SPA, paving the grounds for the calculation of the bremsstrahlung cross section in the next chapter.

The QED first-order Born amplitude (see first diagram in Fig. 1.3) is given by

$$\mathcal{M}^{(1)}_{\text{Born}} = ie^2 \bar{u}(k')\gamma^\mu u(k)\frac{1}{q^2}\bar{u}(p')\Gamma_\mu u(p)\,. \tag{1.2}$$

where the vertex Γ_μ is defined by

$$\Gamma_\mu \equiv F_1(q^2)\gamma_\mu + \frac{i\kappa F_2(q^2)}{4M}\sigma_{\mu\nu}q^\nu\,. \tag{1.3}$$

This vertex accounts for the structure of the struck proton; m and M are the electron and proton masses, respectively; κ is the proton's anomalous magnetic moment. In the laboratory frame we denote the incident electron's four-momentum as $k = (\epsilon, \mathbf{k})$, the scattered electron has four-momentum $k' = (\epsilon', \mathbf{k}')$. The incoming proton is initially at rest, so it has four-momentum $p = (M, \mathbf{0})$. The outgoing proton has four-momentum $p = (p'^0, \mathbf{p}')$. The momentum transfer between electron and proton is denoted by

$$q \equiv k - k'\,. \tag{1.4}$$

The bremsstrahlung photon's four-momentum will be written as

$$\omega = \omega^0\,(1, 1, \Omega_\gamma)\ . \tag{1.5}$$

The Pauli tensor in expression (1.3) is defined by

$$\sigma_{\mu\nu} \equiv \frac{i}{2}[\gamma_\mu, \gamma_\nu] \,. \tag{1.6}$$

The four QED bremsstrahlung amplitudes (see Fig. 1.3) are given by

$$\mathcal{M}_{\rm ei} = ie^3 \bar{u}(k')\gamma^\mu \left[\frac{i\gamma^\alpha(k-\omega)_\alpha + m}{(k-\omega)^2 - m^2}\right] \gamma^\nu \varepsilon_\nu u(k) \frac{1}{\tilde{q}^2} \bar{u}(p')\Gamma_\mu(\tilde{q}^2)u(p) \,, \tag{1.7}$$

for bremsstrahlung emitted by the incident electron, by

$$\mathcal{M}_{\rm ef} = ie^3 \bar{u}(k')\gamma^\alpha \varepsilon_\alpha \left[\frac{i\gamma^\nu(k'+\omega)_\nu + m}{(k'+\omega)^2 - m^2}\right] \gamma^\mu u(k) \frac{1}{\tilde{q}^2} \bar{u}(p')\Gamma_\mu(\tilde{q}^2)u(p) \,, \tag{1.8}$$

for bremsstrahlung emitted by the scattered electron, by

$$\mathcal{M}_{\rm pi} = -ie^3 \bar{u}(p')\Gamma^\mu(q) \left[\frac{i\gamma^\nu(p-\omega)_\nu + M}{(k-\omega)^2 - M^2}\right] \varepsilon_\alpha \Gamma^\alpha(\omega) u(p) \frac{1}{q^2} \bar{u}(k')\gamma_\mu u(k) \,, \tag{1.9}$$

for bremsstrahlung emitted by the incoming proton, and by

$$\mathcal{M}_{\rm pf} = -ie^3 \bar{u}(p')\Gamma^\alpha(\omega) \varepsilon_\alpha \left[\frac{i\gamma^\nu(p'+\omega)_\nu + M}{(p'+\omega)^2 - M^2}\right] \Gamma^\mu(q^2) u(p) \frac{1}{q^2} \bar{u}(k')\gamma_\mu u(k) \,, \tag{1.10}$$

for bremsstrahlung from the struck proton. The vector $\varepsilon_\nu = \epsilon_\nu(\omega)$ describes the helicity of the bremsstrahlung photon. For bremsstrahlung originating from the electron we use the momentum transfer

$$\tilde{q} \equiv p - p' \,, \tag{1.11}$$

and for bremsstrahlung coming from the proton we use definition (1.4). q and $\tilde{q}$ are also inserted into the respective form factors, entering expressions (1.7) to (1.10) through the vertex functions Γ^μ. We assume that the intermediate proton in the amplitudes (1.9) and (1.10) is propagating like a Dirac particle which should be a good approximation for soft photons [40]. We will refer to the four bremsstrahlung amplitudes above as the 1γ amplitudes.

In the limit where the bremsstrahlung photon energy goes to zero, the four amplitudes (1.7) to (1.10) can be calculated in the SPA. As mentioned in the previous section, the SPA leads to a factorization of the 1γ amplitudes, because in the limit as $\omega^0 \to 0$ the emitted bremsstrahlung photon has no effect on the scattering process — neither on its kinematics nor on the evaluation of the form factor. So, *e.g.*, in the SPA the amplitude (1.7) factorizes into the elastic Born amplitude times the amplitude for emitting a bremsstrahlung photon with

energy ω^0. To see the factorization, considering the amplitude $\mathcal{M}_{\text{ei}}$, we re-write it in terms of the first-order Born amplitude $\mathcal{M}^{(1)}_{\text{Born}}$,

$$i\mathcal{M}_{\text{ei}} = -ie\bar{u}(k')\mathcal{M}^{(1)}_{\text{Born}}(k', k-\omega)\frac{i(\not{k}-\not{\omega}+m)}{(k-\omega)^2-m^2}\gamma^\nu\varepsilon_\nu u(k)\,. \tag{1.12}$$

Assuming, the emitted bremsstrahlung photon is soft, we approximate the Born amplitude (1.2) by

$$\mathcal{M}^{(1)}_{\text{Born}}(k', k-\omega) \sim \mathcal{M}^{(1)}_{\text{Born}}(k', k) \quad (\omega^0 \to 0)\,. \tag{1.13}$$

We also omit the soft bremsstrahlung photon momentum ω in the numerator of the fermion propagator. One can easily show that [42]

$$(\not{k}+m)\gamma^\mu\varepsilon_\mu u(k) = 2p^\mu\varepsilon_\mu u(k)\,. \tag{1.14}$$

Inserting this expression into (1.12) the incident electron bremsstrahlung amplitude $\mathcal{M}_{\text{ei}}$ becomes

$$\mathcal{M}_{\text{ei}} \sim -e\mathcal{M}^{(1)}_{\text{Born}}\left(\frac{k\cdot\varepsilon}{k\cdot\omega}\right) \quad (\omega^0 \to 0)\,, \tag{1.15}$$

in the SPA. Similarly we obtain for the remaining 1γ amplitudes in SPA,

$$\mathcal{M}_{\text{ef}} \sim e\mathcal{M}^{(1)}_{\text{Born}}\left(\frac{k'\cdot\varepsilon}{k'\cdot\omega}\right) \quad (\omega^0 \to 0)\,, \tag{1.16}$$

and

$$\mathcal{M}_{\text{pi}} \sim e\mathcal{M}^{(1)}_{\text{Born}}\left(\frac{p\cdot\varepsilon}{p\cdot\omega}\right) \quad (\omega^0 \to 0)\,, \tag{1.17}$$

and

$$\mathcal{M}_{\text{pf}} \sim -e\mathcal{M}^{(1)}_{\text{Born}}\left(\frac{p'\cdot\varepsilon}{p'\cdot\omega}\right) \quad (\omega^0 \to 0)\,. \tag{1.18}$$

As mentioned earlier, the SPA can easily be removed for single-photon bremsstrahlung. But it simplifies multi-photon emission considerably. In Chap. 3 we will introduce a novel multi-photon bremsstrahlung treatment, going beyond the SPA and partially replacing it.

1.3.2 Peaking approximation

Another important approximation employed in data analyses is the peaking approximation. Most of the bremsstrahlung photons from the electron are emitted either in the direction of the incoming or outgoing electron and one can observe two radiation peaks at the respective angles (see Fig. 1.4). The proton bremsstrahlung is much less peaked. At very high momentum transfers

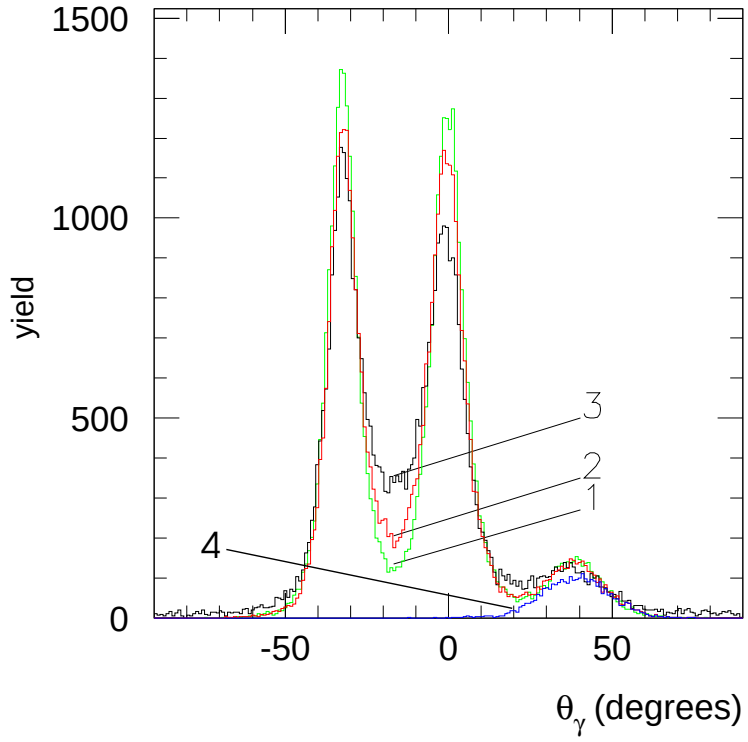

Figure 1.4: Bremsstrahlung angular distribution in the H$(e, e'p)$ reaction at the kinematics given in tab. 1.1. The black histogram (3) shows the measured experimental angular distribution of bremsstrahlung. The experimental photon angle θ_γ is reconstructed from the missing momentum according to eq. (4.1). The green line (1) and the red line (2) correspond to a Monte Carlo simulation based on the PA and take into account finite detector resolution. The red line takes into account emission of bremsstrahlung from e, e', and p', whereas the green line only allows for bremsstrahlung emitted solely from either e, e', or p'. The blue line (4) in the vicinity of the proton direction simulates a deficiency of the apparatus (punch-through effects). Simulations and data do not have to be normalized, all curves represent absolute yields, accounting for luminosities and detector efficiencies *etc.* One can clearly see that the peaking approximation underestimates the bremsstrahlung especially between the two photon peaks in the two electron directions and also between the peaks in incident electron direction and in proton direction.

one can see a bump (rather than a peak) in its direction, too. The peaking approximation, first proposed for (e, e') experiments by L. I. Schiff [43] in 1952, makes use of this observation by assuming that *all* radiation goes either in the direction of the incoming electron, or the scattered electron. With the advent of high-precision coincidence experiments the peaking approximation was extended to $(e, e'p)$ data [40], assuming that the proton bremsstrahlung was peaked as well. This approximation underestimates the non-peaked contributions to the bremsstrahlung photon angular distribution, because it adds all non-peaked

Q^2	$2\,\mathrm{GeV}^2$
ϵ	$3.120\,\mathrm{GeV}$
$\lvert\mathbf{k}'\rvert$	$2.050\,\mathrm{GeV}$
$\lvert\mathbf{p}'\rvert$	$1.700\,\mathrm{GeV}$
θ_e	32.5^o
θ_p	-38.5^o

Table 1.1: The kinematic settings at which the standard radiative corrections and the full angular simulation are compared to the data. We have set $c \equiv 1$.

strength onto the three peaks. Especially between the two radiation peaks of the electron the discrepancy becomes large (see Fig. 1.4), limiting the accuracy of $(e, e'p)$ data analyses [44, 45].

The peaking approximation assumes all bremsstrahlung photons to be aligned with the emitting particle's momentum. So naively we would expect three Dirac delta functions in Fig. 1.4. But limited detector resolution and acceptance, multiple scattering and last but not least multi-photon bremsstrahlung lead to a broadening of the three peaks, giving them finite widths and heights.

Attempts to remove the peaking approximation from single-photon radiative corrections to electron-proton scattering experiments have already been made both for polarized and unpolarized beams [46–48]. But neither have these procedures been made available for analysis codes nor can they handle multi-photon bremsstrahlung. In connection with virtual Compton scattering experiments at MAMI a full angular calculation not using the peaking approximation has been described [49], but it is single-photon only and it is not available for other $(e, e'p)$ experiments.

Also, the peaking approximation has been removed for analyses of parity violating electron scattering experiments recently [50, 51]. But only single-photon bremsstrahlung is considered, the kinematic range of this analysis went only up to $Q^2 < 1.0\,\mathrm{GeV}^2$, and the results are presented such that the impact of the peaking approximation cannot be disentangled from the total radiative corrections. Thus Refs. [50, 51] do not answer the question whether the peaking approximation is a good approximation or not.

2 Standard bremsstrahlung cross section

In this Chapter we will calculate the bremsstrahlung cross section, initially using the SPA. Also, the peaking approximation will be discussed, emphasizing its convenience both for the calculations and for the implementation of radiative corrections in data analyses. Finally we will sketch the full single-photon bremsstrahlung calculation in QED. The SPA bremsstrahlung cross section will later be simulated using Monte Carlo event generators.

2.1 SPA cross section

Let us first calculate the elastic Born cross section. Squaring the Born amplitude (1.2) we obtain

$$|\mathcal{M}_{\mathrm{SPA}}|^2 = \frac{e^4}{q^4} L_{\mathrm{e}}^{\mu\nu} W_{\mu\nu}^{\mathrm{hadron}}, \tag{2.1}$$

where the leptonic tensor is

$$\begin{aligned} L_{\mathrm{e}}^{\mu\nu} &\equiv \frac{1}{2} \sum_{\mathrm{e\,spins}} [\bar{u}(k')\gamma^\mu u(k)][\bar{u}(k')\gamma^\nu u(k)]^\star \\ &= \frac{1}{2}\mathrm{tr}[(\not{k}' + m)\gamma^\mu(\not{k} + m)\gamma^\nu] \\ &= 2[k'^\mu k^\nu + k'^\nu k^\mu - (k'\cdot k - m^2)g^{\mu\nu}]\,. \end{aligned} \tag{2.2}$$

and the hadronic tensor is given by

$$\begin{aligned} W_{\mu\nu}^{\mathrm{hadron}} &\equiv \frac{1}{2} \sum_{\mathrm{p\,spins}} [\bar{u}(p')\Gamma_\mu u(p)][\bar{u}(p')\Gamma_\nu u(p)]^\star \\ &= \frac{1}{2}\mathrm{tr}[(\not{p}' + M)\Gamma_\mu(\not{p} + M)\Gamma_\nu]\,. \end{aligned} \tag{2.3}$$

This trace can be evaluated using the `feyncalc` package [52] for the computer algebra code MATHEMATICA. The vertex Γ^μ is defined by Eq. (1.3).

In order to obtain the electron-proton cross section to order α^2 including bremsstrahlung with total energy less than ΔE_{m},

$$\frac{d\sigma}{d\Omega_{\mathrm{e}}}(\omega^0 < \Delta E_{\mathrm{m}})\,, \tag{2.4}$$

where ω^0 is the bremsstrahlung photon energy, the amplitudes depicted in Fig. 1.3 are considered. The four bremsstrahlung diagrams contributing to $\mathcal{M}_{\mathrm{brems}}$ are divergent in the limit of vanishing bremsstrahlung photon energies. These divergences cancel the ones both from the TPE diagrams* and the vertex corrections [25]. The TPE diagrams are special cases, as already indicated in the introduction. While consideration of their divergent pieces is necessary in order to remove all divergences from the scattering amplitudes, their finite contributions are known to be negligible in $A(e,e'p)$ experiments with $A > 1$. As mentioned before, Mo and Tsai calculated the box diagrams using only the nucleon intermediate state in the limit where one of the two photons exchanged has zero momentum. Improved calculations can be found in [26–30]. According to Ref. [29] a model-dependent calculation of the influence of the TPE yields effects of the order of 1-2% for the kinematic settings considered in the present manuscript. $(e,e'p)$ analysis codes follow the calculation by Mo and Tsai [40, 53] and so do we.

As we initially assume that the SPA is valid we can approximate the four bremsstrahlung diagrams by a product of the Born amplitude times a correction factor, as seen in Eqs. (1.15) to (1.18). In order to obtain the bremsstrahlung cross section from these amplitudes, we need to add and to square them, summing over final states and averaging over initial states. This is particularly straight-forward in the SPA, since only one well-known QED trace occurs, which is the one leading to the first-order Born cross section.

Squaring the SPA bremsstrahlung amplitudes (1.15) to (1.18), we obtain

$$|\mathcal{M}_{\mathrm{SPA}}|^2 = \frac{e^4}{q^4} L_{\mathrm{e}}^{\mu\nu} W_{\mu\nu}^{\mathrm{hadron}} \frac{A(\Omega_\gamma)}{(\omega^0)^2}\,, \tag{2.5}$$

where the leptonic and the hadronic tensors are defined by (2.2) and (2.3), respectively. The expression $A(\Omega_\gamma)$ in Eq. (2.5) is the SPA bremsstrahlung photon angular distribution,

$$A(\Omega_\gamma) \equiv \frac{\alpha(\omega^0)^2}{4\pi^2}\left(-\frac{k'}{\omega\cdot k'} + \frac{p'}{\omega\cdot p'} + \frac{k}{\omega\cdot k} - \frac{p}{\omega\cdot p}\right)^2\,, \tag{2.6}$$

containing the correction terms from Eqs. (1.7) to (1.10). It does not depend on the photon energy ω^0, which vanishes when expanding expression (2.6).

*The divergences from the TPE diagrams cancel with the one from the electron-proton bremsstrahlung interference term which appears after squaring the full scattering amplitude.

The squared matrix element (2.5) is a product of a tensor contraction with the photon angular distribution (2.6). This is a consequence of the factorization of the QED bremsstrahlung amplitudes in the SPA.

The SPA cross section for single-photon bremsstrahlung thus is

$$\frac{d\sigma}{d\Omega_{\rm e} d\Omega_\gamma d\omega^0} = \frac{d\sigma^{(1)}}{d\Omega_{\rm e}} \frac{A(\Omega_\gamma)}{\omega^0}\,, \tag{2.7}$$

where we have employed $d^3\omega = d\Omega_\gamma d\omega^0 (\omega^0)^2$; and $d\sigma^{(1)}/d\Omega_{\rm e}$ is the first-order Born cross section.

Integrating over photon angles and energies the total cross section for emitting a photon with energy smaller than $\Delta E_{\rm m}$, the cross section (2.7) becomes

$$\frac{d\sigma}{d\Omega_{\rm e}}(\omega^0 < \Delta E_{\rm m}) \;=\; \frac{d\sigma^{(1)}}{d\Omega_{\rm e}}[1 - \delta_{\rm soft}(\Delta E_{\rm m}) - \delta_{\rm hard}]\,. \tag{2.8}$$

The integration techniques needed to carry out the integration can be found *e.g.* in Ref. [54], the remaining calculations are explicitly carried out in Ref. [40]. The contributions from the vertex corrections and vacuum polarization are included in

$$\delta_{\rm hard} \equiv 2\alpha \left[-\frac{3}{4\pi} \log\left(\frac{Q^2}{m^2}\right) + \frac{1}{\pi} - \sum_i \delta_i^{\rm vp}(Q^2) \right], \tag{2.9}$$

where the vacuum polarization contribution is

$$\delta_i^{\rm vp}(Q^2) \equiv \frac{1}{3\pi} \left[-\frac{5}{3} + \log\left(\frac{Q^2}{m_i^2}\right) \right], \tag{2.10}$$

in the ultra-relativistic (UR) limit. This expressions does not only contain electron-positron loops but also heavier lepton and light quark-anti-quark loops, with m_i denoting their respective masses. The bremsstrahlung is contained in

$$\begin{aligned}
\delta_{\rm soft}(\Delta E_{\rm m}) \;\equiv\; & \frac{\alpha}{\pi} \left\{ \log\left(\frac{|\mathbf{k}||\mathbf{k}'|}{\Delta E_{\rm m}^2}\right) \left[\log\left(\frac{Q^2}{m^2}\right) - 1 \right] \right. \\
& + \log\left(\frac{p^0 p'^0}{\Delta E_{\rm m}^2}\right) \left[\log\left(\frac{Q^2}{M^2}\right) - 1 \right] + \frac{1}{2} \log^2\left(\frac{p'^0}{M}\right) \\
& + \log\left(\frac{p^0 p'^0}{\Delta E_{\rm m}^2}\right) \log\left(\frac{|\mathbf{k}|}{|\mathbf{k}'|}\right) + \log\left(\frac{|\mathbf{k}||\mathbf{k}'|}{\Delta E_{\rm m}^2}\right) \log\left(\frac{|\mathbf{k}|}{|\mathbf{k}'|}\right) \\
& \left. + \frac{1}{2} \log\left(\frac{|\mathbf{k}||\mathbf{k}'|}{M^2}\right) \log\left(\frac{|\mathbf{k}|}{|\mathbf{k}'|}\right) \right\},
\end{aligned} \tag{2.11}$$

also given in the UR limit. The single-photon cross section (2.8) is still divergent in the limit as $\Delta E_{\rm m}$ vanishes and we also know [37, 38, 40] that one has to take into account higher-order bremsstrahlung terms (multi-photon bremsstrahlung) in order to achieve the desired experimental accuracy. It was shown in Refs. [37, 40] that in fact *all* orders of bremsstrahlung contributions can be considered by just exponentiating the soft photon (bremsstrahlung) term in the cross section (2.8), yielding

$$\frac{d\sigma}{d\Omega_{\rm e}}(\omega_i^0 < \Delta E_{\rm m}) = \frac{d\sigma^{(1)}}{d\Omega_{\rm e}} \exp[-\delta_{\rm soft}(\Delta E_{\rm m})][1-\delta_{\rm hard}]\,. \tag{2.12}$$

The index i indicates that several photons, each with an energy less than the cut-off $\Delta E_{\rm m}$, are emitted. Exponentiating $\delta_{\rm soft}(\Delta E_{\rm m})$ also gives the cross section (2.12) the correct asymptotic behaviour as $E_0 \to 0$ [25, 36, 37, 41].

As the SPA, the exponentiation holds in the limit $E_0 \to 0$ only. $(e,e'p)$ data analysis codes make use of the exponentiation for *all* photon energies [53], because the limited spectrometer acceptances remove events with very high bremsstrahlung photon energies. In order to improve the SPA, we will remove single hard photons from the $\delta_{\rm soft}$ contribution. Such high-energy photons will be treated exactly by taking them out of the exponential and evaluating the cross section exactly instead of using the Born approximation. This will be done in Chap. 3 of this thesis.

Following Ref. [40], we consider the cross section for emitting n photons with an energy larger than a cut-off E_0 together with multi-photon bremsstrahlung up to the photon energy limit E_0,

$$\begin{aligned}\frac{d\sigma(n,E_0)}{d\Omega_{\rm e}d\omega_1^0 d\Omega_1 ... d\omega_n^0 d\Omega_n} &= \frac{d\sigma^{(1)}}{d\Omega_{\rm e}} \exp[-\delta_{\rm soft}(E_0)](1-\delta_{\rm hard})\frac{1}{n!}\frac{A(\Omega_\gamma^{(1)})}{\omega_1^0}...\frac{A(\Omega_\gamma^{(n)})}{\omega_n^0} \\ &\quad \times\theta(\omega_1^0-E_0)...\theta(\omega_n^0-E_0)\,. \end{aligned} \tag{2.13}$$

Summing over all n, and integrating over the photon energies up to an upper boundary $E_{\rm tot} > E_0$ associated with the spectrometer acceptances and experimental cuts, we obtain the total cross section

$$\frac{d\sigma}{d\Omega_{\rm e}}(E_0) = \frac{d\sigma^{(1)}}{d\Omega_{\rm e}} \exp[-\delta_{\rm soft}(E_0)](1-\delta_{\rm hard}) \sum_{n=0}^{\infty}\frac{1}{n!}\prod_{i=1}^{n}\int_{E_0}^{E_{\rm tot}} d\omega_i^0 \frac{\lambda}{\omega_i^0}\,. \tag{2.14}$$

Here,

$$\lambda \equiv \int d\Omega_\gamma A(\Omega_\gamma) \tag{2.15}$$

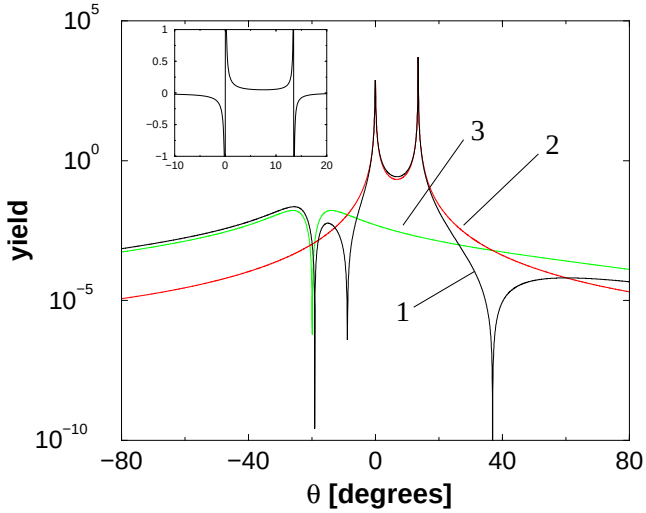

Figure 2.1: Angular distribution of bremsstrahlung using the SPA for the kinematics shown in Tab. 2.1. The black line (1) shows the full angular distribution $A(\Omega_\gamma)$, the red line (2) considers pure electron contributions (ee) only, the green line (3) shows the pure proton contribution (pp). The interference term is partially negative and is shown in the inset graph. It is small compared to the other contributions. The dip for the proton is due to the fact that a particle cannot radiate a photon in forward direction. The same is true of course for electrons but the width of the respective dip is extremely narrow.

Q^2	$15.00\,\mathrm{GeV}^2$
k^0	$21.00\,\mathrm{GeV}$
$\lvert\mathbf{k}'\rvert$	$13.00\,\mathrm{GeV}$
$\lvert\mathbf{p}'\rvert$	$8.882\,\mathrm{GeV}$
θ_e	13.5^o
θ_p	-19.9^o

Table 2.1: The kinematic setting used in Fig. 2.1.

is independent of the photon energy ω^0 and $A(\Omega_\gamma)$ is the angular distribution from Eq. (2.6) which is plotted in Fig. 2.1 for the sample kinematic configuration given in Tab. 2.1. The integrals over the photon energies ω_i^0 in Eq. (2.14) can trivially be solved and the product over i just yields a power of n. We can re-write the cross section, introducing unit terms and, at the same time, a probability density function (PDF) for the bremsstrahlung photon energies. The PDFs enable us to evaluate the total cross section using Monte Carlo generators. They translate the usual flat Monte Carlo random number distributions to physical distributions.

Introducing the PDFs leads to

$$\frac{d\sigma}{d\Omega_e}(E_0) = \frac{d\sigma^{(1)}}{d\Omega_e}\exp[-\delta_{\text{soft}}(E_0)](1-\delta_{\text{hard}})\sum_{n=0}^{\infty}\frac{1}{n!}\left[\lambda\log\left(\frac{E_{\text{tot}}}{E_0}\right)\right]^n \times\left[\prod_{i=1}^{n}\int_{E_0}^{E_{\text{tot}}}d\omega_i^0\,\text{pdf}(\omega_i^0)\right], \tag{2.16}$$

where

$$\text{pdf}(\omega_i^0)\equiv\frac{1}{\omega_i^0\log\left(\frac{E_{\text{tot}}}{E_0}\right)} \tag{2.17}$$

is the probability density function for the ω_i^0. Now we introduce another unit factor, which casts the sum over n into a Poisson distribution, so that we can write the cross section in terms of two PDFs,

$$\frac{d\sigma}{d\Omega_e}(E_0) = \frac{d\sigma^{(1)}}{d\Omega_e}\exp[-\delta_{\text{soft}}(E_0)](1-\delta_{\text{hard}})e^{\lambda\log\left(\frac{E_{\text{tot}}}{E_0}\right)} \times\sum_{n=0}^{\infty}\left\{\frac{1}{n!}\left[\lambda\log\left(\frac{E_{\text{tot}}}{E_0}\right)\right]^n e^{-\lambda\log\left(\frac{E_{\text{tot}}}{E_0}\right)}\right\}\left[\prod_{i=1}^{n}\int_{E_0}^{E_{\text{tot}}}d\omega_i^0\,\text{pdf}(\omega_i^0)\right]. \tag{2.18}$$

The factor in curly brackets is the PDF for n,

$$\text{pdf}(n)\equiv\frac{1}{n!}\left[\lambda\log\left(\frac{E_{\text{tot}}}{E_0}\right)\right]^n e^{-\lambda\log\left(\frac{E_{\text{tot}}}{E_0}\right)}, \tag{2.19}$$

which is just the one of a Poisson distribution in n.[†] Inserting Eqs. (2.17) and (2.19) into (2.18) we can write for the total cross section

$$\frac{d\sigma}{d\Omega_e}(E_0) = \frac{d\sigma^{(1)}}{d\Omega_e}\times\exp[-\delta_{\text{soft}}(E_0)](1-\delta_{\text{hard}}) \times e^{\lambda\log\left(\frac{E_{\text{tot}}}{E_0}\right)}\sum_{n=0}^{\infty}\text{pdf}(n)\prod_{i=1}^{n}\text{pdf}(\omega_i^0). \tag{2.20}$$

The total cross section (2.20) is ultimately found not to depend on E_0 because $\delta_{\text{soft}}(E_0)$ and λ are such that E_0 cancels. In the next section we will show this explicitly for the peaking approximation.

[†]A Poisson distribution in n is defined by $x^n e^{-x}/n!$.

R. Ent *et al.* showed [40] that equation (2.12) holds within a correction of order α^2 for the case that the sum of the energies of all bremsstrahlung photons emitted is smaller than the cut-off E_0,

$$\frac{d\sigma}{d\Omega_\mathrm{e}}\left(\sum_i \omega_i^0 < E_0\right) = \frac{d\sigma}{d\Omega_\mathrm{e}}(\omega_i^0 < E_0)[1+\mathcal{O}(\alpha^2)]\,. \tag{2.21}$$

Therefore, up to an order α^2 correction, cross section (2.20) can be seen as the cross section for emitting several photons, the *sum* of their energies being E_0, along with the emission of n hard photons with energies above the cut-off. $(e,e'p)$ data analysis codes only consider the hard photons. The low-energy cut-off E_0 is chosen to be below the detector acceptances, such that at most bremsstrahlung with total energy E_0 is missed by the radiative correction treatment.

Starting with the cross section (2.13) we obtain the differential cross section for emitting bremsstrahlung photons with total energy E_tot, $d\sigma/d\Omega_\mathrm{e}dE_\mathrm{tot}$ following the same approach as for the total cross section by adding a Dirac delta function, yielding

$$\begin{aligned}\frac{d\sigma}{d\Omega_\mathrm{e}dE_\mathrm{tot}} &= \frac{d\sigma^{(1)}}{d\Omega_\mathrm{e}}\exp[-\delta_\mathrm{soft}(E_0)](1-\delta_\mathrm{hard})e^{\lambda\log\left(\frac{E_\mathrm{tot}}{E_0}\right)}\sum_{n=0}^{\infty}\mathrm{pdf}(n)\\ &\quad\times\prod_{i=1}^{n}\mathrm{pdf}(\omega_i^0)\delta(\omega_1^0+...+\omega_n^0-E_\mathrm{tot})\,.\end{aligned} \tag{2.22}$$

In the Monte Carlo simulation, events are generated according to the three PDFs (2.6), (2.17), and (2.19). And the delta function from Eq. (2.22) can be realized by simulating the total cross section $d\sigma/d\Omega_\mathrm{e}$ and binning the result in the vicinity of

$$\sum_i \omega_i^0 \approx \omega^0\,. \tag{2.23}$$

All observables can, of course, be obtained following the procedure sketched above for the missing energy. The single-photon angular distribution, *e.g.* is obtained by adding a Dirac delta function of the photon angles to the cross section (2.20),

$$\int d\Omega'_\gamma \frac{d\sigma}{d\Omega_\mathrm{e}}\delta(\Omega_\gamma-\Omega'_\gamma)\,. \tag{2.24}$$

The result is then again binned, as in the case of the missing energy shown above.

While the SPA simplifies multi-photon bremsstrahlung calculations considerably by letting the cross section factorize, most $(e, e'p)$ data analysis procedures further extend the SPA by adjusting the kinematic settings of the $(e, e'p)$ reaction and by evaluating the form factors using an adjusted value of q^2 [40, 53, 55], following a suggestion by Borie and Drechsel [56, 57]. We will call this extended version of the SPA the *modified* SPA. It accounts for the bremsstrahlung photons' effect on the scattering process approximately, which is ignored by the pure SPA. It is usually applied when the bremsstrahlung photons cannot be considered being 'soft' any more. As we will see in Chap. 4 the modified SPA can sometimes lead to considerable fractions of unphysical events.

There are several possibilities of modifying the SPA. One way of extending it for single-photon bremsstrahlung is to change from elastic kinematics to 1γ-kinematics. Given the photon four-momentum ω and the beam energy ϵ and fixing *e.g.* the electron scattering angles θ_e and ϕ_e, one can calculate the remaining kinematic quantities of the 1γ process. The SPA cross section is then calculated using the new 1γ kinematic variables and inserting a modified value of q^2 into the form factors.

Modified versions of the SPA also exist for multi-photon bremsstrahlung. For multi-photon emission, one can add up the n bremsstrahlung photons, yielding one (massive) total bremsstrahlung photon ω_{tot}. Subsequently one proceeds as for the 1γ kinematics, but with the photon ω_{tot} in the final state.

The explicit SPA calculation of the bremsstrahlung matrix element (and also the contributions from vertex corrections and from vacuum polarization) can be found in the Appendix of this thesis for the somewhat simpler case of an electron scattered off a Coulomb field.

2.2 Peaking approximation

In the peaking approximation event generation of the photon angles simplifies considerably. Still we need to ensure the cross section (2.20) to be independent of E_0. This has consequences for the decomposition of λ into e, e', and p' parts. As we will see in this section, we have to add additional contributions to the e and the e' part. Following Ref. [40], in this section we will restate the whole procedure which makes the cross section independent of E_0.

Writing the bremsstrahlung contribution to the cross section, $\delta_{\text{soft}}(E_0)$, in the form

$$\delta_{\text{soft}}(E_0) \;=\; \lambda' \log\left(\frac{1}{E_0}\right) + \text{const} \tag{2.25}$$

where λ' is given by

$$\lambda' \equiv \frac{2\alpha}{\pi}\left\{\left[\log\left(\frac{Q^2}{m^2}\right)-1\right]+\left[\log\left(\frac{Q^2}{M^2}\right)-1\right]+2\log\left(\frac{|\mathbf{k}}{|\mathbf{k}'|}\right)\right\}, \quad (2.26)$$

the exponential $\exp[-\delta_{\rm soft}(E_0)]$ becomes

$$\exp[-\delta_{\rm soft}(E_0)] = \exp\left[-\lambda'\log\left(\frac{1}{E_0}\right)\right]\exp(\text{const})\,. \quad (2.27)$$

If λ and λ' are the same, the E_0-dependence in the cross section (2.22) drops out when inserting (2.27). The integration in Eq. (2.15) can easily be performed [40] in order to get λ, yielding terms which can be interpreted as electron-electron (ee) terms, a proton-proton (pp) term (see Fig. 2.1) which is small, an interference (ep) term (see inset graph in Fig. 2.1) which is also small and partially negative, and other terms which are due to unpeaked radiation. These terms are to be called 'missing terms' since they are absent in the peaking approximation. Only taking into account the ee terms one gets [40]

$$\begin{aligned}\lambda &= \frac{\alpha}{\pi}\left[\log\left(\frac{\epsilon+|\mathbf{k}|}{\epsilon-|\mathbf{k}|}\right)+\log\left(\frac{\epsilon'+|\mathbf{k}'|}{\epsilon'-|\mathbf{k}'|}\right)-2\right]\\ &\sim \frac{\alpha}{\pi}\left[\log\left(\frac{4|\mathbf{k}|}{m^2}\right)+\log\left(\frac{4|\mathbf{k}'|}{m^2}\right)-2\right], \end{aligned} \quad (2.28)$$

in the UR limit. In order to find the additional contributions to λ due to non-peaked strength, which are needed to remove E_0 from the cross section (2.22), consider $\delta_{\rm soft}$ from Eq. (2.11) for two different energies,

$$\delta_{\rm soft}(E_1) - \delta_{\rm soft}(E_2) = \frac{2\alpha}{\pi}\log\left(\frac{E_2}{E_1}\right)\left\{\left[\log\left(\frac{Q^2}{m^2}\right)-1\right]+2\log\left(\frac{|\mathbf{k}|}{|\mathbf{k}'|}\right)\right\}. \quad (2.29)$$

Adding these terms to λ and splitting them up in an *ad hoc* manner, λ and λ' can indeed be shown to be equal, because

$$\lambda = \frac{\alpha}{\pi}\left[2\log\left(\frac{4|\mathbf{k}||\mathbf{k}'|}{m^2}\right)-2+2\log\left(\frac{1-\cos\theta_{\rm e}}{2}\right)+4\log\left(\frac{|\mathbf{k}|}{|\mathbf{k}'|}\right)\right]. \quad (2.30)$$

On the other hand λ' as defined in (2.26) can be written as

$$\lambda' = \frac{2\alpha}{\pi}\left[\log\left(\frac{4|\mathbf{k}||\mathbf{k}'|}{m^2}\right)+\log\left(\frac{1-\cos\theta_{\rm e}}{2}\right)+2\log\left(\frac{|\mathbf{k}|}{|\mathbf{k}'|}\right)-1\right], \quad (2.31)$$

where we have omitted the pp contribution. We see that λ and λ' are the same and the unwanted E_0 dependence disappears from the cross section (2.20).

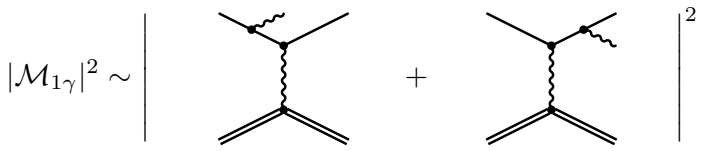

Figure 2.2: The 1γ matrix element squared.

2.3 Exact 1γ cross section

In this section we will sketch the exact QED calculation of the bremsstrahlung matrix element (see Fig. 2.2). We will restrict ourselves to electron radiation which is the dominant contribution to the missing energy. Bremsstrahlung from the proton is a minor correction to the radiative corrections and can be treated with recourse to the SPA, as we will show in Sec. 4.3.

The relevant QED amplitudes were given in the introduction in Eqs. (1.7) and (1.8). Squaring them, summing over final spins and averaging over initial spins, we obtain

$$|\mathcal{M}_{1\gamma}|^2 = \frac{e^6}{q^4} L_{1\gamma}^{\mu\nu} W_{\mu\nu}^{\text{hadron}}\,, \tag{2.32}$$

where the lepton tensor $L_{1\gamma\text{e}}^{\mu\nu}$ includes bremsstrahlung,

$$\begin{aligned} L_{1\gamma}^{\mu\nu} &= \frac{1}{4}\frac{\text{tr}[(\not{k}+m)\gamma^\alpha(\not{k}-\not{\phi}+m)\gamma^\mu(\not{k}'+m)\gamma^\nu(\not{k}-\not{\phi}+m)\gamma_\alpha]}{(k\cdot w)^2} \\ &\quad + \frac{1}{4}\frac{\text{tr}[(\not{k}+m)\gamma^\mu(\not{k}'+\not{\phi}+m)\gamma^\alpha(\not{k}'+m)\gamma_\alpha(\not{k}+\not{\phi}+m)\gamma^\nu]}{(k'\cdot w)^2} \\ &\quad + \frac{1}{2}\frac{\text{tr}[(\not{k}+m)\gamma^\mu(\not{k}'+\not{\phi}+m)\gamma^\alpha(\not{k}'+m)\gamma^\nu(\not{k}-\not{\phi}+m)\gamma_\alpha]}{(k\cdot w)(k'\cdot w)} \end{aligned} \tag{2.33}$$

and the hadron tensor $W_{\mu\nu}^{\text{hadron}}$ is the same as in Eq. (2.3). The traces can be evaluated using the `feyncalc` package [52]. This package can also contract the lepton and the hadron tensors in Eq. (2.32).

The 1γ cross section can now be obtained from the squared matrix element by adding phase space and deviding by the current I,

$$\frac{d\sigma}{d^3k d^3\omega} = (2\pi)^4\delta^{(4)}(k'+p'+\omega-k-p)|\mathcal{M}_{1\gamma}|^2\frac{1}{4I}\frac{d^3k'}{(2\pi)^3 2\epsilon}\frac{d^3p'}{(2\pi)^3 2p'^0}\frac{d^3\omega}{(2\pi)^3 2\omega^0}\,, \tag{2.34}$$

where

$$I \equiv \sqrt{(k\cdot p)^2 - m^2M^2}\,. \tag{2.35}$$

The final result for the exact 1γ cross section can, *e.g.*, be expressed in terms of a set of five independent scalar products. We chose $(k \cdot p)$, $(k' \cdot p)$, $(k \cdot w)$, $(k' \cdot w)$, and (q^2). The full expression is too long to write it out explicitly. We will need it in Chap. 3 in order to partially remove the SPA from $(e, e'p)$ data analysis.

3 Improved radiative corrections

In this chapter we will improve the $(e, e'p)$ radiative correction treatment by first removing the peaking approximation, replacing it with a full angular Monte Carlo simulation. Subsequently we will partially remove the SPA from the standard radiative correction treatment. For multi-photon bremsstrahlung above the low-energy cut-off the SPA cannot be fully removed since an exact QED calculation up to arbitrary order α is not feasible. But in Sec. 3.2 we will introduce a combined method which treats one hard photon from the given multi-photon distribution exactly; and which only takes recourse to the SPA for softer photons.

3.1 Beyond the peaking approximation

Given the full angular SPA differential cross section (2.22) we can now start with the Monte Carlo event generation. As discussed in Sec. 2.2 the bremsstrahlung photon multiplicity n follows a Poisson distribution, the individual photon energies ω_i^0 are distributed according to (2.17), and the photon angular distribution is given by (2.6).

As a first step towards a full angular bremsstrahlung treatment beyond the peaking approximation we tested a photon energy event generator. It generates photon energies on a given energy interval $E_0 < \omega_i^0 < E_{\text{tot}}$ and the photon multiplicities follow the Poisson distribution. The result is shown in Fig. 3.1. The cross section $d\sigma/d\Omega_e d\omega^0$ obtained using the Monte Carlo generator coincides with the analytical calculation from Ref. [40].

The event generation of the photon angles is more elaborate. Standard $(e, e'p)$ data analysis techniques as implemented in codes like SIMC or MCEEP [53, 55] demand that the bremsstrahlung photon's origin is known in order to unfold the data from radiative effects using the modified SPA. Expanding the photon

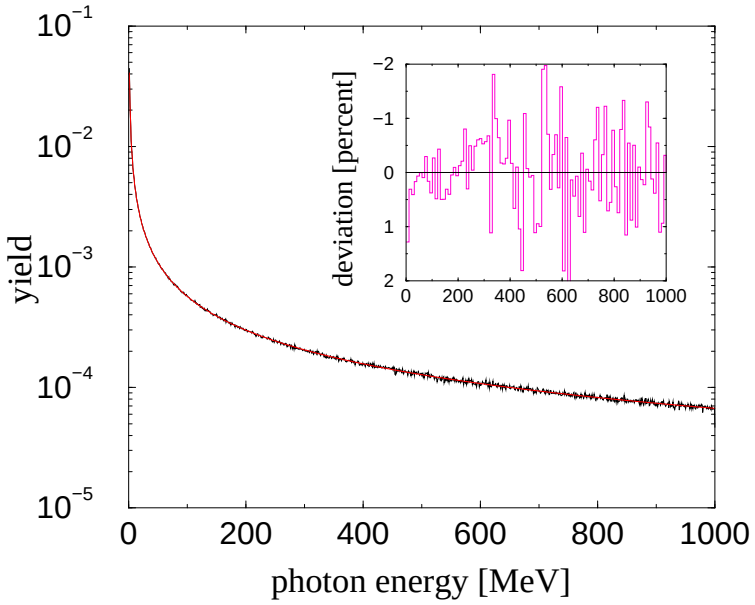

Figure 3.1: Test of the photon energy distribution as generated by our Monte Carlo generator (10^7 events). The black line represents the Monte Carlo events, the red line corresponds to the exact calculation from Ref. [40]. The inset graph (magenta) shows the statistical deviation between the two curves in percent.

angular distribution (2.6),

$$\begin{aligned} A(\Omega_\gamma) \;=\; & -\frac{\alpha\omega^{0^2}}{4\pi^2}\left[\frac{m^2}{(\omega\cdot k')^2}-\frac{2k\cdot k'}{(\omega\cdot k)(\omega\cdot k')}+\frac{m^2}{(\omega\cdot k)^2}\right. \\ & -\frac{2k'\cdot p'}{(\omega\cdot k')(\omega\cdot p')}+\frac{2M\epsilon'}{(\omega\cdot k')(\omega\cdot p)}+\frac{2k\cdot p'}{(\omega\cdot k)(\omega\cdot p')}-\frac{2M\epsilon}{(\omega\cdot k)(\omega\cdot p)} \\ & \left.+\frac{M^2}{(\omega\cdot p')^2}-\frac{2Mp'^0}{(\omega\cdot p')(\omega\cdot p)}+\frac{M^2}{(\omega\cdot p)^2}\right], \end{aligned} \tag{3.1}$$

we assigned to each term radiation coming from (i) the incident electron e, (ii) the scattered electron e', (iii) the incoming proton p, and (iv) the struck proton p'. Some of the terms are sharply peaked, others are responsible for a broad background. The last term in Eq. (3.1), the contribution due to the incoming proton, is a uniform background, as the proton in the target is at rest, compared to the UR velocities of the other particles.

Fig. 2.1 shows the three contributions, e, e', and p', to the angular distribution (2.6), and the full curve also contains the p background. As we can see, there is a dip in the direction of the proton rather than a peak. In fact, the same is true for the two peaks in the electron directions. These three dips are the three peaked terms in expression (3.1) with overall minus signs. Their widths are proportional to their respective masses squared, so we can only

see one of them, the one in the proton direction. The two electron radiation peaks also bear this feature, though it is much less pronounced. These dips are inherent to the amplitudes. It is not possible to emit bremsstrahlung photons in the forward direction, just as a dipole cannot emit radiation along the axis of motion of the oscillating charges. After the observation, that the peaking approximation does not describe the photon angular distribution correctly between the incident and the scattered electron directions (see Fig. 1.4), this is another feature which cannot be reproduced by the peaking approximation.

In order to generate bremsstrahlung photon angles according to the distribution (2.6), or (3.1), respectively, we need a set of positive definite, invertible envelope functions $\hat{A}_i(\Omega_\gamma)$, their sum limiting $A(\Omega_\gamma)$ from above,

$$\hat{A}(\Omega_\gamma) \equiv \sum_i \hat{A}_i(\Omega_\gamma) \geq A(\Omega_\gamma)\,, \tag{3.2}$$

for all photon angles Ω_γ. The fact that we are using envelope functions instead of the angular distribution itself (which is not analytically invertible) forces us to either assign weights to each pair of angles Ω_γ or to use a rejection algorithm. We did the latter one, so when

$$\mu\hat{A}(\Omega_\gamma) \leq A(\Omega_\gamma)\,, \tag{3.3}$$

for some random number μ from the interval [0,1] then the photon angles $x \equiv \cos\theta$ and ϕ are accepted. Otherwise the event is rejected.

The most efficient choice for the envelope curve is

$$\begin{aligned}
\hat{A}_1(\Omega_\gamma) &\equiv \frac{\alpha}{2\pi^2}\frac{\epsilon + |\mathbf{k}|}{\epsilon - |\mathbf{k}|\cos\theta}\,,\\
\hat{A}_2(\Omega_\gamma) &\equiv \frac{\alpha}{\pi^2}\frac{\epsilon' + |\mathbf{k}'|}{\epsilon' - |\mathbf{k}'|\cos\theta}\\
\hat{A}_3(\Omega_\gamma) &\equiv \frac{d\alpha}{2\pi^2}\Theta(\theta)\Theta(\theta_\mathrm{e} - \theta)\,,\\
\hat{A}_4(\Omega_\gamma) &\equiv \frac{\alpha}{2\pi^2}\frac{p'^0 + |\mathbf{p}'|}{p'^0 - |\mathbf{p}'|\cos\theta}\,,
\end{aligned} \tag{3.4}$$

where d is a constant compensating for the underestimation of the bremsstrahlung between the two electron peaks. Please note that each term in Eqs. (3.2) is given in the co-ordinates* which make it easiest to calculate the scalar products in the denominators. $\hat{A}_1(\Omega_\gamma)$ and $\hat{A}_3(\Omega_\gamma)$ are given in the frame where $\mathbf{k}$ points along the z axis, $\hat{A}_2(\Omega_\gamma)$ is given in the frame where $\mathbf{k}'$ points

*We use the SIMC co-ordinate system described in Ref. [59].

along the z axis, and $\hat{A}_4(\Omega_\gamma)$ is given in the frame where $\mathbf{p}'$ points along the z axis.

In order to generate random numbers according to probability densities $\hat{A}_i/p_i$ we choose the standard way to invert the distribution functions which are given by

$$P_i(x) \equiv \frac{1}{p_i}\int_{-1}^{x} dx' \hat{A}_i(x')\,, \tag{3.5}$$

where $x' \equiv \cos\theta$ and

$$p_i \equiv \int_{-1}^{+1} dx \hat{A}_i(x)\,, \tag{3.6}$$

is the normalization constant. We obtain

$$\begin{aligned}
P_1(x) &= \frac{\log\left(\frac{\epsilon+|\mathbf{k}|}{\epsilon-|\mathbf{k}|x}\right)}{\log\left(\frac{\epsilon+|\mathbf{k}|}{\epsilon-|\mathbf{k}|}\right)} = y\,,\\
P_2(x) &= \frac{\log\left(\frac{\epsilon'+|\mathbf{k}'|}{\epsilon'-|\mathbf{k}'|x}\right)}{\log\left(\frac{\epsilon'+|\mathbf{k}'|}{\epsilon'-|\mathbf{k}'|}\right)} = y\,,\\
P_3(x) &= \frac{d\alpha}{2\pi^2}\theta_{\mathrm{e}}\\
P_4(x) &= \frac{\log\left(\frac{p'^0+|\mathbf{p}'|}{p'^0-|\mathbf{p}'|x}\right)}{\log\left(\frac{p'^0+|\mathbf{p}'|}{p'^0-|\mathbf{p}'|}\right)} = y\,,
\end{aligned} \tag{3.7}$$

where y is a flat random number distribution on the interval $[0,1]$. To obtain random numbers distributed according to the $\hat{A}_i/p_i$ we invert the distribution functions, yielding

$$\begin{aligned}
P_1^{-1}(y) &= \frac{\epsilon}{|\mathbf{k}|} - \frac{\epsilon+|\mathbf{k}|}{|\mathbf{k}|}\left(\frac{\epsilon-|\mathbf{k}|}{\epsilon+|\mathbf{k}|}\right)^y = x\,,\\
P_2^{-1}(y) &= \frac{\epsilon'}{|\mathbf{k}'|} - \frac{\epsilon'+|\mathbf{k}'|}{|\mathbf{k}'|}\left(\frac{\epsilon'-|\mathbf{k}'|}{\epsilon'+|\mathbf{k}'|}\right)^y = x\,,\\
P_4^{-1}(y) &= \frac{p'^0}{|\mathbf{p}'|} - \frac{p'^0+|\mathbf{p}'|}{|\mathbf{p}'|}\left(\frac{p'^0-|\mathbf{p}'|}{p'^0+|\mathbf{p}'|}\right)^y = x\,,
\end{aligned} \tag{3.8}$$

where for $P_2^{-1}(y)$ and $P_4^{-1}(y)$ the value of $\theta = \arccos x$ still has to be transformed back into the co-ordinate system where $\mathbf{k}$ points along the z-axis. The inverse of $P_3(x)$ is not needed for it is just a flat off set which accounts for the underestimation of the interpeak strength by terms 1, 2, and 4.

The individual functions (3.4) are chosen by the Monte Carlo event generator according to the integrals (3.6), normalized to their sum,

$$\frac{p_i}{\sum_i p_i} \,. \tag{3.9}$$

In case $\hat{A}_1(\Omega_\gamma)$ is chosen, the bremsstrahlung photon is assumed to originate from the incident electron; if $\hat{A}_2(\Omega_\gamma)$ is chosen, the bremsstrahlung photon is assigned to the scattered electron; and if $\hat{A}_4(\Omega_\gamma)$ is chosen, the photon is assumed to have been emitted by the struck proton.

The function $\hat{A}_3(\Omega_\gamma)$ is an angle-independent distribution at first but shaped by the rejection algorithm into a contribution which is given by *ee* interference. There are several 'coin toss' methods to choose whether an event created from the interference term is assigned to the incoming or the outgoing electron or to both. This assignment is necessary for the modified SPA. We employed three different ways of dealing with the interference term, leading to slightly different results. Together with the Monte Carlo photon energy generation (2.17) and with the photon multiplicity generation (2.19) each of these three ways of dealing with the interference term constitutes a Monte Carlo event generation method for the interference term.

1. The interference term (being essentially a function of the photon angle θ) is split into two parts, the 'left part' consisting of events with angles closer to θ_e and the 'right' part with angles closer to zero. Events closer to the incoming electron direction ('right') were counted for the incoming electron whereas events closer to the outgoing electron ('left') direction were counted for the latter one.

2. In addition to method (1) the energy loss between incident and scattered electron is randomly split.

3. The emitted photon is randomly assigned to either the incoming or the outgoing electron.

For the final comparison between the standard analysis code bremsstrahlung treatment (peaking approximation) and our full angular Monte Carlo simulation we used the third method as it fitted the reconstructed photon distribution most accurately, as we will see in the next chapter.

A full angular bremsstrahlung event generator as described in this section has never been inserted into $(e, e'p)$ data analysis codes.† In order to check our results

†Only for virtual Compton scattering experiments, which measure a different final state but contain the Feynman diagrams from Fig. 1.3 as sub-diagrams, a first-order bremsstrahlung full angular treatment has been described [49]. The respective full angular Monte Carlo generator is not available for $(e, e'p)$ data analyses.

against experimental data and to have a measure for the computational expense it entails, we inserted our Monte Carlo routine into SIMC, an analysis code for $(e, e'p)$ experiments at TJNAF's hall C [53]. It was written by J. Arrington and its radiative correction treatment is due to N. Makins [40]. The results of this test are shown in Chap. 4.

3.2 Beyond the soft-photon approximation

An exact multi-photon QED treatment is not feasible for data analysis since the exact multi-photon amplitudes cannot be included into data analysis codes to arbitrarily high orders. Therefore we introduce a novel *combined approach*: we generate multi-photon bremsstrahlung according to the SPA distribution. We choose one hard photon from the given $n\gamma$ event which we treat exactly by calculating the exact QED 1γ-matrix element (see Fig. 2.2). And we treat the remaining photons as soft photons (with energies still larger than the low-energy cut-off E_0), using the SPA.

There are several possibilities for choosing the hard photon. We employed four methods:

1. Choose the photon with the largest energy ω^0. This method is motivated by the question of the validity of the SPA.

2. Calculate the modified momentum transfer squared, $q^2_{1\gamma}$, for each individual photon of the $n\gamma$ event in 1γ-kinematics and choose the photon yielding a value of $q^2_{1\gamma}$ which is farthest from the elastic value, q^2_{el}. The form factors are then evaluated using $q^2_{1\gamma}$.

3. Add up all n photons, leading to a total photon ω_{tot}. Calculate the new kinematics inserting ω_{tot} into the 1γ kinematics and calculate q^2_{tot}. Choose the photon which leads to a value of $q^2_{1\gamma}$ which is closest to q^2_{tot}. This method and method 2 focus on the fact that the bremsstrahlung emission alters the value of q^2, the effect being two-fold: the form factors are evaluated at the modified momentum transfer; and the leptonic current is changed, which changes the ratio of $F_1(q^2)$ and $F_2(q^2)$ in the cross section [56, 57].

4. Choose the 'hard' photon randomly.

As in the case of the full angular Monte Carlo code described in Sec. 3.1 our Monte Carlo routine generates multiple photons according to the probability density functions in cross section (2.18). Again, the bremsstrahlung photon energies ω^0_i are distributed according to Eq. (2.17) and the photon multiplicities n follow a Poisson distribution. The bremsstrahlung photon angles are generated according to the elastic angular distribution $A(\Omega^i_\gamma)$ from Eq. (2.6). The superscript i

indicates that each individual photon from a multi-photon event follows the angular distribution (2.6). In order to simplify the expressions, let us absorb the photon energy dependence into the angular distribution $A(\Omega_\gamma^i)$, thus obtaining a combined distribution

$$A(\omega_i) \equiv \frac{A(\Omega_\gamma^i)}{\omega_i^0} \,. \tag{3.10}$$

Then, in the SPA, the 1γ bremsstrahlung matrix element squared (see Fig. 2.1) for the hard photon becomes

$$|\mathcal{M}_{1\gamma}|^2 \sim |\mathcal{M}_{\text{Born}}^{(1)}|^2 A(\omega) \,. \tag{3.11}$$

In order to evaluate the applicability of the SPA for the kinematic settings considered in this thesis we compared it to the exact calculation in the case of a single bremsstrahlung photon emitted by the electron. The integration over the bremsstrahlung photons was carried out with our full angular Monte Carlo generator, thus rendering symbolic evaluation of ellipsoidal phase space integrals in the laboratory frame unnecessary.

Consider the single-photon SPA bremsstrahlung cross section

$$\begin{aligned} \sigma_{\text{spa}} &\sim \int \frac{d^3\omega}{(2\pi)^3 2\omega^0} \frac{1}{4I} |\mathcal{M}_{\text{el}}|^2 A(\omega) \\ &= \int \frac{\omega^0 d\omega^0 d\Omega_\gamma}{16\pi^3} \frac{1}{4I} |\mathcal{M}_{\text{el}}|^2 A(\omega) \,, \end{aligned} \tag{3.12}$$

where I is the incident current. Our Monte Carlo code generates bremsstrahlung events according to the distribution

$$\frac{d^3\omega}{(2\pi)^3 2\omega^0} A(\omega) = \frac{\omega^0 d\omega^0 d\Omega_\gamma}{16\pi^3} A(\omega) \,. \tag{3.13}$$

Evaluating the integral in Eq. (3.12) using our SPA Monte Carlo generator we thus obtain

$$\begin{aligned} \sigma_{\text{spa}} &\approx \frac{1}{N} \sum_{\text{events}} \frac{1}{4I} |\mathcal{M}_{\text{el}}|^2 A(\omega) \frac{\omega^0}{16\pi^3} \frac{1}{A(\omega) \frac{\omega^0}{16\pi^3}} \\ &= \frac{1}{N} \sum_{\text{events}} \frac{1}{4I} |\mathcal{M}_{\text{el}}|^2 \,, \end{aligned} \tag{3.14}$$

where N is the number of events, and $\mathcal{M}_{\text{el}}$ is the elastic first-order Born matrix element. The full 1γ calculation (not using SPA) yields

$$\sigma_{1\gamma} \sim \int \frac{\omega^0 d\omega^0 d\Omega_\gamma}{16\pi^3} \frac{1}{4I} |\mathcal{M}_{1\gamma}|^2 \,, \tag{3.15}$$

where

$$\mathcal{M}_{1\gamma} \equiv \mathcal{M}_{\rm ei} + \mathcal{M}_{\rm ef}\,. \tag{3.16}$$

The cross section (3.15) becomes

$$\begin{aligned}\sigma_{1\gamma} &\approx \frac{1}{N}\sum_{\rm events}\frac{1}{4I}\frac{|\mathcal{M}_{1\gamma}|^2}{16\pi^3}\frac{1}{\frac{A(\omega)}{16\pi^3}} \\ &= \frac{1}{N}\sum_{\rm events}\frac{1}{4I}\frac{|\mathcal{M}_{1\gamma}|^2}{A(\omega)}\end{aligned} \tag{3.17}$$

in the Monte Carlo formalism.

Considering initially single-photon bremsstrahlung, we assign each bremsstrahlung event weights in order to re-weight the SPA Monte Carlo generator to a new Monte Carlo generator. The 'exact weight' is

$$w_{1\gamma}^{\rm ex} \equiv \frac{|\mathcal{M}_{1\gamma}|^2}{|\mathcal{M}_{\rm Born}^{(1)}|^2 A(\omega)}\,. \tag{3.18}$$

We want to stress here that the first-order Born amplitude as well as the photon angular distribution $A(\omega)$ are evaluated in elastic kinematics. The exact single-photon emission amplitude $\mathcal{M}_{1\gamma}$ is, of course, evaluated in 1γ-kinematics. In contrast to the 'exact weight' (3.18), the 'modified SPA weight' measures the influence of the kinematic adjustments and the adjusted evaluation of the form factors within the modified SPA,

$$w_{1\gamma}^{\rm mod} \equiv \frac{|\mathcal{M}_{\rm Born}^{(1),{\rm mod}}|^2 A_{\rm mod}(\omega)}{|\mathcal{M}_{\rm Born}^{(1)}|^2 A(\omega)}\,. \tag{3.19}$$

The first-order Born amplitude $\mathcal{M}_{\rm el}^{(1),{\rm mod}}$ as well as the photon distribution $A_{\rm mod}(\omega)$ in the *numerator* have been evaluated in modified 1γ kinematics, in order to account for both kinematic effects of bremsstrahlung and to evaluate the form factors at realistic values of q^2.

This approach can be carried over to multi-photon bremsstrahlung in a straightforward way. Assuming that the n bremsstrahlung photons have been rearranged such that the nth photon is the hard photon, we define

$$w_{n\gamma}^{\rm ex} \equiv \frac{|\mathcal{M}_{1\gamma}|^2 A_{1\gamma}(\omega_1)...A_{1\gamma}(\omega_{n-1})}{|\mathcal{M}_{\rm Born}^{(1)}|^2 A(\omega_{\rm hard})A(\omega_1)...A(\omega_{n-1})}\,, \tag{3.20}$$

for the exact $n\gamma$ weight and

$$w_{n\gamma}^{\rm mod} \equiv \frac{|\mathcal{M}_{\rm Born}^{(1),{\rm tot}}|^2 A_{\rm mod}(\omega_{\rm hard})A_{\rm mod}(\omega_1)...A_{\rm mod}(\omega_{n-1})}{|\mathcal{M}_{\rm Born}^{(1)}|^2 A(\omega_{\rm hard})A(\omega_1)...A(\omega_{n-1})} \tag{3.21}$$

for the modified $n\gamma$ weight. The subscript 1γ in the numerator of (3.20) indicates that the respective contributions to the matrix element squared have been computed in 1γ kinematics and the subscript 'mod' in the numerator of (3.21) indicates that the respective quantities have been evaluated in modified kinematics. The first-order Born amplitude and the photon angular distributions appearing in the (identical) *denominators* of Eqs. (3.20) and (3.21) are evaluated in elastic kinematics.

Our Monte Carlo routine calculates *e.g.* the multi-photon missing energy distribution by generating radiative events according to elastic the energy and angular distribution $A(\omega)$. Then it determines the 1γ-kinematics and uses one of the four methods sketched above in this section to choose the hard photon. Each scattering event is assigned two weights (3.20) and (3.21). Finally the photon energies ω_i^0 are binned in the vicinity of

$$\sum_{i=1}^{n} \omega_i^0 \approx \omega^0 \,, \tag{3.22}$$

in order to obtain the missing energy distribution. Similarly, we generate the photon angular distribution.

As a test of the full angular Monte Carlo routine, we inserted our new combined Monte Carlo routine into the SIMC analysis code [53], in order to be able to compare the error associated with the use of the SPA with other sources of errors.

The combined approach described in this section neglects bremsstrahlung coming from the proton. Photon emission by the proton is rare compared to bremsstrahlung from the electron. In order to measure the effect of proton bremsstrahlung we included it, assuming that the SPA is a good approximation for proton bremsstrahlung. The first-order electron bremsstrahlung was still calculated exactly. This was achieved by changing the weight (3.20) into

$$w_{n\gamma}^{\mathrm{ex}} \equiv \frac{[|\mathcal{M}_{1\gamma}|^2 + |\mathcal{M}_{\mathrm{Born}}^{(1),\mathrm{mod}}|^2 A_{\mathrm{rest}}(\omega_{\mathrm{hard}})] A_{\mathrm{mod}}(\omega_1)...A_{\mathrm{mod}}(\omega_{n-1})}{|\mathcal{M}_{\mathrm{Born}}^{(1)}|^2 A(\omega_{\mathrm{hard}}) A(\omega_1)...A(\omega_{n-1})} \,, \tag{3.23}$$

where $A_{\mathrm{rest}}(\omega_{\mathrm{hard}})$ is the angular distribution (2.6) without the electron-electron terms (and divided by ω_{hard}^0; see Eq. (3.10)). In Sec. 4.3 we will present the results.

4 Results

In this chapter we will first present the results obtained by removing the peaking approximation from experimental analysis, followed by the results obtained by employing the combined calculation which partially removes the SPA from $(e, e'p)$ radiative correction procedures.

4.1 Beyond the peaking approximation

To test our approach we chose several $(e, e'p)$ kinematic settings with beam energies of 3.12 GeV and varying values of Q^2 on a hydrogen target. We usually generated 200,000 successful Monte Carlo events per run to compare peaking approximation and full angular Monte Carlo simulation. Figs. 4.1 – 4.7 show results for the kinematics given in Tab. 1.1 and additionally we studied the kinematic settings shown in Tab. 4.1.

The bremsstrahlung photon angles for H$(e, e'p)$ experiments shown in Figs. 4.1 and 4.2 as well as in 4.3 are obtained according to

$$\theta = \arctan\left(\frac{p_{\mathrm{m}_y}}{p_{\mathrm{m}_z}}\right) , \tag{4.1}$$

where p_{m_y} and p_{m_z} are the missing momenta in y and in z direction, respectively. The notion of a direction of the missing momentum due to bremsstrahlung only exists for H$(e, e'p)$ experiments, where, below pion threshold, the missing momentum is solely due to bremsstrahlung. Our co-ordinate system is the SIMC co-ordinate system described in Ref. [59].

As pointed out in the introduction one weak point of the peaking approximation is its underestimation of the strength of non-peaked radiation especially between the radiation peaks in the directions of the incident and the scattered electron [44, 45]. Fig. 4.1 shows that the photon angular distribution broadens when employing our full angular Monte Carlo simulation. The gap between experimentally determined bremsstrahlung distribution and simulations employing the peaking approximation (also see Fig. 1.3) between the two radiation peaks in e

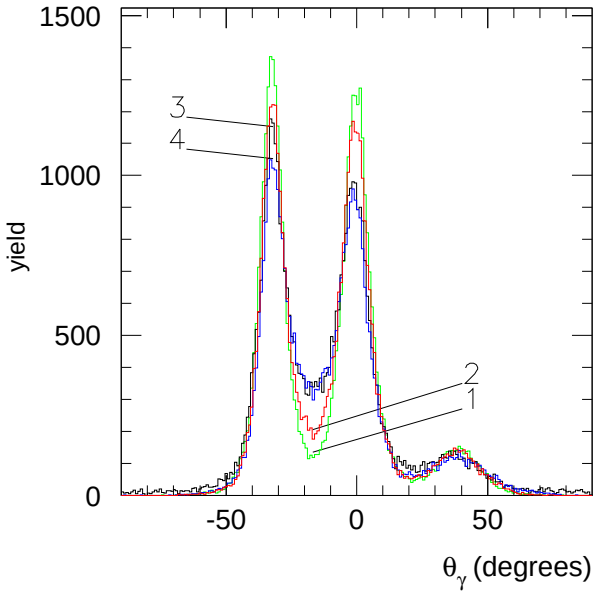

Figure 4.1: Angular distributions of bremsstrahlung photons for the kinematics shown in Tab. 1.1. The green line (1) and the red line (2) represent the two versions of the peaking approximation and the black line (3) shows the measured (reconstructed) experimental angular distribution as already shown in Fig. 1.4. The blue curve (4) represents our full angular Monte Carlo simulation. The peaks in e and in e' direction generated by the full angular Monte Carlo simulation (3) are broader than the ones from the peaking approximation (curves 1 and 2), and agree with the data (3) much better than (1) and (2). In the dip between the radiation peaks due to the incoming electron (at 0^o) and the proton (the small bump at 39^o) the full angular simulation does not entirely overcome the gap between simulation and data. A detailed figure of this region can be found in Fig. 4.2.

and e' direction is filled, the underestimation of the interpeak strength is removed.

When calculated with our method the peak in the proton direction fits the reconstructed bremsstrahlung data well. However, this has to be put into perspective as the proton bremsstrahlung is obscured by a detector related artefact (punch-through effects) such that one cannot make a clear statement on the accuracy here (also see Fig. 4.2, which shows a detail of Fig. 4.1).

For the results presented in this section, the ee interference term discussed in Sec. 3.1 was treated using method (3). This led to the most accurate results as can be seen in Fig. 4.3. The other two methods also improved the angular distribution of the bremsstrahlung photons compared to the standard peaking approximation approach. But they exhibited a slight deviation from the data in the heights of the e and e' peaks. At the kinematic setting used here, shown in Tab. 1.1, the ee interference term accounted for roughly 20% of all events.

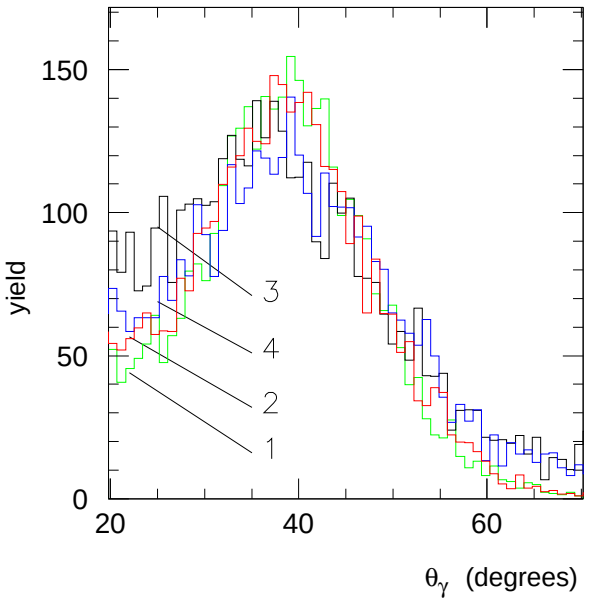

Figure 4.2: Detail of Fig. 4.1 around the proton direction. Colours and numbers are as in Fig. 4.1. In the region between the peak in e direction and the bump in p' direction the full angular simulation (4) does not entirely overcome the gap between simulation and data. But as described in the text the region around the proton direction is obscured by punch-through effects anyway.

Looking at the missing energy distribution (see Fig. 4.4) we see that the overall energy loss is 0.3% smaller than predicted by the peaking approximation. This is well within the systematic uncertainty usually attributed to the radiation correction. The missing momenta (see Fig. 4.5) generated by the standard radiation procedure and by our code are as similar to each other as are the missing energies. The momentum distributions of electron and proton for the kinematics shown in Tab. 1.1 are also not changed significantly by the full angular Monte Carlo calculations, as can be seen in Figs. 4.6 and 4.7.

As a check we also looked at kinematic settings with both larger and smaller values of Q^2, while letting the beam energy unaltered. We compared again the full angular Monte Carlo simulation with the standard radiation code. However, we could not compare all the results to data since the E97-006 experiment did not look at all the kinematic settings from Tab. 4.1 [6]. But two of the five runs could be checked against experimental data. The purpose of simulating kinematic settings with different momentum transfers was to find out whether the deviations between the yield of the standard analysis code and the full angular Monte Carlo simulation depended on Q^2 or on the beam energy ϵ. The discussion of the case where the momentum transfer is left constant while the beam energy is changed

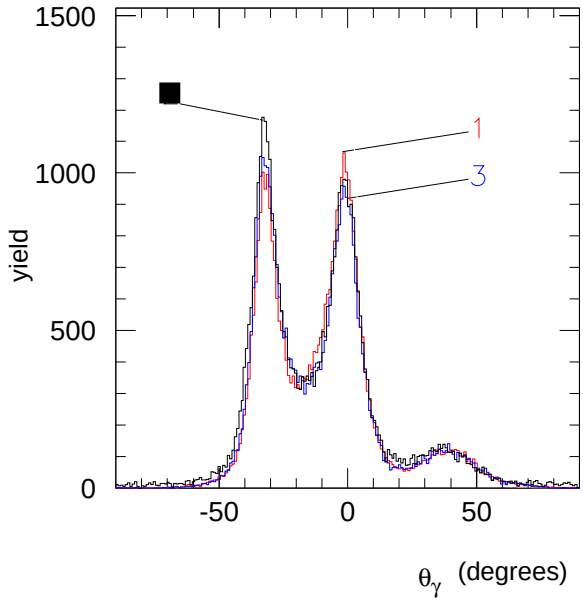

Figure 4.3: Photon angular distribution for the three different treatments of the interference term. Method (1) is represented by the red line and it coincides with method (2) (not shown). The blue line represents method (3), the black line (marked with the black square) shows the data. Method (3) is found to reproduce the data most accurately and is hence used for the full angular simulation (4) in Figs. 4.1 and 4.2.

Q^2/GeV^2	$0.61^\dagger$	1.00	$2.00^\dagger$	3.00	4.00
ϵ/GeV	3.12	3.12	3.12	3.12	3.12
$\lvert\mathbf{p}'\rvert/\mathrm{GeV}$	0.852	1.13	1.70	2.36	2.92
$\lvert\mathbf{k}'\rvert/\mathrm{GeV}$	2.74	2.59	2.05	1.52	0.99
Δ yield	+0.70%	+0.64%	−0.10%	−0.63%	−2.5%

Table 4.1: The deviations in the yield, integrated up to 0.7 GeV energy loss through bremsstrahlung, between the standard analysis code and the full angular Monte Carlo simulation. The kinematic settings marked with a dagger represent actual experimental runs, the others have only been simulated.

will be given in Chap. 5 because it automatically leads to kinematic settings used for Rosenbluth separations. Looking at the total yield in Tab. 4.1 we found differences of up to 3.0%, the yield of the full angular Monte Carlo simulation being smaller than the standard analysis yield when going to higher momentum transfers and larger for small values of Q^2.

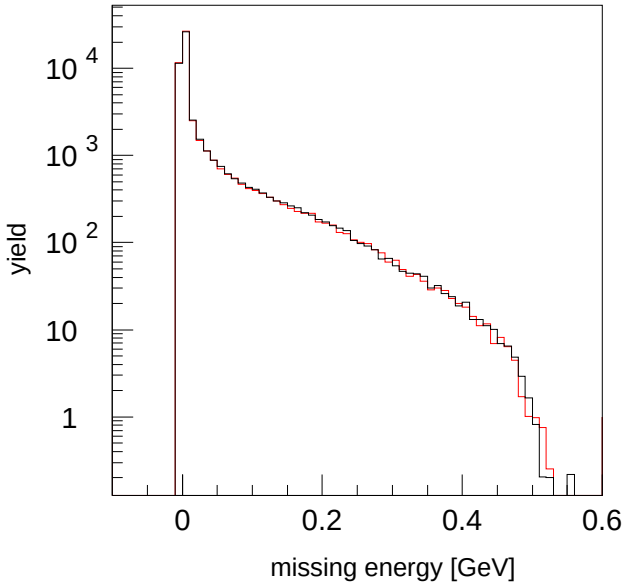

Figure 4.4: Logarithmic plot of photon energy distribution for the kinematics shown in Tab. 1.1. The black line was obtained using the peaking approximation, the red line shows the results obtained with the full angular Monte Carlo simulation. The total radiated energy simulated for the latter case is only about 0.3% smaller than the one from the peaking approximation which is well within the uncertainties attributed to radiative corrections.

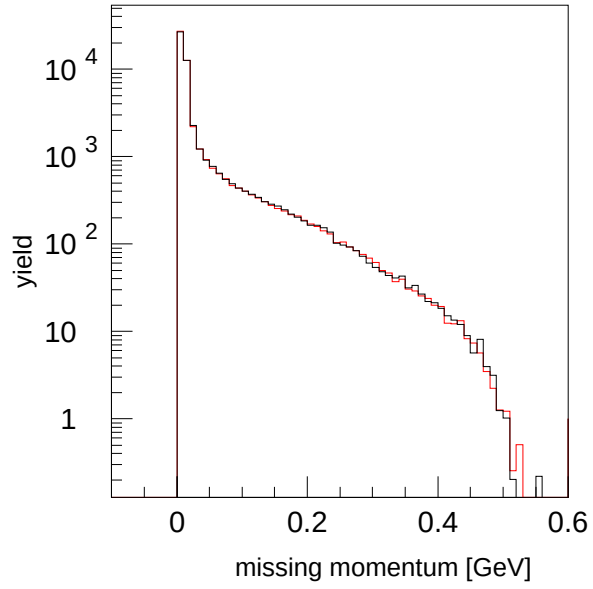

Figure 4.5: Logarithmic plot of reconstructed missing momentum distribution for the kinematics shown in Tab. 1.1. The missing momentum is almost unaltered. The full angular simulation is represented by the red line, the peaking approximation by the black line.

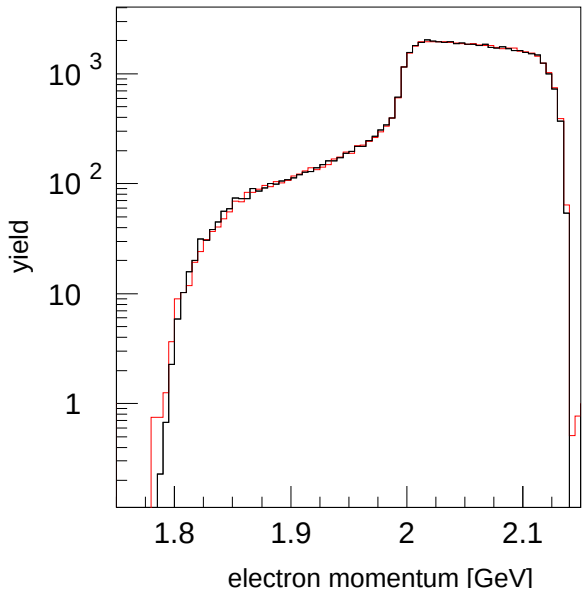

Figure 4.6: Electron momentum distribution for the kinematics shown in Tab. 1.1. The black line was obtained using the peaking approximation, the red line shows the results using the full angular Monte Carlo simulation.

4.2 The need to improve the soft-photon approximation — revisited

The discrepancies described in the previous section and shown in Tab. 4.1 are related to the inappropriate application of the SPA. Our full angular Monte Carlo approach is more sensitive to the problems caused by the modified SPA than the peaking approximation at certain kinematic settings. Including the full angular dependence of bremsstrahlung photons (other than the trivial angular dependence of the peaking approximation) and changing the particle momenta can occasionally lead to energy gains for both electron and proton as long as the particles are assumed to be on-shell at all times, which is of course a simplification. Such un-physical events are rejected by our code, because they are artefacts of the modified SPA which corrects for the energy losses due to soft photons and assumes on-shell vertices. In addition to the factorization of the cross section (see Eq. (2.7)), the modified SPA leads to a modified form factor, since the momentum transfer is altered by the radiation.* At some kinematic settings the un-physical events described above account for a significant fraction of all

*As mentioned in Chap. 2 the modified SPA adjusts particle momenta in order to account for the emission of bremsstrahlung. In the case where the peaking approximation is applied additionally to the SPA this means that $k \to k - \omega_i$, $k' \to k' - \omega_f$, and $p' \to p' - \omega_p$, where ω_i, ω_f, and ω_p are the total bremsstrahlung momenta emitted by e, e', and p'. Their three-momenta are aligned with the respective three-momenta of the emitting particles.

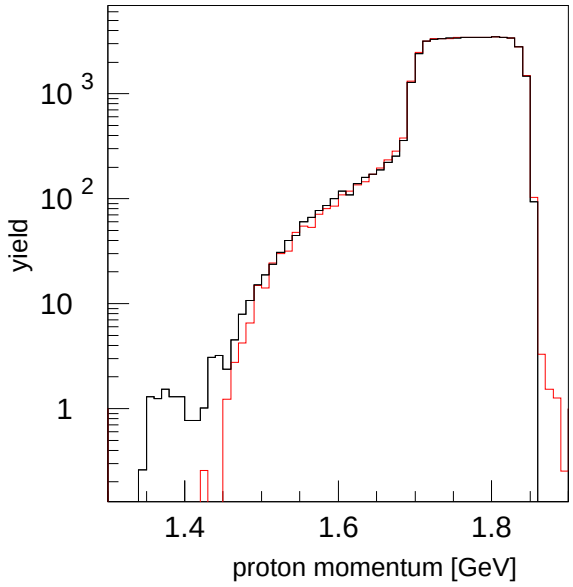

Figure 4.7: Proton momentum distribution for the kinematics shown in Tab. 1.1. Full angular Monte Carlo simulation (red line) and peaking calculation (black line) almost coincide.

events, changing the total yield by up to a few percent, as can be seen in Tab. 4.1.

The peaking approximation does not have that problem since it can fulfill both energy and momentum conservation at the same time when assuming massless on-shell electrons. Energy gains through emission of radiation are not possible. The scattered protons cannot assumed to be massless, of course. But as they account for a small fraction of high energy bremsstrahlung events only, they do not change the total yield much, neither in the case of the peaking approximation nor for the full angular simulation.

The fact that removing the peaking approximation alone from $(e, e'p)$ data analyses sometimes leads to a considerable fraction of unphysical events indicates that the full angular Monte Carlo calculation reveals problems due to the SPA which are kept in the dark when using the peaking approximation. This emphasizes the need for a more structured and more consistent approach to the improvement of radiative corrections. Unphysical events should be prevented by calculating the bremsstrahlung kinematics of bremsstrahlung events exactly, as described in Sec. 3.2.

Emission of bremsstrahlung alters both the kinematics and has an impact on the evaluation of the form factors. $(e, e'p)$ data codes using the peaking approximation and the SPA, like SIMC, account for these effects as follows: they consider

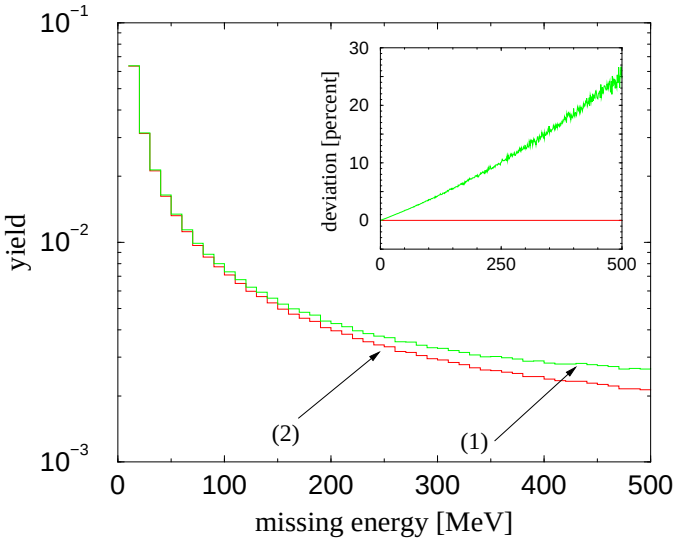

Figure 4.8: Missing energy distribution for multi-photon bremsstrahlung. The green curve (1) was obtained using the modified SPA weight (3.21). The red curve (2) represents the combined approach using weight (3.20). The inset graph shows the deviation between the two curves in percent normalized to the combined result. At $E_m = 100\,\text{MeV}$ the modified SPA calculation overestimates the radiative tail by 3.6%, at $E_m = 500\,\text{MeV}$ the deviation is 25%. The momentum transfer is $Q^2 = 0.6\,\text{GeV}^2$.

bremsstrahlung from the incident electron only, aligned with the momentum $\mathbf{k}$, then generate the modified kinematics and a modified value of q^2 which is inserted into the form factors. Bremsstrahlung from the outgoing particles are only considered kinematically. It does not enter the evaluation of the form factors.

A more structured approach, using the bremsstrahlung kinematics with an appropriate value for q^2 is more preferable. The value of q^2 inserted into the form factors should account for the total bremsstrahlung emission. The approach of Borie and Drechsel [56, 57] would be obsolete if (additionally to the 1γ kinematics) the 1γ cross section was calculated exactly without using the SPA. This is part of the motivation behind our combined approach introduced in Sec. 3.2. In the upcoming section we will describe our results, obtained using our novel combined approach.

4.3 Beyond the soft-photon approximation

To test our combined approach described in Sec. 3.2 we considered two physical observables, the missing energy distribution and the photon angular distribution at several kinematic settings. Our Monte Carlo generator produced ten million events per run. The results turned out to be invariant under methods 1, 2, and 3

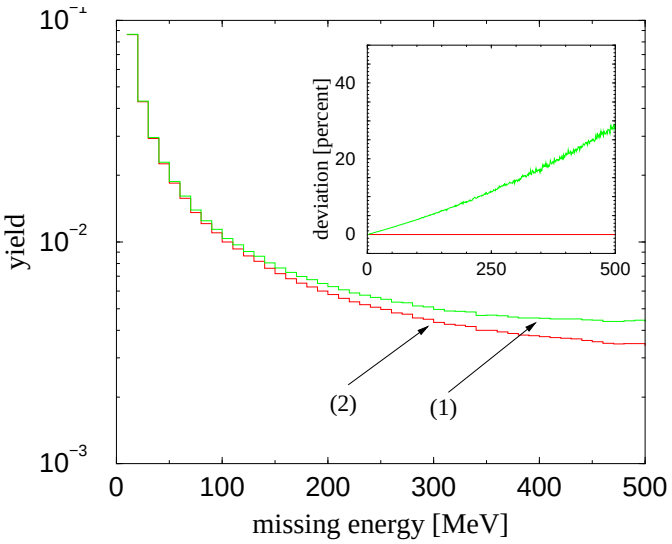

Figure 4.9: Missing energy distribution for multi-photon bremsstrahlung. The colour coding of the curves is as above in Fig. 4.8. At $E_m = 100\,\text{MeV}$ the modified SPA calculation overestimates the radiative tail by 3.9%, at $E_m = 500\,\text{MeV}$ the deviation is 29%. The momentum transfer is $Q^2 = 2.0\,\text{GeV}^2$.

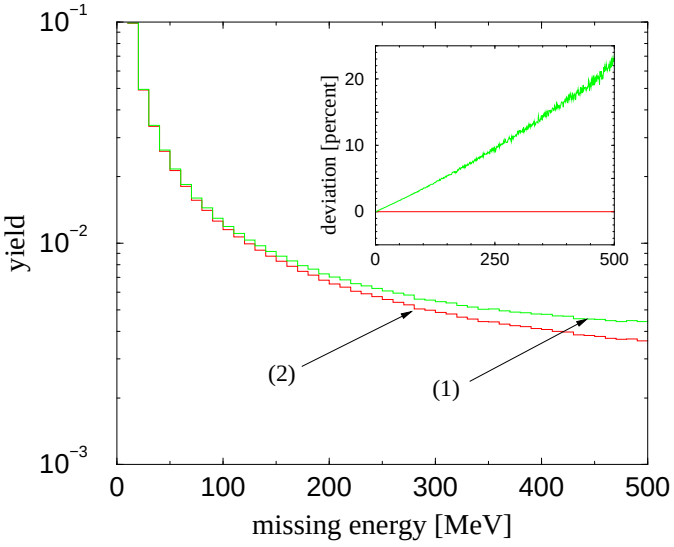

Figure 4.10: Missing energy distribution for multi-photon bremsstrahlung. The colour coding of the curves is as above in Fig. 4.8. At $E_m = 100\,\text{MeV}$ the modified SPA calculation overestimates the radiative tail by 3.5%, at $E_m = 500\,\text{MeV}$ the deviation is 23%. The momentum transfer is $Q^2 = 4.0\,\text{GeV}^2$.

for choosing the hard photon (see Sec. 3.2). Only the random choice of the hard photon (method 4) differed from the other three methods. The results shown in this section have been generated using method 1, which chooses the photon with

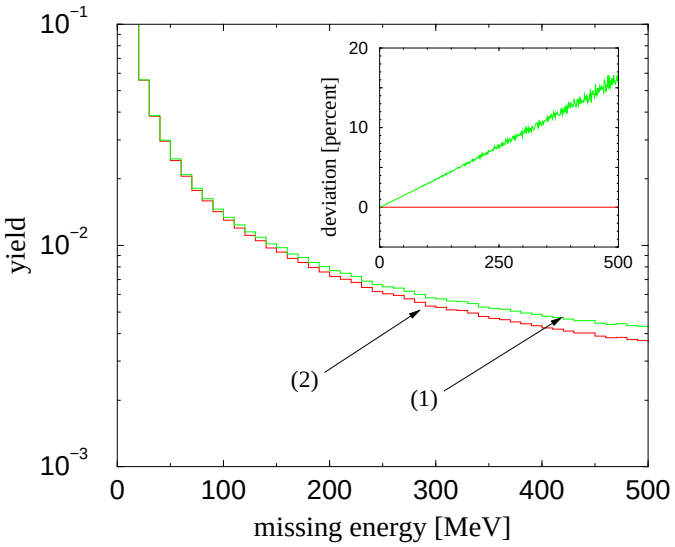

Figure 4.11: Missing energy distribution for multi-photon bremsstrahlung. The colour coding of the curves is as above in Fig. 4.8. At $E_m = 100\,\text{MeV}$ the modified SPA calculation overestimates the radiative tail by 3.0%, at $E_m = 500\,\text{MeV}$ the deviation is 17%. The momentum transfer is $Q^2 = 8.0\,\text{GeV}^2$.

the highest energy as the hard photon.

Figs. 4.8 to 4.11 show the missing energy distributions for multi-photon bremsstrahlung, once calculated by means of the modified SPA (3.21), once calculated in the combined approach (3.20). We clearly see that the modified SPA calculation overestimates the radiative tail. While the deviations between the two calculations are of the order of a few percent for missing energies E_m below $E_m = 100\,\text{MeV}$, the deviations become considerably larger towards the far ends of the radiative tails.

As mentioned earlier, particle detectors are usually configured to detect certain momentum ranges only, depending on what one is looking for. In quasi-elastic $(e, e'p)$ experiments these acceptances are typically set to $\pm 10 - 15\%$ of the central elastic momentum. And, *e.g.*, Rosenbluth measurements only consider events with missing energies below a cut-off of the order of $20 - 50\,\text{MeV}$. Thus events coming from the very far ends of the radiative tails in Figs. 4.8 to 4.11 do not make it into the detectors.

An important question is whether other sources of errors in $(e, e'p)$ experiments dilute the effect of the improved radiative correction treatment presented in this manuscript. On top of radiative corrections, $(e, e'p)$ experiments have to be corrected for *e.g.* finite detector resolution and acceptances, for multiple scattering, and particle decay [53, 55]. In order to put the novel combined

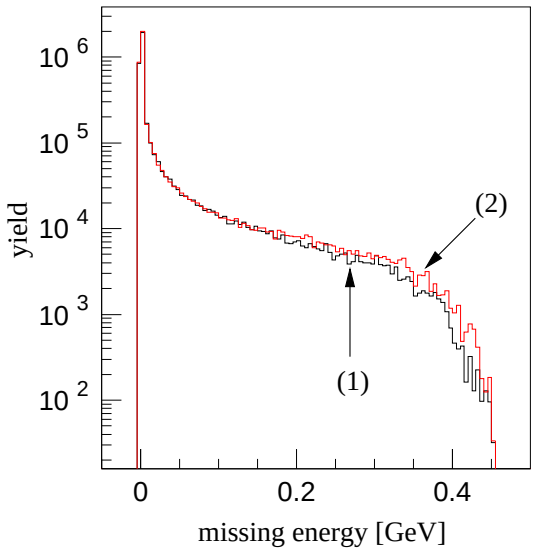

Figure 4.12: Missing energy distribution for multi-photon bremsstrahlung simulated with SIMC. The black curve (1) represents the standard SIMC modified SPA radiative corrections. The red curve (2) shows the E_m distribution obtained by inserting our combined radiative correction approach into SIMC. The latter one has more strength in the radiative tail. The total yield differs by 4.6%. The momentum transfer is $Q^2 = 0.6\,\mathrm{GeV}^2$, as in Fig. 4.8.

Q^2/GeV^2	Δ(100MeV)	Δ(500MeV)
0.6	3.6%	25%
2.0	3.9%	29%
4.0	3.5%	23%
8.0	3.0%	17%

Table 4.2: Deviations between the missing energy distributions (in percent) for four different kinematic settings shown in Figs. 4.8 to 4.11 at two different missing energies.

approach into perspective we inserted our Monte Carlo code into SIMC. In its standard distribution this data analysis code uses a version of the modified SPA which – in contrast to the modified SPA calculation shown in Figs. 4.8 to 4.11 – does not know how to choose a hard photon from a given multi-photon bremsstrahlung event. On top of that SIMC uses the peaking approximation [43, 53].

Figs. 4.12 through 4.15 show the results from the improved version of SIMC (containing the combined approach) and they indicate that the combined approach does have an impact on the missing energy distribution. The radiative

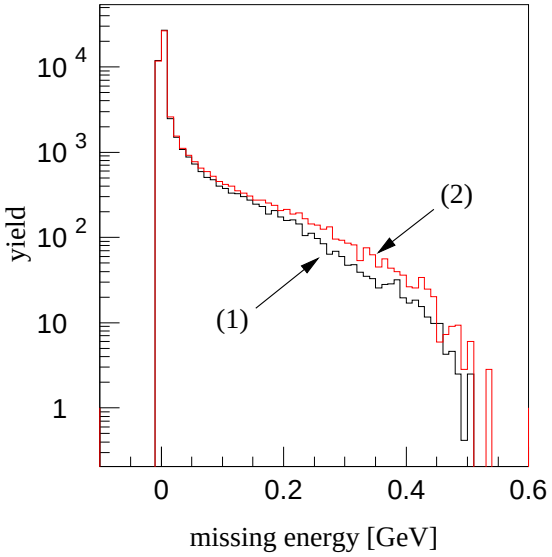

Figure 4.13: Missing energy distribution for multi-photon bremsstrahlung simulated with SIMC. The colour code is the same as in Fig. 4.12. The total yield differs by 2.3%. The momentum transfer is $Q^2 = 2.0\,\mathrm{GeV}^2$, as in Fig. 4.9.

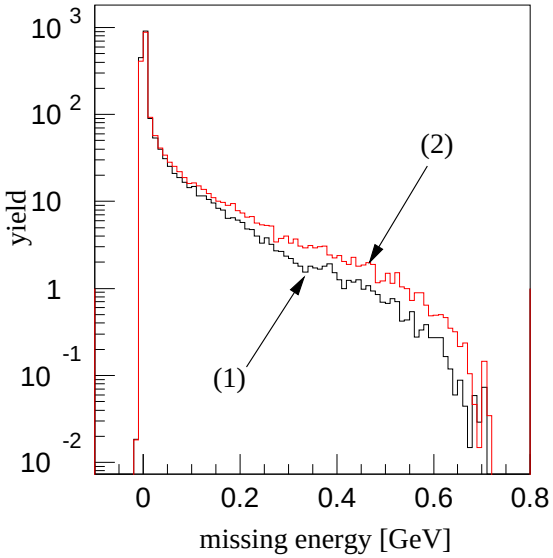

Figure 4.14: Missing energy distribution for multi-photon bremsstrahlung simulated with SIMC. The colour code is the same as in Fig. 4.12. The total yield differs by 1.4%. The momentum transfer is $Q^2 = 4.0\,\mathrm{GeV}^2$, as in Fig. 4.10.

tail calculated using the combined approach inside SIMC is stronger than the radiative tail obtained with the standard SIMC radiative correction procedure for all four kinematic settings under consideration. So removing the SPA partially

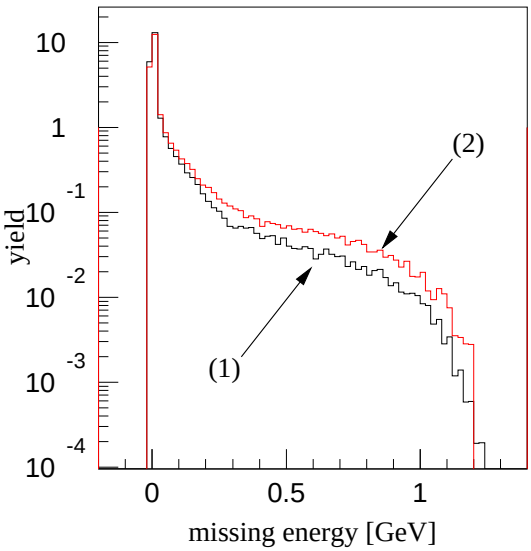

Figure 4.15: Missing energy distribution for multi-photon bremsstrahlung simulated with SIMC. The colour code is the same as in Fig. 4.12. The total yield differs by 1.4%. The momentum transfer is $Q^2 = 8.0\,\mathrm{GeV}^2$, as in Fig. 4.11.

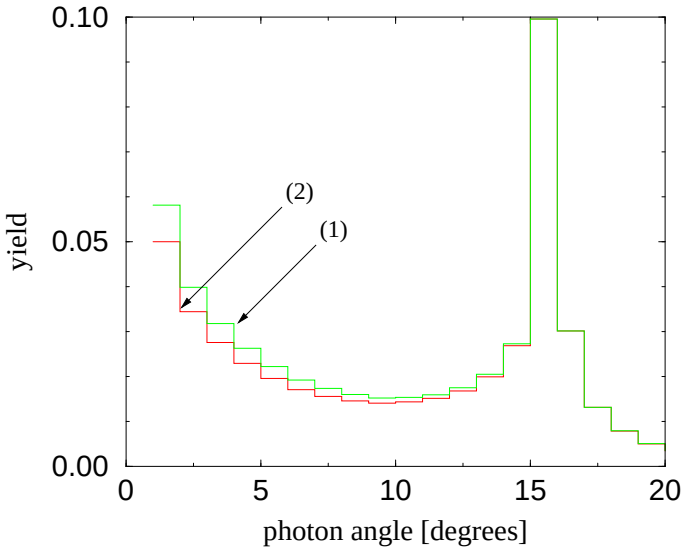

Figure 4.16: Bremsstrahlung angular distribution. The green curve (1) represents the modified SPA, the red curve (2) shows the combined approach. The SPA distribution deviates from the combined calculation especially in the vicinity of the incident electron, around 0^o. The kinematic settings are as in Fig. 4.8.

from data analyses, replacing it by the combined approach, has a considerable effect.

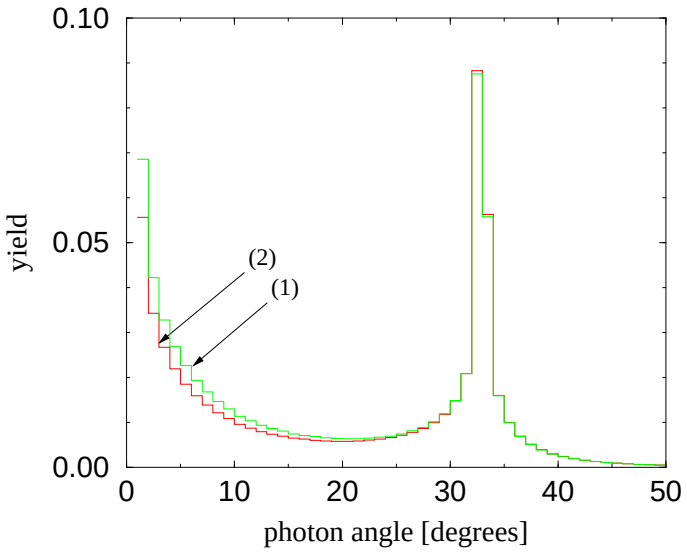

Figure 4.17: Bremsstrahlung angular distribution. The colour code is as in Fig. 4.16. The SPA distribution deviates from the combined calculation especially in the vicinity of the incident electron, around 0^o. The kinematic settings are as in Fig. 4.9.

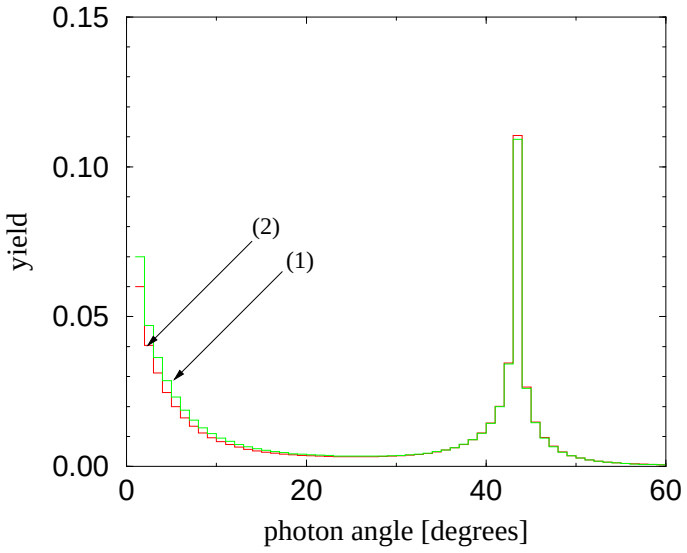

Figure 4.18: Bremsstrahlung angular distribution. The colour code is as in Fig. 4.16. The SPA distribution deviates from the combined calculation especially in the vicinity of the incident electron, around 0^o. The kinematic settings are as in Fig. 4.10.

The angular distributions of the bremsstrahlung photons can be found in Figs. 4.16 to 4.19. For all kinematic settings the modified SPA calculation overestimates the angular distribution in the vicinity of the incident electron,

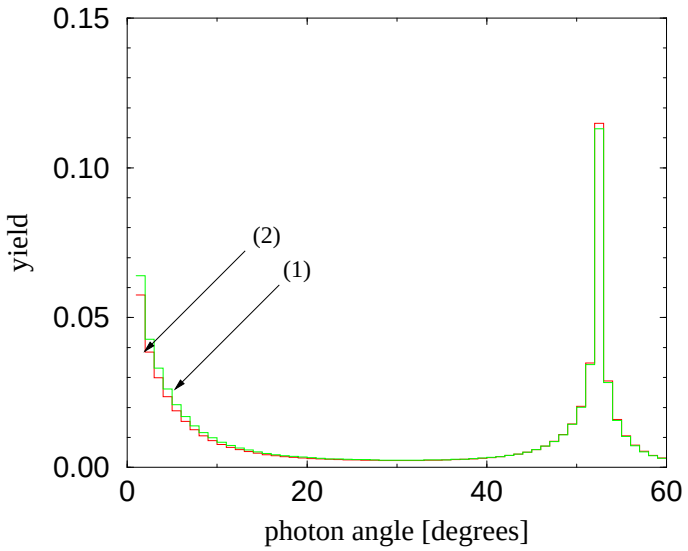

Figure 4.19: Bremsstrahlung angular distribution. The colour code is as in Fig. 4.16. The SPA distribution deviates from the combined calculation especially in the vicinity of the incident electron, around 0^o. The kinematic settings are as in Fig. 4.11.

hence at small angles.

As in the case of the missing energy simulation the question is whether this deviation can be seen in the data, or whether other sources of errors dominate the photon angular distribution. In order to determine the impact of the combined approach on the photon angular distribution we resorted to SIMC, as for the missing energy distribution.

In standard $(e, e'p)$ data analysis codes, like SIMC, the photon angular distribution is approximated using Schiff's peaking approximation [40, 43, 53, 55]. It is clear that the photon angular distribution generated in SIMC's standard radiative correction approach (including the peaking approximation) differs from the combined approach even more than the modified SPA from the combined calculation shown in Figs. 4.16 to 4.19. The peaking approximation and thus the standard SIMC analysis code is to be expected not to describe the experimental angular distribution accurately especially between the two radiation peaks coming from the incident and the scattered electron, as seen in Sec. 4.1. Looking at the photon angular distribution both with the standard SIMC code and with the modified version of SIMC, containing our combined simulation, gives us the opportunity to rate the impact of our approach compared to the standard SIMC radiative correction procedure. Where available, we compared the different approaches to data.

Figs. 4.20 to 4.23 show the photon angular distributions as generated by SIMC.

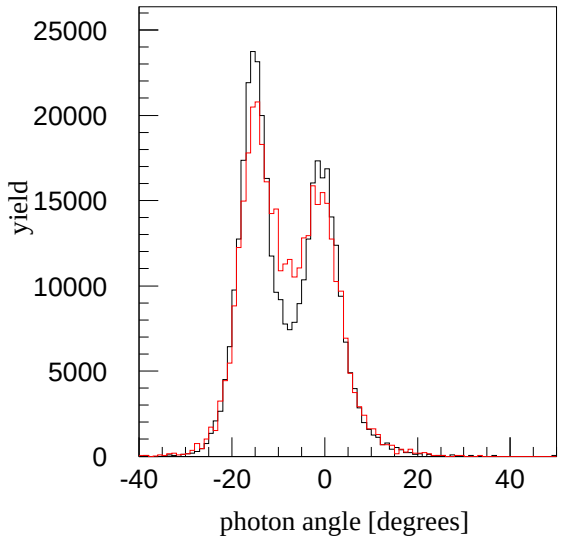

Figure 4.20: Bremsstrahlung angular distribution generated with SIMC. The black curve (1) represents the standard SIMC modified SPA calculation. The red curve (2) shows the angular distribution simulated with the combined approach. The largest difference between the standard SIMC treatment and the data occurs in the middle between the e and the e' directions. The kinematics are the same as in Figs. 4.8 and 4.16.

The largest deviations between the standard SIMC radiative correction and the combined approach appear between the two peaks due to electron (e and e') bremsstrahlung, in contrast to Figs. 4.16 to 4.19, where deviations occur at small angles. This indicates that the photon angular distribution is not affected by the SPA and by the combined approach. The peaking approximation is the dominant source of error, in contrast to the case of the missing energy.

Fig. 4.24 verifies this. One of the kinematic settings has been measured [5, 6], so we are able to compare the combined approach with H$(e, e'p)$ data from the E97-006 experiment at TJNAF. The combined approach (beyond peaking and beyond SPA) and the full angular approach (beyond peaking, but using SPA) lead to very similar results.

This measurement at $Q^2 = 2.0\,\mathrm{GeV}^2$ was subject to a correction accounting for punch-throughs of the proton in the spectrometer collimator, as described in the Sec. 1.3. This feature appears in Fig. 4.24 as a bump in the proton direction. In the proton direction the combined approach falls slightly below the experimental yield, because our combined simulation does not include proton bremsstrahlung.

As indicated in Sec. 3.2 we also included proton bremsstrahlung into our

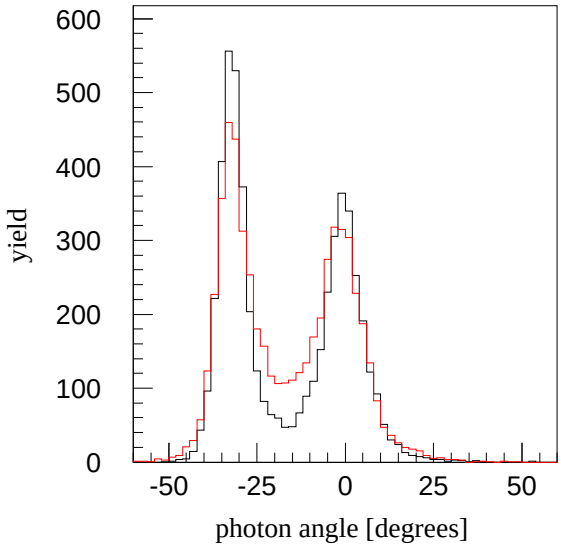

Figure 4.21: Bremsstrahlung angular distribution generated with SIMC. The colour code is the same as in Fig. 4.20. The comparison with experimental data can be found in Fig. 4.24. The kinematics are the same as in Figs. 4.9 and 4.17.

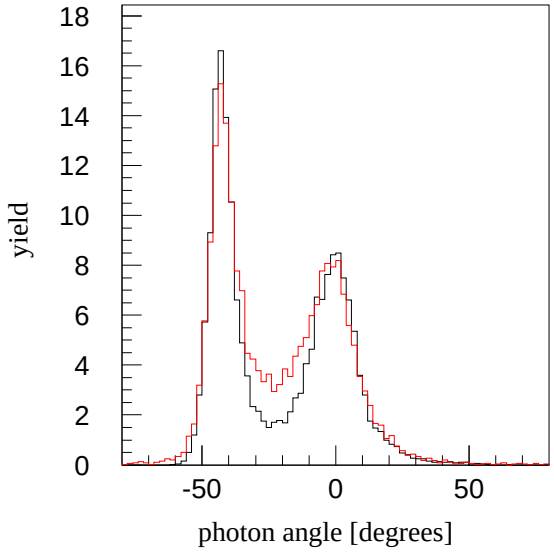

Figure 4.22: Bremsstrahlung angular distribution generated with SIMC. The colour code is the same as in Fig. 4.20 but there was no data available for these kinematic settings. They are the same as in Figs. 4.10 and 4.18.

combined calculation, resorting to the SPA. As a test we generated the

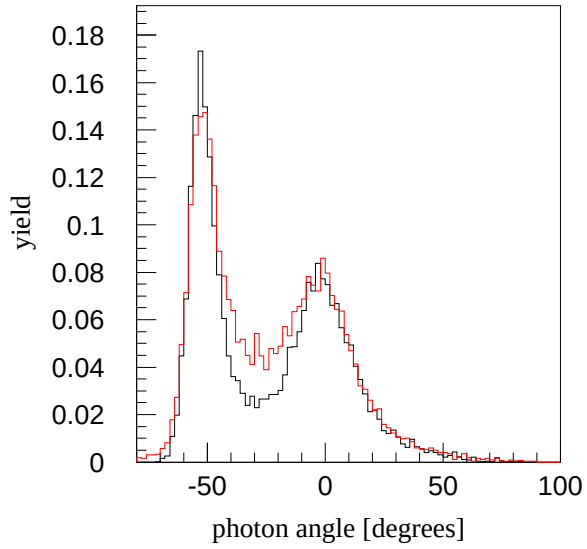

Figure 4.23: Bremsstrahlung angular distribution generated with SIMC. The colour code is the same as in Fig. 4.20 but there was no data available for these kinematic settings. They are the same as in Figs. 4.11 and 4.19.

photon angular distribution using weight (3.23), comparing it to the combined calculation without the proton (3.20). As can be seen in Fig. 4.26 the photon angular distribution is not changed significantly by including SPA proton bremsstrahlung. Just the electron radiation peaks are slightly overestimated when neglecting the proton bremsstrahlung. And the missing energy is not changed at all when including protons (see Fig. 4.27). Thus we conclude that the proton bremsstrahlung is not relevant and that the SPA is a good approximation for proton bremsstrahlung.

We observe that the combined approach reproduces the experimental photon angular distribution in Fig. 4.24 much better than the standard SIMC simulation. And the combined approach presented in this section and the full angular approach from Sec. 4.1 are much closer to each other and to the data than the standard SIMC simulations, indicating again, that removal of the peaking approximation is the relevant improvement for the photon angular distribution. Partial removal of the SPA does not play a role when looking at the photon angular distribution. Hence the peaking approximation is the main source of error for the photon angular distribution, in contrast to the missing energy distribution. Removing the SPA is not relevant for the photon angular distribution. But of course it also does not pose a disadvantage, since the computational expense for the combined method is very moderate. It is at most a factor of 2.

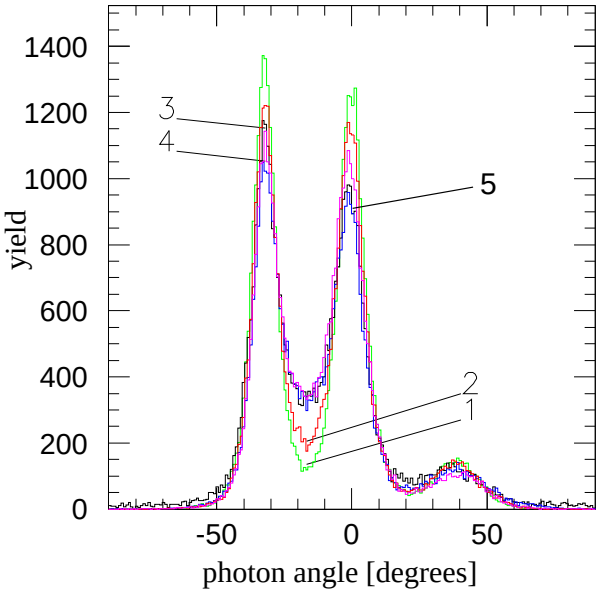

Figure 4.24: Combined approach bremsstrahlung angular distribution generated inside SIMC and compared to data for the kinematics shown in Tab. 1.1. The green (1) and the red curve (2) show standard SIMC photon distributions, both using different versions of the peaking approximation; and the black curve (3) represents the data, as in Figs. 1.4 and 4.1. The magenta line (4) is the new combined approach implemented into SIMC. Additionally there is the blue line (5) from Fig. 4.1 showing a full angular SPA simulation. The combined approach (4) fits the data as well as the full angular approach (5) which can best be seen in Fig. 4.25.

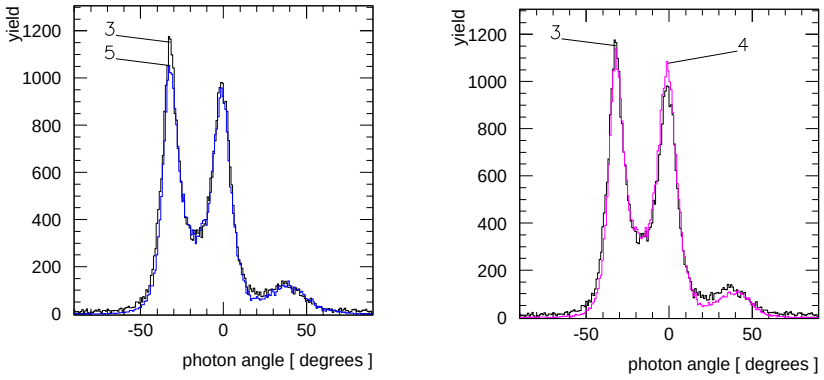

Figure 4.25: Detail of Fig. 4.24. Both histogrammes show the data in black (3) compared to the full angular Monte Carlo simulation in blue (5) on the left; and compared to the combined simulation in magenta (3) on the right.

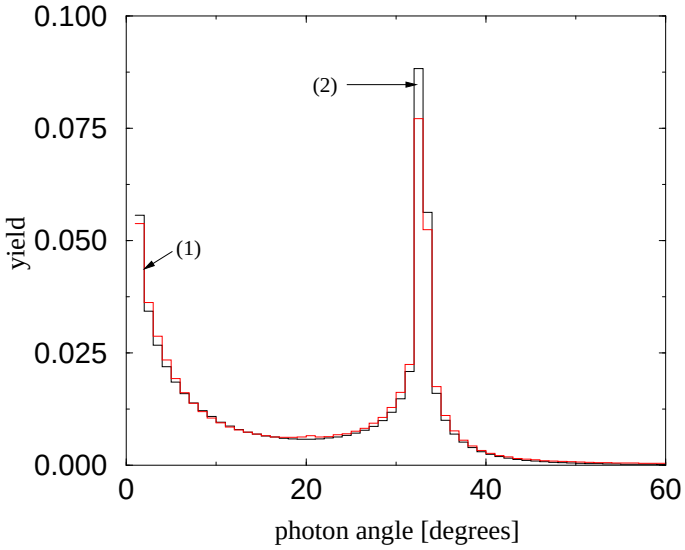

Figure 4.26: Photon angular distribution with (red curve, 1) and without (black curve, 2) SPA proton bremsstrahlung. The simulation neglecting proton bremsstrahlung overestimates the electron peaks slightly. Over the rest of the photon angle domain the two curves coincide.

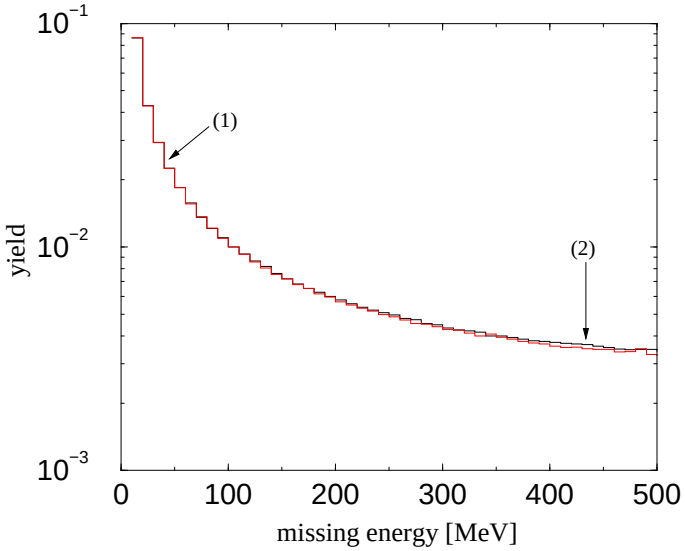

Figure 4.27: Missing energy distribution with (red curve, 1) and without (black curve, 2) SPA proton bremsstrahlung. The two curves are hardly distinguishable.

5 Impact on nucleon form factors

In this chapter we will review the electromagnetic structure of the nucleons, especially focussing on the proton electric form factor. The electric (e) and magnetic (m) form factors of the proton (p) and the neutron (n)$G_{\rm ep}$, $G_{\rm mp}$, $G_{\rm en}$, and $G_{\rm mn}$ are central to an understanding of the nucleons. Traditionally, $G_{\rm ep}$ and $G_{\rm mp}$ have been determined from e-p cross sections using the Rosenbluth technique, *i.e.* by measuring cross sections at constant momentum transfers Q^2 at both forward and backward scattering angles, in order to separate the two. More recently, the polarization technique has been exploited; here, the recoil proton polarization in $\vec{e}$-p scattering is used to obtain the ratio $G_{\rm ep}/G_{\rm mp}$.

In Sec. 5.1 we will discuss the physical interpretation of the nucleon form factors. In Sec. 5.2 we will take a glance at the Rosenbluth technique and at the polarization transfer method, which are apparently leading to contradictory results for $G_{\rm ep}(Q^2)$ for large values of Q^2. Subsequently we will briefly discuss the influence of the TPE in Sec. 5.3. In order to find out whether the combined approach presented in Chap. 3 has an impact on the Rosenbluth data we calculate the so-called reduced cross section in Sec. 5.4, using the combined radiative correction treatment, introduced in Sec. 3.2.

5.1 Introduction to nucleon form factors

In the general introduction to this thesis (see Chap. 1) we discussed already the vertex function Γ_μ. Symmetry considerations (Lorentz invariance, gauge invariance, and parity conservation) lead to the expression presented earlier in Eq. (1.3),

$$\Gamma_\mu \equiv F_1(q^2)\gamma_\mu + \frac{i\kappa F_2(q^2)}{4M}\sigma_{\mu\nu}q^\nu \,. \tag{5.1}$$

The two functions $F_1(q^2)$ and $F_2(q^2)$ contain everything we do not know about the electromagnetic structure of the interaction at the vertex. They are referred to as the Pauli (or Pauli and Dirac) form factors. For the case of an electron exchanging a virtual photon with a proton, the Pauli form factors describe the

proton's internal electromagnetic structure as probed by the exchanged photon. If we chose

$$F_1(q^2) = 1 \text{ and } F_2(q^2) = 0\,, \tag{5.2}$$

we would describe scattering off a point-like Dirac particle. Electron scattering off such a particle without structure (but with mass M, charge $+e$, and spin $1/2$) is called 'Mott scattering'. Let us briefly review the Mott cross section, in order to highlight how the form factors (and thus electromagnetic structure) enters the full calculation. Squaring the first-order Born amplitude (1.2), using (5.2), summing over final spins and averaging over initial spins, finally adding the phase space factors, we obtain the Mott cross section. In the laboratory frame it reads

$$\left(\frac{d\sigma}{d\Omega_{\rm e}}\right)_{\rm Mott} = \frac{\alpha^2}{4\epsilon^2 \sin^4\frac{\theta}{2}} \frac{\epsilon'}{\epsilon} \left(\cos^2\frac{\theta}{2} - \frac{q^2}{2M^2}\sin^2\frac{\theta}{2}\right)\,, \tag{5.3}$$

where θ is the electron scattering angle. For the electron-proton cross section, including the proton's electromagnetic structure we would have to employ the full vertex (5.1), leading to

$$\left(\frac{d\sigma}{d\Omega_{\rm e}}\right)_{\rm ep} = \frac{\alpha^2}{4\epsilon^2 \sin^4\frac{\theta}{2}} \frac{\epsilon'}{\epsilon} \left[\cos^2\frac{\theta}{2}\left(F_1^2 - \frac{\kappa^2 q^2}{4M^2}F_2^2\right) - \frac{q^2}{2M^2}(F_1+\kappa F_2)^2 \sin^2\frac{\theta}{2}\right] \tag{5.4}$$

in the laboratory frame. Defining the linear combinations

$$\begin{aligned} G_{\rm ep} &\equiv F_1 + \frac{\kappa q^2}{4M^2}F_2 \\ G_{\rm mp} &\equiv F_1 + \kappa F_2\,, \end{aligned} \tag{5.5}$$

allows us to write down cross section (5.4) in a slightly more compact way, yielding

$$\left(\frac{d\sigma}{d\Omega_{\rm e}}\right)_{\rm ep} = \frac{\alpha^2}{4\epsilon^2 \sin^4\frac{\theta}{2}} \frac{\epsilon'}{\epsilon} \left(\frac{G_{\rm ep}^2 + \tau G_{\rm mp}^2}{1+\tau}\cos^2\frac{\theta}{2} - \frac{q^2}{2M^2} 2\tau G_{\rm mp}^2 \sin^2\frac{\theta}{2}\right)\,, \tag{5.6}$$

with

$$\tau \equiv -\frac{q^2}{4M^2}\,. \tag{5.7}$$

The functions $G_{\rm ep}$ and $G_{\rm mp}$ are the Sachs form factors. They have a physical interpretation in the Breit-frame. This frame is defined as the frame in which the momentum transfer q has no zeroth component, so the photon is space-like. In this system, we have

$$\mathbf{P} \equiv \mathbf{p} + \mathbf{p}' = \mathbf{0}\,, \tag{5.8}$$

and the static charge distribution can be defined as [58]

$$\rho(\mathbf{r}) = \frac{e}{(2\pi)^3} \int d^3q G_{\mathrm{ep}}(q^2) \exp(iq \cdot r)\,, \tag{5.9}$$

which is just the Fourier transform of the proton electric form factor in the non-relativistic limit, where $\mathbf{q}^2 \ll M^2$. Similarly, in the Breit-frame, using the non-relativistic limit, the proton magnetic form factor can be interpreted as the Fourier transform of a current operator.

The Sachs form factors G_{ep} and G_{em} are called space-like proton form factors. Time-like form factors are measured in e^+e^- collider experiments. The proton time-like form factors are less well known than the space-like ones because of large experimental uncertainties [60].

As a first approximation the two Sachs form factors can be approximated as dipoles [28],

$$G_{\mathrm{d}}(q^2) = \left(\frac{1}{1 - \frac{q^2}{\Lambda^2}}\right)^2\,, \tag{5.10}$$

the term 'dipole' referring to the two poles of this model for the form factors,* and Λ being a constant of the order of 1 GeV. Form factor measurement results are often presented as deviations from the dipole form factor.

5.2 Rosenbluth problem

The form factors G_{ep} and G_{em} can be measured in $(e, e'p)$ experiments using the Rosenbluth separation technique [61]. Defining the variable ε (not related to the photon helicity vector ε_μ from Chap. 1) as,

$$\varepsilon^{-1} \equiv 1 + 2(1+\tau)\tan^2\frac{\theta}{2}\,, \tag{5.11}$$

we can re-write cross section (5.6), obtaining

$$\left(\frac{d\sigma}{d\Omega_{\mathrm{e}}}\right)_{\mathrm{ep}} = \left(\frac{d\sigma}{d\Omega_{\mathrm{e}}}\right)_{\mathrm{Mott}} \frac{\tau G_{e_m}^2 + \varepsilon G_{\mathrm{ep}}^2}{\varepsilon(1+\tau)}\,. \tag{5.12}$$

We further define the so-called reduced cross section,

$$\sigma_{\mathrm{red}} \equiv \left(\frac{d\sigma}{d\Omega_{\mathrm{e}}}\right)_{\mathrm{ep}} \frac{\varepsilon(1+\tau)}{\left(\frac{d\sigma}{d\Omega_{\mathrm{e}}}\right)_{\mathrm{Mott}}}\,. \tag{5.13}$$

*While the term 'dipole' usually refers to a pair of electric charges or magnetic poles of equal magnitude but opposite polarity, separated by some distance, in this case 'dipole' refers to the two zeros ('poles') in the denominator of expression (5.10).

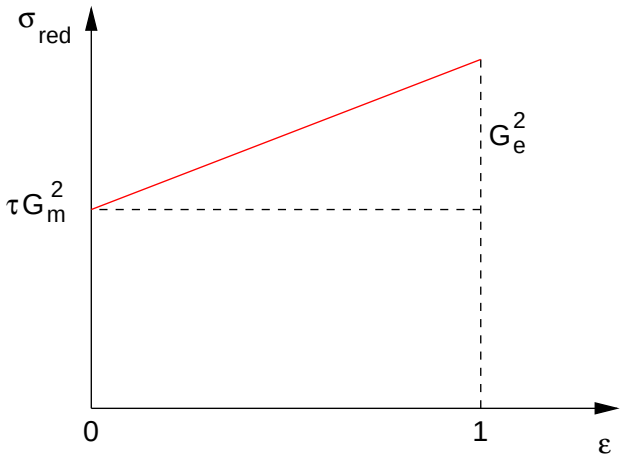

Figure 5.1: Rosenbluth plot of the reduced cross section $\sigma_{\mathrm{red}}(\epsilon)$. The slope equals G^2_{ep}, and the intercept is τG^2_{mp}.

Applying definition (5.13) to the cross section (5.12), the reduced cross section turns out to be a linear function of ε,

$$\sigma_{\mathrm{red}} = \tau G^2_{\mathrm{mp}} + \varepsilon G^2_{\mathrm{ep}} \,. \tag{5.14}$$

The slope of this linear function (see Fig. 5.1) is G^2_{ep} and its intercept equals τG^2_{mp}. For constant q^2, τ also is constant. Comparing forward and backward scattering, each set of such measurements yields one data point of the form factors $G^2_{\mathrm{ep}}(Q^2)$ and $G^2_{\mathrm{mp}}(Q^2)$ at the chosen value of Q^2.

The Rosenbluth separation technique measures G^2_{ep} and G^2_{mp} simultaneously. This poses a problem at higher values of Q^2, where the respective contributions of G_{ep} and G_{mp} to the reduced cross section (5.14) are distributed very un-evenly among the two Sachs form factors. A linear combination of G^2_{ep} and G^2_{mp} is measured, and *e.g.* at $Q^2 = 5\,\mathrm{GeV}^2$, the electric form factor contribution to σ_{red} is down to 8% and it further decreases with increasing Q^2. Hence the slope of the measured reduced cross section (5.14) (see Fig. 5.1) becomes very small and thus very sensitive to systematic errors.

Fig. 5.2 shows results for the proton electric form factor as a function of Q^2 as determined via Rosenbluth separation. Usually, results are presented in units of G_{d}; or they are given in units of $G_{\mathrm{mp}}/\mu_{\mathrm{p}}$, where μ_{p} is the proton magnetic moment. To date all Rosenbluth measurements are compatible with scaling, *i.e.* these experiments indicate that

$$G_{\mathrm{ep}} \sim G_{\mathrm{d}} \,, \tag{5.15}$$

or,

$$G_{\mathrm{ep}} \sim G_{\mathrm{mp}}/\mu_{\mathrm{p}} \,, \tag{5.16}$$

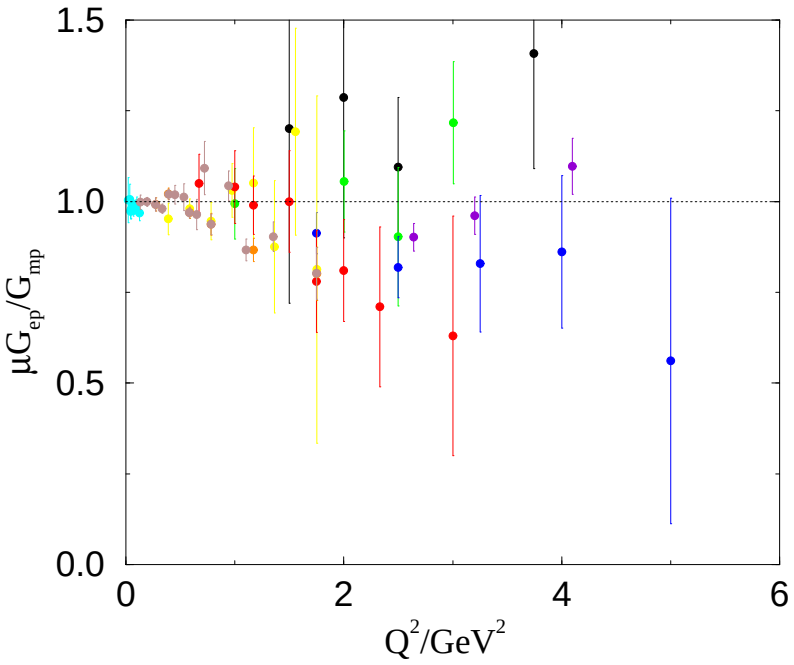

Figure 5.2: World Rosenbluth data (colour version available on-line at [66]). Rosenbluth data from [67] (black), [68] (red), [69] (green), [70] (blue), [71] (brown), [72] (yellow), [73] (violet), [74] (cyan), and [75] (orange). The dashed line represents scaling (5.15). A subset of this data was used for the re-analysis by Arrington in Ref. [22].

respectively.

In contrast to $(e, e'p)$ experiments polarization transfer experiments use polarized electron beams and they measure the struck proton's polarization via a second scattering in the polarimeters. In nuclear physics nomenclature they are denoted as $(\vec{e}, e'\vec{p})$ experiments. The first polarization transfer (or 'recoil polarization') experiment with values of Q^2 large enough to exhibit a discrepancy with the G_{ep} results from Rosenbluth measurements was carried out at TJNAF's hall A in 1998 [62]. It measured a range of Q^2 from $0.5\,\mathrm{GeV}^2$ to $3.5\,\mathrm{GeV}^2$. Swapping the spectrometers, higher momentum transfers up to $5.6\,\mathrm{GeV}^2$ became accessible in a later experiment [63].

The ratio $G_{\mathrm{ep}}\mu_{\mathrm{p}}/G_{\mathrm{mp}}$ is roughly independent of Q^2 according to the measurements using the Rosenbluth technique, whereas according to the polarization transfer method the same ratio seems to fall approximately linearly with Q^2, reaching a value of 0.2 at $Q^2 = 6\,\mathrm{GeV}^2$. A linear fit to the polarization transfer data yields [63]

$$\mu_{\mathrm{p}} G_{\mathrm{ep}}/G_{\mathrm{mp}} = 1 - 0.13(Q^2 - 0.04)\,, \tag{5.17}$$

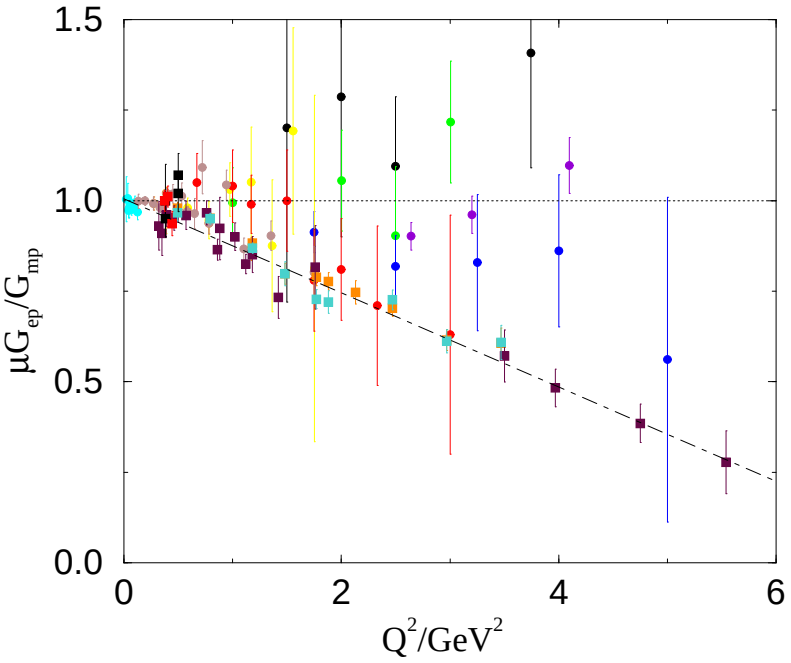

Figure 5.3: Proton electric form factor as obtained via Rosenbluth analysis of cross sections (circles) and polarization transfer method (squares) (colour version available on-line at [83]). This plot shows the world Rosenbluth data together with the world polarization transfer data. For a list of references please refer to [84]. The dashed line represents scaling (5.15), the dot-dashed line represents the fit (5.17) to the polarization transfer data. The discrepancy becomes manifest when fitting the two data sets.

which is shown in Fig. 5.3, together with the Rosenbluth data. Subsequent to the discovery of this discrepancy [62, 63] an improved Rosenbluth measurement (dubbed 'SuperRosenbluth') was carried out at TJNAF's hall C [64, 65]. In order to reduce radiative corrections and systematic uncertainties due to beam fluctuations the SuperRosenbluth experiment measured the inclusive H(e,p) cross section. In an effort to overcome the discrepancy between (5.17) and the scaling (5.15) and (5.16), the world Rosenbluth data was re-analyzed [22, 76] (see Fig. 5.2) as well as the world polarization transfer data. Neither Rosenbluth data nor polarization transfer data showed any internal inconsistencies. Hence the discrepancy was manifest.

5.3 Two-photon exchange contribution

The discrepancy has led to several attempts aiming at an understanding. In particular, the works of Blunden *et al.* and Guichon and Vanderhaeghen [29, 30, 77] evoke the contribution of TPE processes (see Fig. 1.3). Blunden *et al.* find about half the required contribution when calculating the TPE contribution

using as intermediate state the proton ground state only. Calculations involving *all* intermediate states are only available from generalized parton distribution (GPD) calculations, relating them to virtual Compton processes on the nucleon, being valid only for large values of Q^2 [88–90]. GPD combine form factors with structure functions (parton densities) and can *e.g.* be obtained from lattice calculations. Hadronic TPE calculations are still model dependent and only valid for small and intermediate values of Q^2. But recently the Delta resonance Δ has been included into the hadronic TPE calculations [78].

One well known TPE effect is the Coulomb distortion of the electron waves, which corresponds to the exchange of one hard and one (or more) soft photon(s) between the electron and the target nucleus. While systematically neglected in the past (for exceptions see [79–81]) the inclusion of Coulomb distortion in the Rosenbluth separation does have a significant effect even at large Q^2: it changes G_{ep} downward by typically one standard deviation [82]. The effect, however, is not big enough to fully explain the discrepancy between the Rosenbluth technique and the polarization transfer method.

Finite TPE contributions to radiative corrections are usually neglected in $A(e, e'p)$ experiments ($A > 1$), since they constitute a very minor correction only. The Rosenbluth technique, however, is very sensitive even to small corrections depending systematically on the variable ε from Eq. (5.11). The TPE does depend on ε and due to the small slopes of the typical Rosenbluth plots (see Fig. 5.1) the minor TPE correction is magnified by the Rosenbluth technique by roughly two orders of magnitude, rendering the underlying Born approximation invalid [29].

The ε-dependence of the TPE contribution is a 2% effect with small non-linearities towards small values of ε and a weak dependence on Q^2 [29]. Thus it destroys the linearity of the Rosenbluth plot. But while the proton TPE contribution bends the reduced cross section (5.13) in one direction, consideration of the Δ resonance bends it into the other, thus partially restoring the linearity (5.14) [78, 85]. Experimentally there are no indications for a non-linearity in the Rosenbluth plots [86]. However, the experimental uncertainties are large, such that the absence of non-linearities in the data does not rule out large TPE effects. Ref. [87] shows experimental constraints on the TPE induced non-linearities.

Yet, the TPE correction to the reduced cross section as measured by the Rosenbluth technique cannot be calculated to a satisfactory accuracy. And another questions is whether there are further corrections, also exhibiting an ε-dependence, which could again be magnified by the Rosenbluth technique. To date the TPE correction is believed to account for roughly 50% of the discrepancy between the two experimental techniques, shown in Fig. 5.3.

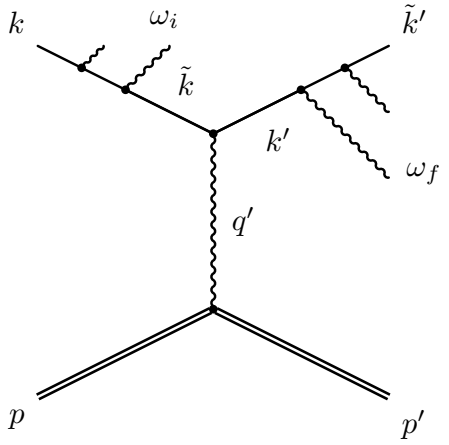

Figure 5.4: Momentum nomenclature for multi-photon bremsstrahlung process. The two photon lines originating from the incident electron (left) symbolize multi-photon emission from the incident electron with *total* momentum ω_i. The two photon lines originating from the scattered electron (right) symbolize multi-photon emission from the scattered electron with *total* momentum ω_f.

The difference between the values of G_{ep} from the Rosenbluth method compared to the polarization technique has led to many proposals for experimental investigations, and several accepted experiments at TJNAF, aiming at studying two-step processes. The perhaps most clean tool, use of *positron* scattering, unfortunately is not yet practical, given the absence of suitable positron beams.

In order to check whether the improved radiative correction treatment presented in this thesis has an impact on the reduced cross section (5.13) and thus on the discrepancy, we applied our combined radiative correction approach to typical Rosenbluth kinematic settings.

5.4 σ_{red} using improved radiative corrections

In this section we will apply our improved radiative correction procedure, introduced in Chap. 3 of this thesis, to $(e, e'p)$ Rosenbluth measurements in order to find out whether they have an impact on the reduced cross section (5.13) and hence on G_{ep}.

To that end we need Rosenbluth data for the proton electric form factor G_{ep}, because we have to reproduce Rosenbluth plots which are then re-computed using our combined radiative correction approach. An empirical fit to the world

Rosenbluth data is given in Ref. [91]. We use it to plot the reduced cross section (5.13) for three kinematic settings with $Q^2 = 2.0\,\mathrm{GeV}^2$, with $Q^2 = 4.0\,\mathrm{GeV}^2$, and $Q^2 = 6.0\,\mathrm{GeV}^2$.

The comparison between existing $(e, e'p)$ Rosenbluth results with a calculation based on our new combined approach is done by multiplying the reduced cross section (5.13) with a correction factor accounting for the differences between the two radiative correction treatments. Therefore, as for the calculations shown in Sec. 3.2, we assigned two weights to each event, one being the $n\gamma$ combined weight (3.20) and another one accounting for the standard radiative corrections in SIMC [40, 53], given by

$$w_{n\gamma}^{\mathrm{simc}} \equiv \frac{|\mathcal{M}_{\mathrm{Born}}^{(1),\mathrm{simc}}|^2 A_{\mathrm{simc}}(\omega_i)}{|\mathcal{M}_{\mathrm{Born}}^{(1)}|^2 A(\omega_{\mathrm{hard}}) A(\omega_1) ... A(\omega_{n-1})} \,. \tag{5.18}$$

$A_{\mathrm{simc}}(\omega_i)$ accounts for the incident electron's bremsstrahlung only, ω_i is the sum of the bremsstrahlung photons emitted by the incident electron e (see Fig. 5.4). The denominators of the two weights (3.20) and (5.18) are identical, of course, since the two weights are applied to the same multi-photon distributions generated with the same SPA Monte Carlo generator. The numerator re-weights the SPA Monte Carlo generator to the SIMC event generation. In its standard version, SIMC uses both the peaking approximation and the SPA. The scattering process including bremsstrahlung is understood to be a two-step process. Initially, the incident electron with momentum $k = (\epsilon, \mathbf{k})$ emits several bremsstrahlung photons with total four-momentum ω_i, all of them aligned with the vector $\mathbf{k}$. So the electron's momentum at the vertex is

$$\tilde{k} = k - \omega_i \,, \tag{5.19}$$

and it is assumed to be on-shell, *i.e.* $\tilde{k}^2 = m^2$. After this first step the momentum transfer to the proton, q', is calculated and inserted into the form factors. It includes the energy loss due to bremsstrahlung from the initial electron. Then, in a second step, the scattered electron's energy, ϵ', is calculated and eventually this scattered electron emits further bremsstrahlung photons with total four-momentum ω_f (see Fig. 5.4). Again, all of these photons emitted by the scattered electron $k' = (\epsilon', \mathbf{k}')$ are aligned with $\mathbf{k}'$ in the standard version of SIMC.

SIMC calculates the form factors taking into account bremsstrahlung from the incident electron only. Bremsstrahlung from the scattered electron just reduces k',

$$\tilde{k}' = k' - \omega_f \,, \tag{5.20}$$

which becomes relevant for the detector simulations. But SIMC does not correct the form factors and the momentum transfer q' for bremsstrahlung from the

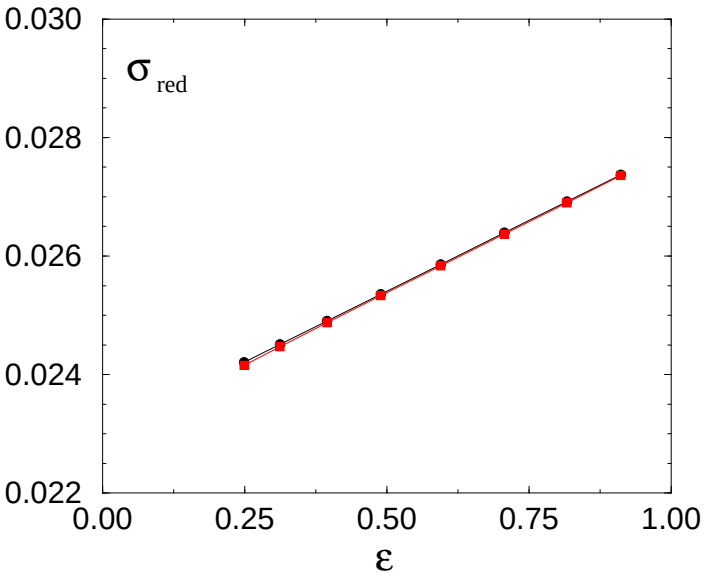

Figure 5.5: Reduced cross section for $Q^2 = 2.0\,\mathrm{GeV}^2$. The black line (circles) shows a calculation following the standard SIMC radiative correction treatment. The red line (squares) represents the combined approach. The difference between the two curves is negligible.

scattered electron, ω_f. Hence, in the numerator of the weight (5.18) the first-order Born matrix element $\mathcal{M}^{(1),\mathrm{simc}}_{\mathrm{Born}}$ is calculated using

$$q' = \tilde{k} - k' \,. \tag{5.21}$$

And kinematic modifications due to bremsstrahlung emission from the incident electron are taken into account by $A_{\mathrm{simc}}(\omega_i)$ [40, 53], as shown in eq. (5.18).

In contrast to the results presented in the previous Chapter we included a 'detector simulation' into our combined code used to generate the Rosenbluth plots. This detector simulation simply assumed the detectors to be rectangular windows and it constrained their momentum acceptances. In case the SIMC like radiation procedure described above lead to particle momenta not seen by the detectors, $w^{\mathrm{simc}}_{n\gamma}$ was set to zero; and in case our combined approach lead to particles outside the detector acceptances, the weight $w^{\mathrm{ex}}_{n\gamma}$ was set to zero.

In order to compare the two approaches the missing energy was considered, binning the two weights (3.20) and (5.18) in the vicinity of the total missing energy for each event. As $(e, e'p)$ Rosenbluth experiments only consider the elastic peak of the missing momentum E_{m} up to energies of the order of $20 - 50\,\mathrm{Mev}$, we integrated the two missing energy distributions, obtaining the two total cross sections

$$\sigma^{\mathrm{ex}}_{\mathrm{tot}}(E_{\mathrm{m}} \leq 50\,\mathrm{MeV})\,, \tag{5.22}$$

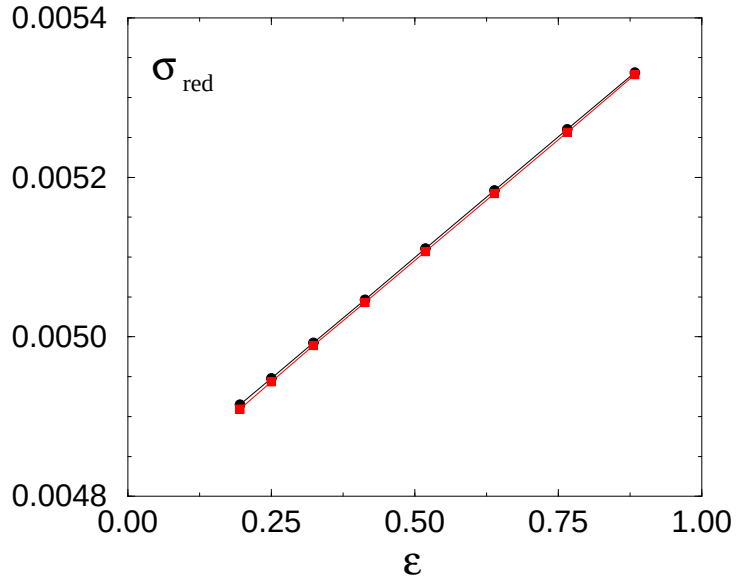

Figure 5.6: Reduced cross section for $Q^2 = 4.0\,\mathrm{GeV}^2$. The black line (circles) shows a calculation following the standard SIMC radiative correction treatment. The red line (squares) represents the combined approach. The difference between the two curves is negligible.

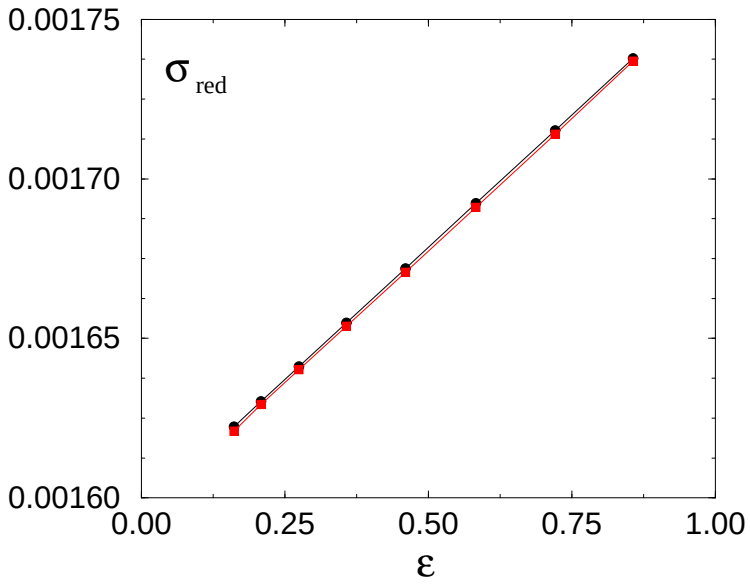

Figure 5.7: Reduced cross section for $Q^2 = 6.0\,\mathrm{GeV}^2$. The black line (circles) shows a calculation following the standard SIMC radiative correction treatment. The red line (squares) represents the combined approach. The difference between the two curves is negligible.

Q^2	$(G_{\mathrm{ep}}^{\mathrm{simc}})^2$	$(G_{\mathrm{ep}}^{\mathrm{ex}})^2$	deviation
$2.0\,\mathrm{GeV}^2$	4.772×10^{-3}	4.816×10^{-3}	+0.92%
$4.0\,\mathrm{GeV}^2$	6.055×10^{-4}	6.081×10^{-4}	+0.43%
$6.0\,\mathrm{GeV}^2$	1.660×10^{-4}	1.662×10^{-4}	+0.12%

Table 5.1: Impact of the improved radiative corrections on the proton electric form factor. The experimental errors on G_{ep}^2 usually are large such that the deviations shown in this table are totally invisible.

and

$$\sigma_{\mathrm{tot}}^{\mathrm{simc}}(E_{\mathrm{m}} \leq 50\,\mathrm{MeV})\,. \tag{5.23}$$

These cross sections were used to correct the standard SIMC reduced cross section (5.13) by multiplying with a correction factor,

$$\sigma_{\mathrm{red}}^{\mathrm{ex}}(\varepsilon) = \frac{\sigma_{\mathrm{tot}}^{\mathrm{ex}}(E_{\mathrm{m}} \leq 50\,\mathrm{MeV})}{\sigma_{\mathrm{tot}}^{\mathrm{simc}}(E_{\mathrm{m}} \leq 50\,\mathrm{MeV})}\sigma_{\mathrm{red}}(\varepsilon)\,. \tag{5.24}$$

The results are presented in Figs. 5.5 to 5.7. As one can see the correction factor (5.24) is so close to unity for all three kinematic settings considered that almost no effect can be seen. Given the large errors usually appearing in Rosenbluth measurements we can conclude here, that the combined approach to radiative corrections has no visible impact on $(e, e'p)$ Rosenbluth measurements. The slopes of the three Rosenbluth plots are given in Tab. 5.1. The corrections to the original values of G_{ep}^2 (obtained using both the peaking approximation and the SPA) are extremely small.

The case of the inclusive (e, p) SuperRosenbluth measurement is more elaborate since the scattered electron's momentum would have to be generated very efficiently in an additional Monte Carlo generator. But as the (e, p) SuperRosenbluth measurement did not deviate from earlier world $(e, e'p)$ Rosenbluth data, an improved radiative correction procedure as presented in this thesis would lead to corrections similarly small as (or even smaller than) the corrections shown in Tab. 5.1.

6 Conclusion and outlook

Having removed both the peaking approximation and the SPA we will now briefly discuss the impact of these improvements. An interesting loose end will be presented in connection with the G_{ep}-discrepancy.

6.1 Advantage of removing peaking approximation and SPA

Using a full angular Monte Carlo simulation of multi-photon bremsstrahlung at almost no extra computational expense improves the treatment of internal bremsstrahlung in $(e, e'p)$ experiments considerably. The problems of the peaking approximation, the underestimation of bremsstrahlung between the radiation peaks and the *ad hoc* split of the non-peaked strength, are solved by our approach. The peaking approximation has been removed and the full angular Monte Carlo code has been inserted seamlessly into SIMC, a much used data analysis code for $(e, e'p)$ experiments at TJNAF.

We also inserted the full angular treatment into a version of the SIMC code designed to analyze $p(e, e'p)\pi^0$ experiments, dubbed SIMC-SEMI, by Mark Jones from TJNAF. The peaking approximation employed in the standard version of SIMC-SEMI is especially problematic for $p(e, e'p)\pi^0$ experiments [92]. Unfortunately the results of the full angular data re-analysis were not yet available at the time this thesis was finished.

Studying the effects of removing the peaking approximation from $(e, e'p)$ data analyses we realized that there was room for further improvement. Both the kinematic effect of bremsstrahlung and the evaluation of the form factors at the modified momentum transfer raised questions as to the consistency and to the accuracy of standard $(e, e'p)$ radiative corrections. In order to address that problem we decided to improve the treatment of bremsstrahlung in a more general context and, in addition to the peaking approximation, we partially removed the SPA from multi-photon bremsstrahlung processes.

In order to do so we treated one hard photon from a given multi-photon emission event exactly, calculating the full 1γ QED matrix element squared. We tried out different methods of selecting the hard photon. Three of these methods were motivated by the physics of radiative corrections. The first one addressed the question of the validity of the SPA. And the two other ones were inspired by Borie and Drechsel's approach to bremsstrahlung [56, 57], focussing on the evaluation of the form factor at the modified momentum transfer q^2. Our results turned out to be invariant under these three methods, whereas a random selection of the 'hard' photon did not yield good results.

First we compared our combined method to a modified multi-photon SPA calculation, looking at the missing energy distribution. The modified SPA overestimated the radiative tail for different kinematic settings. In order to check whether the combined treatment still had an impact when considering additional experimental corrections we inserted our combined calculation into an existing data analysis code (SIMC), in its standard version using the peaking approximation and a version of the modified SPA, in addition to other corrections [40, 53]. We showed that our combined approach had an impact on the missing energy distribution and that it was not washed out by other corrections that need to be applied to data. The computational expense of the combined method was small, at most a factor of 2, compared to the standard SIMC version.

Similarly, we showed that the photon angular distribution was overestimated by the modified SPA especially at small angles, in the vicinity of the incident electron. Inserting our combined approach into SIMC we saw large deviations between the standard SIMC photon angular distribution and our combined approach. The bulk of this difference turned out to be due to the peaking approximation, as expected.

In conclusion we can say, that the removal of the peaking approximation improved the photon angular distribution considerably. The simulated angular distributions came very close to distributions reconstructed from data, in contrast to distributions obtained using the peaking approximation. And partial removal of the SPA had a large impact on the missing energy distribution. This improvement was not washed out by other experimental sources of errors. The combined approach as implemented in the improved version of SIMC contains both improvements, of course.

Our combined approach goes beyond both the peaking approximation and the soft-photon approximation and it treats both the kinematic impact of multi-photon bremsstrahlung and the evaluation of the form factors at modified momentum transfers much more systematically than previous $(e, e'p)$ radiative correction considerations. Since it has been embedded into SIMC, it is available for

$(e, e'p)$ data analyses at TJNAF.

6.2 G_{ep}-problem

While our improved radiative corrections had no sizeable impact on the Rosenbluth plots and thus on G_{ep} as determined by the Rosenbluth separation technique, there is a very interesting loose end in connection with the proton form factor measurements which is worthwhile to discuss.

Initial-state radiation (ISR) experiments (also called 'radiative return') could provide independent measurements of G_{ep}^2 and G_{mp}^2 by measuring angular distributions. ISR experiments study the

$$e^+e^- \to \gamma p\bar{p} \tag{6.1}$$

reaction, the photon γ coming from either the electron or the positron. The matrix element including ISR is down by a factor of $\mathcal{O}(\alpha)$ compared to the process without radiation. But this is compensated for by huge luminosities of the so-called 'meson factories' like DAϕNE, CESR, PEP-II, and KEK-B [60, 93]. The hardest ISR photon usually is detected and its angular distribution is found to be mostly aligned with the electron or the positron [94]. But softer ISR photons constitute a considerable background. Another source of error is final-state radiation (FSR) which can partially be removed by suitably chosen cuts and by simulations. FSR seems to be negligible for $p\bar{p}$ production, except in the region close to the threshold, where the Coulomb interaction gets important [60]. ISR has been included into e^+e^- data analyses to next-to-leading order (NLO) using the PHOKHARA Monte Carlo generator. Originally designed for two-pion and two muon production, it has been made available for $p\bar{p}$ production recently [60, 95]. A similar code named AMEGIC++ also contains SPA radiative corrections [96].

It would be interesting to carry our combined bremsstrahlung approach over to ISR experiments. Multi-photon ISR corrections could be treated similarly to the combined multi-photon bremsstrahlung calculation presented in Sec. 3.2. One could identify one hard ISR photon which would enter the exact QED calculation; and the remaining photons would be accounted for resorting to the SPA.

Acknowledgements

I would like to gratefully acknowledge the enthusiastic supervision of this thesis by Prof. Dr. Dirk Trautmann. He was very helpful, very encouraging, and he always kept the spirits up. He gave me the opportunity to join his group in May 2002 and on no occasion did I regret my decision to accept his kind offer.

I also want to thank Prof. Dr. Ingo Sick. His ideas, his input, and his concepts were very inspiring and very helpful. I enjoyed our enriching discussions a lot. And I want to thank him especially for sharing his deep insights into the Rosenbluth topic with me.

I am deeply indebted to Dr. Kai Hencken who helped me through the twists and turns of both relativistic field theory and effective coding. Without him, without his thesis directions, his patience and his support this thesis would be considerably poorer. He always had time for discussions, though he was exposed to a lot of questions by myself, as we shared the office. And even after he left our group in autumn 2005 he found a lot of time indeed for very fruitful discussions.

Dr. Daniela Rohe helped me a lot with the computer code SIMC and with radiative correction issues. Though I also confronted her with numerous hideous questions she always had time to help.

Also, I want to thank Prof. Dr. Gerhard Baur who joined several group discussions on bremsstrahlung. And I want to thank him for his nice lectures on QED and various aspects of nuclear physics.

And I am grateful to Dr. John Arrington, Prof. Dr. Paul Ulmer, and to Dr. Mark Jones for very useful hints on SIMC, SIMC-SEMI and MCEEP.

This institute's social life would not be the same without the "French Mafia" from the second floor. I will miss the Monday Aperos where I learnt a lot about agrarian products from *la grande nation*. And I especially wish Dr. Cédric

Carasco all the best for his future in Cadarache.

I will also miss the monthly graduate days in the EUROGRAD frame work. They provided a nice and broad overview over many nuclear physics topics. And it was nice to meet the Ph.D. students from Tübingen.

I want to thank Sven Lammers and Alekos Tsamaloukas for very enjoyable football evenings. Maybe Greece will qualify again for the European Championship in 2008. I am very grateful for Alekos' help on various LaTeX style files and classes and on bicycle tuning!

Last but not least I want to thank my clan for notorious moral and financial support and for the annual Advent season supply management. Once I have submitted this thesis, I will take part in the family's activities more often. Ceydaya sabrı için çok çok teşekkür ederim.

Basel, Switzerland, May MMVI
Florian Weißbach

A Bethe-Heitler cross section

In this Appendix, which has been added for entirely educational purposes since it just follows the calculations in Refs. [42, 97], adding details occasionally, we want to calculate the cross section for an electron being scattered off an external Coulomb potential, emitting a soft bremsstrahlung photon at the same time. And we will also caluclate the internal radiative corrections. Scattering off a potential is rather easy compared to *ep*-scattering, for instance, since the energies of the incident electron, E, and the outgoing electron, E', are the same. Thus the exchanged four-momentum, q^2, simply is

$$Q^2 \equiv -q^2 = \mathbf{q}^2 \,. \tag{A.1}$$

The cross section for the soft bremsstrahlung is infrared-divergent, the divergence is cancelled by the vertex correction.

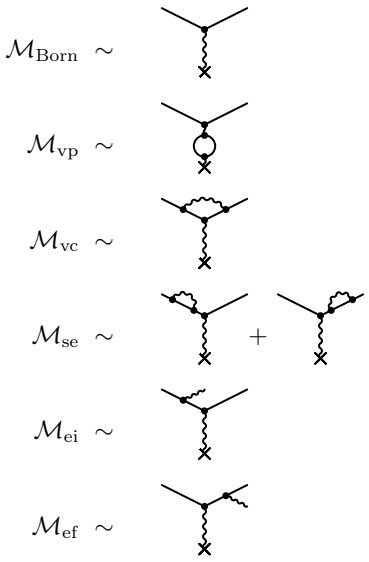

Figure A.1: Feynman diagrams beyond leading order for the Bethe-Heitler process. 'Born' ist short hand for first-order Born amplitude, 'vp' is vacuum polarization, 'vc' is vertex correction, 'se' is self-energies, 'ei' is incident electron bremsstrahlung, and 'ef' is scattered electron bremsstrahlung.

A.1 Feynman diagrams

The two Feynman diagrams for the Bethe-Heitler bremsstrahlung process ($\mathcal{M}_{\rm ei}$ and $\mathcal{M}_{\rm ef}$) are shown in Fig. A.1. When integrating over the energy of the bremsstrahlung photon, ω, the cross section diverges in the limit as $\omega \to 0$. So does the contribution to elastic electron scattering from the vertex correction $\mathcal{M}_{\rm vc}$ (see Fig. A.1). Looking at the various contributions more consistently, we have to calculate

$$|\mathcal{M}_{\rm Born} + \mathcal{M}_{\rm vc} + \mathcal{M}_{\rm vp}|^2 + \int d\omega \, |\mathcal{M}_{\rm ei} + \mathcal{M}_{\rm ef}|^2 \; . \tag{A.2}$$

The self energy amplitudes $\mathcal{M}_{\rm se}$ do not contribute because they are reducible, 'vp' is short hand for vacuum polarization.

Expanding the term on the left of Eq. (A.2) to order α^3 or e^6, we obtain the following matrix element squared in cartoon like decomposition,* namely

$$\left.\frac{d\sigma^{(2)}}{d\Omega_{\rm e}}\right|_{\rm total} \sim 2\mathcal{M}^{\star}_{\rm Born}\mathcal{M}_{\rm vc} + 2\mathcal{M}^{\star}_{\rm Born}\mathcal{M}_{\rm vp} + \int d\omega \, |\mathcal{M}_{\rm bs_i} + \mathcal{M}_{\rm bs_f}|^2 \; . \tag{A.3}$$

In order to get the unpolarized cross section we sum over final spin states (which will usually be denoted by s'), and we average over initial spins (s).

A.2 The various amplitudes and cross sections

For purely elastic electron scattering off an external field we have

$$\mathcal{M}_{\rm Born} = \frac{-iZe^2}{|\mathbf{q}|^2}\bar{u}_a(p',s')\gamma^0_{ab}u_b(p,s) \, , \tag{A.4}$$

where the four-vectors p and p' denote initial and final four-momentum of the electron. The three-momentum $\mathbf{q}$ comes from the external field $A_0^{\rm ext}(x)$, and it is the momentum that is transfered from the Coulomb field to the electron. From Eq. (A.4) we get

$$\begin{aligned} \frac{1}{2}\sum_{s,s'}|\mathcal{M}_{\rm Born}|^2 &= \frac{Z^2e^4}{|\mathbf{q}|^4}\frac{1}{2}{\rm tr}[(\not{p}+m)\gamma^0(\not{p}'+m)\gamma^0] \\ &= \frac{Z^2e^4}{|\mathbf{q}|^4}\left[4EE' - 2(p\cdot p') + 2m^2\right] = \frac{Z^2e^4}{|\mathbf{q}|^4}\left[4E^2 + \mathbf{q}^2\right] \, , \end{aligned} \tag{A.5}$$

*This equation is not exact because the various amplitudes describe different final states $\langle f|$. Also the integration measure is not exact, as in Eq. (A.2).

because $E = E'$, as we are considering elastic scattering only. Introducing the variables $\beta \equiv |\mathbf{p}|/E$ we can write

$$p' \cdot p = E^2 - \mathbf{p}^2 \cos\theta = m^2 + 2E^2\beta^2 \sin^2\frac{\theta}{2}\,, \tag{A.6}$$

where θ is the scattering angle. Here we have made use of the fact that

$$2\sin^2\frac{\theta}{2} = 1 - \cos\theta\,, \tag{A.7}$$

and we have also employed

$$E^2 = m^2 + \mathbf{p}^2\,. \tag{A.8}$$

The momentum tranfer $\mathbf{q}^2$ can also be expressed in terms of a sinus function, yielding

$$|\mathbf{q}|^4 = 16\beta^2 E^2 \mathbf{p}^2 \sin^4\frac{\theta}{2}\,. \tag{A.9}$$

So all in all we get for the unpolarized elastic scattering cross section

$$\begin{aligned}\frac{d\sigma}{d\Omega} &= \frac{4Z^2\alpha^2}{16\beta^2E^2\mathbf{p}^2\sin^4\frac{\theta}{2}}\frac{1}{2}[2E^2 - m^2 - 2E^2\beta^2\sin^2\frac{\theta}{2} + m^2] \\ &= \frac{Z^2\alpha^2}{4\mathbf{p}^2\beta^2\sin^4\frac{\theta}{2}}[1 - \beta^2\sin^2\frac{\theta}{2}]\,,\end{aligned} \tag{A.10}$$

which is just the Mott cross section.

As an *excursus* let us briefly derive from that the classical cross section known as the Rutherford formula. To that end we just let $\beta \to 0$, obtaining

$$\left(\frac{d\sigma}{d\Omega}\right)_{\text{cl}} = \frac{Z^2\alpha^2}{4\mathbf{p}^2\sin^4\frac{\theta}{2}}\frac{1}{\beta} = \frac{Z^2\alpha^2}{4\mathbf{p}^2\sin^4\frac{\theta}{2}}\frac{E^2}{\mathbf{p}^2}\,, \tag{A.11}$$

which, recalling Eq. (A.8) in the limit of small momenta, yields the Rutherford formula,

$$\left(\frac{d\sigma}{d\Omega}\right)_{\text{cl}} = \frac{Z^2\alpha^2}{4\mathbf{p}^2\sin^4\frac{\theta}{2}}\frac{m^2}{\mathbf{p}^2}\,. \tag{A.12}$$

Let us now return to the higher order contributions.

The other amplitude products in Eq. A.3 are more elaborate.

A.2.1 Amplitude product $\mathcal{M}^{\star}_{\mathrm{Born}}\mathcal{M}_{\mathrm{vp}}$

Let us first calculate $\mathcal{M}_{\mathrm{vp}}$, which is divergent. We get

$$\begin{aligned}\mathcal{M}_{\mathrm{vp}} &= i^6 Z e^4 \bar{u}(p',s')\gamma_\alpha u(p,s)\frac{1}{\mathbf{q}^2} \\ &\quad \times \mathrm{tr}\left[\int \frac{d^4k}{(2\pi)^4}\frac{(\not{q}+\not{k}+m)_{ab}}{(q+k)^2-m^2}\gamma^0_{bc}\frac{(\not{k}'+m)_{cd}}{k^2-m^2}\gamma^\alpha_{da}\frac{1}{|\mathbf{q}|^2}\right] . \end{aligned} \tag{A.13}$$

From the matrix indices a, b, c, d we can see that the loop ("vacuum polarization") has produced a trace. We can write in a more compact way

$$\mathcal{M}_{\mathrm{vp}} = \frac{-Ze^4}{|\mathbf{q}|^2}\bar{u}(p',s')\gamma_\alpha u(p,s)\frac{1}{\mathbf{q}^2}\int\frac{d^4k}{(2\pi)^4}\frac{\mathrm{tr}[\gamma^\alpha(\not{q}+\not{k}+m)\gamma^0(\not{k}+m)]}{[(q+k)^2-m^2][k^2-m^2]} . \tag{A.14}$$

The evaluation of the trace is straight-forward. We obtain

$$\begin{aligned}&\frac{-Ze^4}{|\mathbf{q}|^2}\bar{u}(p',s')\gamma_\alpha u(p,s)\frac{4}{\mathbf{q}^2} \\ &\int\frac{d^4k}{(2\pi)^4}\frac{k^\alpha(2\omega+q^0)+q^\alpha\omega-g^{\alpha 0}[k\cdot(k+q)-m^2]}{[(q+k)^2-m^2][k^2-m^2]} ,\end{aligned} \tag{A.15}$$

which further simplifies when taking into account that $q^0 = 0$. Let us do the following regularization in a bit more general way so that we can recycle it in the future. The integral appearing in (A.15),

$$\int\frac{d^4k}{(2\pi)^4}\frac{k^\alpha(2\omega+q^0)+q^\alpha\omega-g^{\alpha 0}[k\cdot(k+q)-m^2]}{[(q+k)^2-m^2][k^2-m^2]} , \tag{A.16}$$

can also be written in fully covariant form,

$$\int\frac{d^4k}{(2\pi)^4}\frac{k^\alpha(k^\beta+q^\beta)+k^\beta(k^\alpha+q^\alpha)-g^{\alpha\beta}(k^2+k\cdot q-m^2)}{[(q+k)^2-m^2][k^2-m^2]} \equiv \Pi^{\alpha\beta}(q) . \tag{A.17}$$

The tensor (A.17) can be decomposed into a tensor contribution and a scalar part,

$$\Pi^{\alpha\beta}(q) = \left(\frac{q^\alpha q^\beta}{q^2}-g^{\alpha\beta}\right)\Pi(q^2) . \tag{A.18}$$

The trace of (A.18) is

$$\Pi^\alpha_\alpha(q) = -3\Pi(q^2) . \tag{A.19}$$

Let us now calculate

$$\begin{aligned}\Pi^\alpha_\alpha(q) &= \int \frac{d^4k}{(2\pi)^4}\frac{2k^2+2k\cdot q-4k^2-4k\cdot q+4m^2}{[(q+k)^2-m^2][k^2-m^2]}\\ &= -2\int \frac{d^4k}{(2\pi)^4}\frac{k^2+k\cdot q-2m^2}{[(q+k)^2-m^2][k^2-m^2]}\,. \end{aligned} \tag{A.20}$$

This integral is of course highly divergent, so we have to regularize it. The easiest way to do this would be dimensional regularization, but we have regularized the bremsstrahlung amplitudes with Pauli-Villars technology, so we have to do the same for this amplitude. It turns out that we even need two fermion counter terms,

$$\begin{aligned}&\frac{1}{(k+q)^2-m^2+i\epsilon}\frac{1}{k^2-m^2+i\epsilon}\to\frac{1}{(k+q)^2-m^2+i\epsilon}\times\\ &\left(\frac{1}{k^2-m^2+i\epsilon}+\frac{\alpha_1}{k^2-\Lambda_1^2+i\epsilon}+\frac{\alpha_2}{k^2-\Lambda_2^2+i\epsilon}\right),\end{aligned} \tag{A.21}$$

where

$$\alpha_1\equiv\frac{m^2-\Lambda_2^2}{\Lambda_2^2-\Lambda_1^2}\,,\qquad \alpha_1\equiv\frac{\Lambda_1^2-m^2}{\Lambda_2^2-\Lambda_1^2}\,. \tag{A.22}$$

Thus the modified propagator product (A.21) becomes

$$\begin{aligned}&\frac{(\Lambda_1^2-m^2)(\Lambda_2^2-m^2)}{(k^2-m^2+i\epsilon)(k^2-\Lambda_1^2+i\epsilon)(k^2-\Lambda_2^2+i\epsilon)}\frac{1}{(k+q)^2-m^2+i\epsilon}\\ &\to\frac{\Lambda^4}{(k^2-m^2+i\epsilon)(k^2-\Lambda^2+i\epsilon)^2}\frac{1}{(k+q)^2-m^2+i\epsilon}\,,\end{aligned} \tag{A.23}$$

in the limit as $\Lambda_1,\Lambda_2\to\Lambda$, where Λ is a large cut-off with $\Lambda\gg 1$. So for (A.19) we obtain

$$\begin{aligned}\Pi^\alpha_\alpha(q) &= -2\int\frac{d^4k}{(2\pi)^4}\frac{k^2+k\cdot q-2m^2}{(k+q)^2-m^2+i\epsilon}\frac{\Lambda^4}{(k^2-m^2+i\epsilon)(k^2-\Lambda^2+i\epsilon)^2}\\ &= -2\int\frac{d^4k}{(2\pi)^2}\int_0^1 dxdydzz\delta(x+y+z-1)\frac{\Gamma(4)}{\Gamma^2(1)\Gamma(2)}\\ &\quad\times\frac{\Lambda^4(k^2+k\cdot q-2m^2)}{[x(k+q)^2-xm^2+xi\epsilon+yk^2-ym^2+yi\epsilon+zk^2-z\Lambda^2+zi\epsilon]^4}\\ &= -12\int\frac{d^4k}{(2\pi)^2}\int_0^1 dxdydz\delta(x+y+z-1)\frac{z\Lambda^4(k^2+k\cdot q-2m^2)}{D^4}\,,\end{aligned} \tag{A.24}$$

where

$$\begin{aligned}D &\equiv x(k+q)^2-xm^2+yk^2-ym^2-z\Lambda^2+i\epsilon\\ &= k^2+xq^2+2xk\cdot q-(x+y)m^2-z\Lambda^2+i\epsilon\\ &= l^2-x(x-1)q^2-(x+y)m^2-z\Lambda^2+i\epsilon\,.\end{aligned} \tag{A.25}$$

Here we have introduced the shifted momentum

$$l \equiv k + xq\,. \tag{A.26}$$

The numerator of (A.24) also has to be changed into a function of l, and we obtain

$$z\Lambda^4(k^2 + k\cdot q - 2m^2) = z\Lambda^4[l^2 - 2xl\cdot q + x(x-1)q^2 + l\cdot q - 2m^2]\,, \tag{A.27}$$

but the two terms linear in l will vanish under an integration over l later. Inserting the numerator into (A.24) and switching the momentum integral to d^4l, we obtain

$$\begin{aligned}\Pi^\alpha_\alpha(q) &= -12\int\frac{d^4l}{(2\pi)^4}\int_0^1 dxdydz\delta(x+y+z-1)z\Lambda^4 \\ &\quad\times\frac{l^2 + x(x-1)q^2 - 2m^2}{[l^2-\Delta+i\epsilon]^4}\,,\end{aligned} \tag{A.28}$$

where

$$\Delta \equiv -x(1-x)q^2 + (x+y)m^2 + z\Lambda^2\,. \tag{A.29}$$

The integral over d^4l can be done by means of a Wick rotation. A detailed derivation of the rotation can be found in Ref. [42]. It leads to

$$\int\frac{d^4l}{(2\pi)^4}\frac{1}{[l^2-\Delta+i\epsilon]^4} = \frac{i}{(4\pi)^2}\frac{1}{3\cdot 2}\frac{1}{\Delta^2}\,, \tag{A.30}$$

and in the case where the numerator is proportional to l^2 we obtain

$$\int\frac{d^4l}{(2\pi)^4}\frac{l^2}{[l^2-\Delta+i\epsilon]^4} = \frac{-i}{(4\pi)^2}\frac{2}{3\cdot 2\cdot 1}\frac{1}{\Delta}\,. \tag{A.31}$$

So we obtain for the trace (A.20)

$$\begin{aligned}\Pi^\alpha_\alpha(q) &= -\frac{12}{6}\frac{i}{(4\pi)^2}\int_0^1 dxdydz\delta(x+y+z-1)z\Lambda^4 \\ &\quad\times\left[\frac{2}{\Delta} - \frac{x(x-1)q^2-2m^2}{\Delta^2}\right] = -3\Pi(q^2)\,.\end{aligned} \tag{A.32}$$

In our case where, the Lorentz index $\beta = 0$, we obtain for the expression (A.18)

$$\begin{aligned}\Pi^{\alpha 0}(q) &= \frac{i}{24\pi^2}\int_0^1 dxdydz\delta(x+y+z-1)z\Lambda^4 \\ &\quad\times\left[\frac{2}{\Delta} - \frac{x(x-1)q^2-2m^2}{\Delta^2}\right]\left(\frac{q^\alpha q^0}{q^2} - g^{\alpha 0}\right)\,.\end{aligned} \tag{A.33}$$

But as mentioned in the introduction we are dealing with elastic scattering only, where $q^0 = 0$, because the electron energy is conserved. But let us keep

the vector contribution in the round brackets anyway, so that we can simply reconstruct the covariant form of $\Pi^{\alpha\beta}(q)$ in case we should need it later.

Before we now put together the whole amplitude product we have to render (A.33) finite, *i.e.* Λ has to disappear. To that end we have to perform at least two of the integrations over the Feynman parameters. Let us start with the integration over y and the Dirac delta function. Δ and can be written in such a way that it does not depend on y any more, so that the integration becomes rather trivial. Using

$$\begin{aligned}\Delta &\equiv -x(x-1)q^2-(x+y)m^2-z\Lambda^2 \\ &= -x(x-1)q^2+(z-1)m^2-z\Lambda^2\,, \end{aligned} \tag{A.34}$$

we obtain

$$\begin{aligned}\Pi^{\alpha 0}(q) &= \frac{i}{24\pi^2}\int_0^1 dxdzz\Lambda^4[\theta(x+z)-\theta(x+z-1)] \\ &\quad\times\left\{\frac{x(x-1)q^2-2m^2}{[-x(x-1)q^2+(z-1)m^2-z\Lambda^2]^2}\right. \\ &\quad\left.-\frac{2}{-x(x-1)q^2+(z-1)m^2-z\Lambda^2}\right\}\left(\frac{q^\alpha q^0}{q^2}-g^{\alpha 0}\right) \\ &= \frac{i}{24\pi^2}\int_0^1 dx\int_0^{1-x} dzz\Lambda^4 \\ &\quad\times\left\{\frac{x(x-1)q^2-2m^2}{[-x(x-1)q^2+(z-1)m^2-z\Lambda^2]^2}\right. \\ &\quad\left.-\frac{2}{-x(x-1)q^2+(z-1)m^2-z\Lambda^2}\right\}\left(\frac{q^\alpha q^0}{q^2}-g^{\alpha 0}\right)\,, \end{aligned} \tag{A.35}$$

because the two Heaviside functions limit the Feynman parameter space to the bottom left triangle in the xz plane. Now we have to carry out the z-integrations. The first one yields a denominator which is proportional to Λ^4. Keeping in mind the factor Λ^4 in the numerator, we see that all terms of order less than Λ^4 in the numerator can be neglected in the limit as $\Lambda\to\infty$. Thus we obtain

$$\begin{aligned}\Pi^{\alpha 0}(q) &= \frac{i}{24\pi^2}\int_0^1 dx\frac{\Lambda^4}{(m^2-\Lambda^2)^2}\left(\frac{q^\alpha q^0}{q^2}-g^{\alpha 0}\right) \\ &\quad\times\left[\frac{[\mathbf{A}]}{-x(x-1)q^2-\Lambda^2-x(m^2-\Lambda^2)}+[\mathbf{B}]\right]\,, \end{aligned} \tag{A.36}$$

where

$$\begin{aligned}\mathbf{A} &\equiv \Lambda^2[x(x-1)q^2-2m^2]\left\{\log[-x(x-1)q^2-\Lambda^2-(m^2-\Lambda^2)x][x-1]\right. \\ &\quad\left.-[x-1]-\log[-x(x-1)q^2-m^2][x-1]\right\}\,, \end{aligned} \tag{A.37}$$

and

$$\begin{aligned}\mathbf{B} \;\equiv\; & 2m^2(x-1) - 2\Lambda^2(x-1) + 2[-x(x-1)q^2 - m^2] \\ & \times \left\{\log[-x(x-1)q^2 + x\Lambda^2 - xm^2 - \Lambda^2] - \log[-x(x-1)q^2 - m^2]\right\} .\end{aligned} \tag{A.38}$$

As mentioned above expression **A** has been simplified by neglecting terms of the order less than Λ^2. Now we evaluate the limit $\Lambda \to \infty$, yielding

$$\lim_{\Lambda\to\infty} \frac{\Lambda^4}{(m^2-\Lambda^2)^2} = 1\,, \tag{A.39}$$

and

$$\lim_{\Lambda\to\infty} \frac{\Lambda^2}{-x(1-x)q^2 - \Lambda^2 - x(m^2-\Lambda^2)} = \frac{1}{x-1}\,. \tag{A.40}$$

So $\Pi^{\alpha 0}(q^2)$ reduces to

$$\begin{aligned}\Pi^{\alpha 0}(q) \;=\; & \frac{i}{24\pi^2}\int_0^1 dx \left(\frac{q^\alpha q^0}{q^2} - g^{\alpha 0}\right) \\ & \times\Bigg\{ \log\left[\frac{-x(x-1)q^2 - \Lambda^2 - x(m^2-\Lambda^2)}{-x(x-1)q^2 - m^2}\right][-x(x-1)q^2 - 4m^2] \\ & - x(x-1)q^2 + 2m^2 + 2(m^2-\Lambda^2)(x-1)\Bigg\}.\end{aligned} \tag{A.41}$$

Constant terms or terms proportional to q^2 must be adjusted in such a way that gauge invariance is preserved. They correspond to local terms in position space for which perturbative QED does not hold any more. The logarithm can be simplified as follows,

$$\begin{aligned}\log\left[\frac{-x(x-1)q^2 - \Lambda^2 - x(m^2-\Lambda^2)}{-x(x-1)q^2 - m^2}\right] \;=\; & \log\Lambda^2 \\ & + \log\left[\frac{x-1}{-x(x-1)q^2 - m^2}\right],\end{aligned} \tag{A.42}$$

in the limit as $\Lambda \to \infty$. The first logarithm is just a trivial constant and can be dropped. The numerator in the second logarithm is also trivial, and in order to keep the units straight we just replace it by $(-m^2)$, finally obtaining

$$\Pi^{\alpha 0}(q) \;=\; \frac{i}{24\pi^2}\int_0^1 dx \log\left[\frac{m^2}{x(x-1)q^2 + m^2}\right] x(1-x)q^2 \left(\frac{q^\alpha q^0}{q^2} - g^{\alpha 0}\right). \tag{A.43}$$

The factor q^2 will disappear in a moment when we insert $\Pi^{\alpha 0}(q^2)$ into the vacuum polarization cross section. In order to get the physical result for elastic scattering

now let us finally set $q^0 = 0$ which simplifies the cross section considerably. Let us first write down the amplitude product

$$\begin{aligned} 2\mathcal{M}_{\rm vp}\mathcal{M}^{\star}_{\rm Born} &= 2\Bigg[\frac{Ze^4}{|\mathbf{q}|^2}\bar{u}(p',s')\gamma_\alpha u(p,s)\frac{4}{q^2}\frac{i}{24\pi^2}\int_0^1 dx \\ &\quad\times\log\left[\frac{m^2}{x(x-1)q^2+m^2}\right]x(1-x)q^2 g^{\alpha 0}\Bigg] \\ &\quad\times\left[\frac{-iZe^2}{|\mathbf{q}|^2}\bar{u}(p',s')\gamma^0 u(p,s)\right]^{\star}. \end{aligned} \tag{A.44}$$

When summing over initial and final spin states, this expression reduces to

$$\begin{aligned} \frac{1}{2}\sum_{s,s'} 2\mathcal{M}^{\star}_{\rm Born}\mathcal{M}_{\rm vp} &= \frac{Z^2e^4}{|\mathbf{q}|^4}{\rm tr}[(\not{p}'+m)\gamma^0(\not{p}'+m)\gamma^0]\frac{e^2}{6\pi^2} \\ &\quad\times\int_0^1 dx x(1-x)\log\left[\frac{m^2}{x(x-1)q^2+m^2}\right]. \end{aligned} \tag{A.45}$$

The first factor together with the trace is just

$$\frac{1}{2}\sum_{s,s'}|\mathcal{M}_{\rm Born}|^2, \tag{A.46}$$

so we can re-write down the scattering cross section as

$$\begin{aligned} \left(\frac{d\sigma}{d\Omega_{\rm e}}\right)_{\rm Born\times vp} &= -\left(\frac{d\sigma}{d\Omega_{\rm e}}\right)_{\rm Born}\frac{2\alpha}{3\pi}\int_0^1 dx x(1-x) \\ &\quad\times\log\left[\frac{m^2}{m^2-x(1-x)q^2}\right] \\ &= -\left(\frac{d\sigma}{d\Omega_{\rm e}}\right)_{\rm Born}\frac{2\alpha}{3\pi}\int_0^1 dx x(1-x) \\ &\quad\times\log\left[\frac{1}{1-x(1-x)\frac{q^2}{m^2}}\right]. \end{aligned} \tag{A.47}$$

This integral can be solved with the help of MAPLE if the argument of the logarithm is written in factorized form. Only then one can consider the UR limit in which

$$-\frac{q^2}{m^2} \gg 1, \tag{A.48}$$

which is well satisfied in the GeV region. So from Eq. (A.47) we get

$$\begin{aligned} \left(\frac{d\sigma}{d\Omega_{\rm e}}\right)_{\rm Born\times vp} &= -\left(\frac{d\sigma}{d\Omega_{\rm e}}\right)\frac{2\alpha}{3\pi}\Bigg[\left(-\frac{1}{3}\frac{m^2}{q^2}-\frac{1}{6}\right)\sqrt{1-\frac{4m^2}{q^2}} \\ &\quad\times\log\left(\frac{1+\sqrt{1-\frac{4m^2}{q^2}}}{-1+\sqrt{1-\frac{4m^2}{q^2}}}\right)+\frac{5}{18}+\frac{2}{3}\frac{m^2}{q^2}\Bigg]. \end{aligned} \tag{A.49}$$

This is the exact result for arbitrary q^2. In the UR limit the square roots can be expanded, leading to

$$\left(\frac{d\sigma}{d\Omega_\mathrm{e}}\right)^\mathrm{ur}_{\mathrm{Born}\times\mathrm{vp}} \sim -\left(\frac{d\sigma}{d\Omega_\mathrm{e}}\right)_\mathrm{Born} \frac{2\alpha}{3\pi}\left[-\frac{1}{6}\log\left(-\frac{m^2}{q^2}\right)+\frac{5}{18}\right]. \tag{A.50}$$

In the Uehling case (which is the non-relativistic limit), where

$$-\frac{q^2}{m^2} \ll 1\,, \tag{A.51}$$

the cross section (A.49) vanishes, because

$$\lim_{-q^2\to 0} \left\{-\frac{1}{6}\left(1+\frac{2m^2}{q^2}\right)\sqrt{1-\frac{4m^2}{q^2}}\log\left(\frac{1+\sqrt{1-\frac{4m^2}{q^2}}}{-1+\sqrt{1-\frac{4m^2}{q^2}}}\right) + \frac{2}{3}\frac{m^2}{q^2}\right\} = -\frac{5}{18}\,. \tag{A.52}$$

A.2.2 Amplitude product $\mathcal{M}^\star_\mathrm{Born}\mathcal{M}_\mathrm{vc}$

Let us calculate the first half of expression (A.3). Before we consider the whole product let us evaluate $\mathcal{M}_\mathrm{vc}$ alone. This is the amplitude which will contain ultraviolet and infrared divergences and again the consistency of the theory demands that we regularize every integral (and the S-matrix) before we come to physical quantities like cross sections which should be definite from the beginning.

$$\begin{aligned}\mathcal{M}_\mathrm{vc} &= (-)^4(i)^6\frac{Ze^4}{|\mathbf{q}|^2}\int\frac{d^4k}{(2\pi)^4} \\ &\quad\times\bar{u}(p',s')\frac{\gamma_\rho(\not{k}'+m)\gamma^0(\not{k}+m)\gamma^\rho}{[(k-p)^2+i\epsilon][k'^2-m^2+i\epsilon][k^2-m^2+i\epsilon]}u(p,s)\,,\end{aligned} \tag{A.53}$$

where the momenta k and k' where the incident and the scattered electron's four-momenta, respectively. Keeping in mind that the slashed momenta can act on the spinors according to the Dirac equation (see [42], page 191, bottom), we can rearrange the numerator in Eq. (A.53). Using a slightly different notation we obtain

$$\frac{-Ze^4}{|\mathbf{q}|^2}\int\frac{d^4k}{(2\pi)^4}\frac{\bar{u}(p',s')[\not{k}\gamma^0\not{k}'+m^2\gamma^0-2m(k+k')^0]u(p,s)}{[(k-p)^2+i\epsilon][k'^2-m^2+i\epsilon][k^2-m^2+i\epsilon]}\,. \tag{A.54}$$

Now we introduce Feynman parameters and then switch to the shifted momentum l again, yielding

$$\begin{aligned}&\frac{-2Ze^4}{|\mathbf{q}|^2}\int\frac{d^4l}{(2\pi)^4}\int_0^1 dxdydz\delta(x+y+z-1)\bar{u}(p',s')\\&\times\frac{-\frac{1}{2}\gamma^0 l^2+(-y\not{q}+z\not{p})\gamma^0((1-y)\not{q}+z\not{p})+m^2\gamma^0-2m((1-2y)q^0+2zp^0)}{[l^2-\Delta+i\epsilon]^3}\\&\times u(p,s)\,,\end{aligned}\tag{A.55}$$

where $l\equiv k+yq-zp$ and $\Delta\equiv -xyq^2+(1-z)^2m^2$. The factor of 2 comes from the Feynman parameters. One can now give the numerator a shape which is more easy to handle. This is proved in [42]. The calculation was done partially with help from MAPLE. We obtain

$$\begin{aligned}&\frac{-2Ze^4}{|\mathbf{q}|^2}\int\frac{d^4l}{(2\pi)^4}\int_0^1 dxdydz\delta(x+y+z-1)\bar{u}(p',s')\\&\times\left\{\frac{\gamma^0[-\frac{1}{2}l^2+(1-x)(1-y)q^2+(1-2z-z^2)m^2]}{[l^2-\Delta+i\epsilon]^3}\right.\\&\left.+\frac{(p'^0+p^0)mz(z-1)+q^0m(z-2)(x-y)}{[l^2-\Delta+i\epsilon]^3}\right\}u(p,s)\,.\end{aligned}\tag{A.56}$$

The last term in the numerator (proportional to q^0) vanishes for symmetry reasons under integration over the Feynman parameters. Now, using the Gordon identity we can write (A.56) as

$$\begin{aligned}&\frac{-2Ze^4}{|\mathbf{q}|^2}\int\frac{d^4l}{(2\pi)^4}\int_0^1 dxdydz\delta(x+y+z-1)\bar{u}(p',s')\\&\times\frac{\gamma^0[-\frac{1}{2}l^2+(1-x)(1-y)q^2+(1-2z-z^2)m^2]+\frac{i\sigma^{0\nu}q_\nu}{2m}2m^2z(z-1)}{[l^2-\Delta+i\epsilon]^3}\\&\times u(p,s)\,,\end{aligned}\tag{A.57}$$

which might be of advantage when introducing the so called form factors for the electron. Again we perform a Wick rotation, employing the following two integration equations,

$$\int\frac{d^4l}{(2\pi)^4}\frac{1}{[l^2-\Delta]^m}=\frac{i(-)^m}{(4\pi)^2}\frac{1}{(m-1)(m-2)}\frac{1}{\Delta}\,,\tag{A.58}$$

and for the numerator proportional to l^2,

$$\int\frac{d^4l}{(2\pi)^4}\frac{l^2}{[l^2-\Delta]^m}=\frac{i(-)^{m-1}}{(4\pi)^2}\frac{2}{(m-1)(m-2)(m-3)}\frac{1}{\Delta^{m-3}}\,.\tag{A.59}$$

Unfortunately the latter formula is divergent in the interesting case $m = 3$. Therefore we regularize the integral using Pauli-Villars regulations, *i.e.* we replace the photon propagator in (A.56) by

$$\frac{1}{(k-p)^2+i\epsilon} \to \frac{1}{(k-p)^2+i\epsilon} - \frac{1}{(k-p)^2-\Lambda+i\epsilon}\,, \tag{A.60}$$

where Λ serves as a large "photon mass". The regularized integral is straightforward to solve. We introduce the denominator Δ_Λ, accounting for the massive photon [42],

$$\Delta_\Lambda \equiv -xyq^2 + (1-z)^2m^2 + z\Lambda^2\,, \tag{A.61}$$

and we obtain

$$\int \frac{d^4l}{(2\pi)^4}\left\{\frac{l^2}{[l^2-\Delta]^3} - \frac{l^2}{[l^2-\Delta_\Lambda]^3}\right\} = \frac{i}{(4\pi)^2}\log\left(\frac{\Delta_\Lambda}{\Delta}\right)\,, \tag{A.62}$$

where $\Delta_\Lambda \equiv -xyq^2 + (1-z)^2m^2 + z\Lambda$. So we get for the vertex correction amplitude

$$\begin{aligned}
\mathcal{M}_{\rm vc} &= \frac{-2Ze^4}{|\mathbf{q}|^2}\int_0^1 dxdydz\delta(x+y+z-1)\bar{u}(p',s') \\
&\quad\times\left\{\frac{-i\gamma^0}{(4\pi)^2}\log\left(\frac{\Delta_\Lambda}{\Delta}\right)\right. \\
&\quad+\frac{-i\gamma^0}{(4\pi)^2\Delta}\Big[(1-x)(1-y)q^2+(1-4z+z^2)m^2 \\
&\quad\left.+\frac{i\sigma^{0\nu}q_\nu}{2m}2m^2z(1-z)\Big]\right\}u(p,s)\,.
\end{aligned} \tag{A.63}$$

The overall minus sign cancels the two minus signs in the second line of Eq. (A.63). Traditionally one calls the coefficient of γ^0,

$$\begin{aligned}
F_1(q^2) &\equiv \frac{\alpha}{2\pi}\int_0^1 dxdydz\delta(x+y+z-1) \\
&\quad\times\left[\log\frac{\Delta_\Lambda}{\Delta}+\frac{(1-x)(1-y)q^2+(1-4z+z^2)m^2}{\Delta}\right]\,,
\end{aligned} \tag{A.64}$$

the first form factor and the other one,

$$F_2(q^2) \equiv \frac{\alpha}{2\pi}\int_0^1 dxdydz\delta(x+y+z-1)\frac{2m^2z(1-z)}{\Delta}\,. \tag{A.65}$$

So the vertex correction amplitude can be written as

$$\mathcal{M}_{\rm vc} = \frac{iZe^2}{|\mathbf{q}|^2}\bar{u}(p',s')\left[F_1(q^2)\gamma^0 + F_2(q^2)\frac{i\sigma^{0\nu}q_\nu}{2m}\right]u(p,s)\,. \tag{A.66}$$

The first form factor $F_1(q^2)$ is divergent both in the ultraviolet and in the infrared region. So, as we want to render this amplitude finite, we remove the dependence on Λ, by dropping the term $\log z\Lambda^2$ from the right hand side of

$$\log\left(\frac{\Delta_\Lambda}{\Delta}\right) \sim \log\left(\frac{z\Lambda^2}{\Delta}\right) \to \log\left(\frac{1}{\Delta}\right) . \tag{A.67}$$

This procedure can also be done a bit more formally, by replacing

$$F_1(q^2) \to F_1(q^2) - F_1(0) . \tag{A.68}$$

Thus we obtain for the first form factor

$$\begin{aligned} F_1(q^2) &= \frac{\alpha}{2\pi}\int_0^1 dxdydz\delta(x+y+z-1) \\ &\quad \times\left\{\log\left[\frac{m^2(1-z)^2}{m^2(1-z)^2 - xyq^2}\right]\right. \\ &\quad \left. + \frac{(1-x)(1-y)q^2 + (1-4z+z^2)m^2}{\Delta} - \frac{(1-4z+z^2)m^2}{\Delta(q^2=0)}\right\} . \end{aligned} \tag{A.69}$$

Unfortunately the two last terms from the square brackets are still infrared divergent. We can fix this problem by introducing a small photon mass μ in the photon propagator in Eq. (A.54). This part of the denominator was multiplied by x, so in Eq. (A.69) we have to modify the denominator according to

$$-xyq^2 + (1-z)^2m^2 + x\mu^2 . \tag{A.70}$$

Form factor $F_1(q^2)$ cannot be represented in a very compact manner when performing the integrations over the Feynman parameters. Let us split it into three parts,

$$F_1(q^2) = \frac{\alpha}{2\pi}\left[F_1^a(q^2) + F_1^b(q^2,\mu^2) + F_1^c(\mu^2)\right] , \tag{A.71}$$

such that

$$\begin{aligned} F_1^a(q^2) &= \int_0^1 dxdydz\delta(x+y+z-1)\log\left[\frac{(1-z)^2m^2}{-xyq^2+(1-z)^2m^2} ,\right] \\ F_1^b(q^2,\mu^2) &= \int_0^1 dxdydz\delta(x+y+z-1) \\ &\quad \times\frac{(1-x)(1-y)q^2 + (1-4z+z^2)m^2}{-xyq^2+(1-z)^2m^2+x\mu^2} , \\ F_1^c(\mu^2) &= -\int_0^1 dxdydz\delta(x+y+z-1)\frac{(1-4z+z^2)m^2}{(1-z)^2m^2+x\mu^2} . \end{aligned} \tag{A.72}$$

Let us first calculate the non-trivial (non-diverging) contributions to $F_1(q^2)$,

$$\begin{aligned} F_1^a(q^2) &= \int_0^1 dxdydz\delta(x+y+z-1)\log\left[\frac{m^2(1-z)^2}{m^2(1-z)^2-xyq^2}\right] \\ &= \int_0^1 dxdydz\delta(x+y+z-1)\log\left[\frac{m^2(1-z)^2}{m^2(1-z)^2-x(1-z-x)q^2}\right], \end{aligned} \tag{A.73}$$

so now we can perform the trivial integration over y, yielding

$$\begin{aligned} F_1^a(q^2) &= \int_0^1 dx\int_0^1 dz\log\left[\frac{m^2(1-z)^2}{m^2(1-z)^2-x(1-x-z)q^2}\right] \\ &\quad\times[\theta(x+z)-\theta(x+y-1)] \\ &= \int_0^1 dz\int_0^{1-z} dx\cdot 1\cdot\log\left[\frac{m^2(1-z)^2}{m^2(1-z)^2-x(1-x-z)q^2}\right]. \end{aligned} \tag{A.74}$$

The factor "1" was introduced in order to highlight our choice for the integration by parts which gives

$$\begin{aligned} F_1^a(q^2) &= \int_0^1 dz\int_0^{1-z} dxx\frac{\partial}{\partial x}\log\left[\frac{m^2(1-z)^2}{m^2(1-z)^2-x(1-x-z)q^2}\right], \\ &= \int_0^1 dz\int_0^{1-z} dx\frac{x(-1+2x+z)q^2}{m^2(1-z)^2-x(1-x-z)q^2}, \end{aligned} \tag{A.75}$$

where we have omitted the surface term which vanishes trivially. In order to perform the integration over x with MAPLE, it is necessary to factorize the polynomial in x in the denominator of the second line of Eq. (A.75) in the following way,

$$q^2(x-x_1)(x-x_2), \tag{A.76}$$

where

$$x_{1,2}\equiv\frac{(z-1)}{2}\frac{-q^2\pm\sqrt{q^4-4q^2m^2}}{q^2}. \tag{A.77}$$

Now MAPLE can do the integral over x, yielding

$$F_1^a(q^2) = \int_0^1 dz\left\{(1-z)\sqrt{1-\frac{4m^2}{q^2}}\log\left[\frac{-1+\sqrt{1-\frac{4m^2}{q^2}}}{1+\sqrt{1-\frac{4m^2}{q^2}}}\right]-2(z-1)\right\}. \tag{A.78}$$

The last Feynman parameter integral is trivial and we get

$$F_1^a(q^2) = \frac{1}{2}\sqrt{1-\frac{4m^2}{q^2}}\log\left[\frac{-1+\sqrt{1-\frac{4m^2}{q^2}}}{1+\sqrt{1-\frac{4m^2}{q^2}}}\right]+1. \tag{A.79}$$

Consider now the UR limit where

$$-\frac{q^2}{m^2} \gg 1\,. \tag{A.80}$$

In his limit the square roots can be expanded and we obtain

$$F_1^{\mathrm{ur}\,a}(q^2) \;\sim\; \frac{1}{2}\log\left(-\frac{m^2}{q^2}\right) + 1\,. \tag{A.81}$$

Now we calculate the infrared divergent terms, F_1^b and F_1^c. They diverge in the limit as $\mu \to 0$. We cannot follow the calculations carried out in [42], because there only terms are taken into account which diverge in this limit, so our final result will differ from the expression Ref. [42] achieves.

Consider the form factor contribution $F_1^b(q^2,\mu^2)$. Replacing the Feynman parameter x according to $x+y+z=1$, we can trivially perform the x-integral, obtaining

$$\begin{aligned}
F_1^b(q^2,\mu^2) &= \int_0^1 dz \int_0^{z-1} dy \frac{m^2(1-4z+z^2)+q^2(y+z)(1-y)}{m^2(1-z)^2 - q^2 y(1-y-z) + \mu^2(1-y-z)} \\
&= \int_0^1 dz \Bigg\{ -\frac{1}{2}\frac{N}{q^2\sqrt{M}} \arctan\left[\frac{q^2(z-1)-\mu^2}{\sqrt{M}}\right] \\
&\quad -\frac{1}{2}\frac{N}{q^2\sqrt{M}} \arctan\left[\frac{q^2(z-1)+\mu^2}{\sqrt{M}}\right] \\
&\quad +\frac{1}{2}\frac{\mu^2}{q^2}\log\left[(z-1)-\frac{\mu^2}{m^2}\right] + (z-1)\Bigg\}\,,
\end{aligned} \tag{A.82}$$

where

$$\begin{aligned}
M &\equiv (-1+2z-z^2)q^4 + (-8m^2z + 4m^2z^2 - 2\mu^2 z + 4m^2 + 2\mu^2)q^2 - \mu^4 \\
&= -Q^2(Q^2+4m^2)(1-z)^2 - 2\mu^2(1-z)Q^2 - \mu^4\,, \\
N &\equiv 4q^4 z + (8m^2z^2 - 2\mu^2 z + 2\mu^2 + 8m^2 - 24m^2 z)q^2 - 2\mu^4\,,
\end{aligned} \tag{A.83}$$

respectively. The terms containing the arctan in Eq. (A.82) can be changed into logarithm functions which follows from the trivial identity

$$\frac{1}{a}\arctan\frac{x}{a} = \frac{1}{2ai}\log\left(\frac{-x+ia}{x+ia}\right)\,, \tag{A.84}$$

yielding

$$
\begin{aligned}
F_1^b(q^2,\mu^2) \;=\; & \int_0^1 dz \Bigg(\frac{1}{4}\frac{iN}{q^2\sqrt{M}} \Bigg\{ -\log\left[\sqrt{M} + i(1-z)q^2 - i\mu^2\right] \\
& -\log\left[\sqrt{M} + i(1-z)q^2 + i\mu^2\right] \\
& +\log\left[\sqrt{M} - i(1-z)q^2 + i\mu^2\right] \\
& +\log\left[\sqrt{M} - i(1-z)q^2 - i\mu^2\right] \Bigg\} \\
& +\frac{1}{2}\frac{\mu^2}{q^2}\log\left[(z-1) - \frac{m^2}{q^2}\right] + [z-1] \Bigg) . \qquad \text{(A.85)}
\end{aligned}
$$

The four logarithms can be merged and seeing that M from Eq. (A.83) is actually negative, all imaginary contributions within the logarithm cancel for obvious reasons. Inserting $Q^2 \equiv -q^2$ we can write

$$
\begin{aligned}
F_1^b(Q^2,\mu^2) \;=\; & \int_0^1 dz \Bigg(\frac{1}{4}\frac{-iN}{Q^2\sqrt{M}} \\
& \times \log\left\{ \frac{[\sqrt{-M} + Q^2(1-z) + \mu^2][\sqrt{-M} + Q^2(1-z) - \mu^2]}{[\sqrt{-M} - Q^2(1-z) - \mu^2][\sqrt{-M} - Q^2(1-z) + \mu^2]} \right\} \\
& -\frac{1}{2}\frac{\mu^2}{Q^2}\log\left[\frac{m^2(z-1) - \mu^2}{m^2(z-1)}\right] + [z-1] \Bigg) \\
\;=\; & \int_0^1 dz \Bigg(\frac{1}{4}\frac{-N}{Q^2\sqrt{-M}} \\
& \times \log\left\{ \frac{-M + 2\sqrt{-M}Q^2(1-z) + Q^4(1-z)^2 - \mu^4}{-M - 2\sqrt{-M}Q^2(1-z) + Q^4(1-z)^2 - \mu^4} \right\} \\
& -\frac{1}{2}\frac{\mu^2}{Q^2}\log\left[1 - \frac{\mu^2/m^2}{z-1}\right] + [z-1] \Bigg) . \qquad \text{(A.86)}
\end{aligned}
$$

The integral over z is rather unpleasant, but it can be done using a small adjustment of μ. Let us rewrite M from Eq. (A.83) in the form

$$
-M = Q^2(Q^2+4m^2)\left(1 - z + \frac{\mu^2}{Q^2+4m^2}\right)^2 + \mathcal{O}(\mu^4) \equiv M' . \qquad \text{(A.87)}
$$

This only differs from the original definition of M by contributions of the order of μ^4. The advantage of giving M this shape rather than the one in Eq. (A.83)

is that we can take the square root in Eq. (A.86), yielding

$$\begin{aligned} F_1^b(Q^2,\mu^2) &= \int_0^1 dz \frac{-4Q^4 z + [8m^2(z^2-3z+1) - 2\mu^2(z-1)]Q^2 + 2\mu^4}{4Q^2\sqrt{Q^2(Q^2+4m^2)}\left(1-z+\frac{\mu^2}{Q^2+4m^2}\right)} \\ &\quad \times \log\left[\frac{M' + 2\sqrt{M'}Q^2(1-z) + Q^4(1-z)^2 - \mu^4}{M' - 2\sqrt{M'}Q^2(1-z) + Q^4(1-z)^2 - \mu^4}\right] \\ &\quad + \frac{\mu^2 - Q^2}{2Q^2} + \frac{\mu^2(m^2-Q^2)}{2Q^4}\log\left(\frac{m^2-Q^2}{m^2}\right). \end{aligned} \tag{A.88}$$

The last terms are integrated out already. Now we rewrite the integral in the form

$$\int_0^1 dz \frac{c_{12}(z-z_1)(z-z_2)}{c_3(z-z_3)} \log\left[\frac{c_{45}(z-z_4)(z-z_5)}{c_{67}(z-z_6)(z-z_7)}\right], \tag{A.89}$$

where the definitions of c_{12}, c_3, c_{45}, c_{67}, z_1, z_2, z_3, z_4, z_5, z_6, and z_7 are obvious.

In order to check the validity of the adjustment of M we also evaluated the integral (A.86) numerically which produced the same result.

We now evaluate the UR limit in which

$$\frac{Q^2}{m^2} \gg 1. \tag{A.90}$$

In this limit the expression in the first logarithm from Eq. (A.86) simplifies considerably and using the representation (A.89) we obtain

$$\begin{aligned} F_1^{\mathrm{ur}\,b}(Q^2,\mu^2) &= \frac{2}{\alpha}\int_0^1 dz \frac{z(z-\frac{\alpha}{2})}{z-1-\beta}\log\left[\frac{1}{\alpha^2}\frac{(z-1-\gamma)(z-1+\beta)}{(z-1-\beta)(z-1+\frac{\beta}{\alpha})}\right] \\ &\quad + \frac{\mu^2-Q^2}{2Q^2} + \frac{\mu^2(m^2-Q^2)}{2Q^4}\log\left(\frac{m^2-Q^2}{m^2}\right). \end{aligned} \tag{A.91}$$

The terms in the second line reduce to $-1/2$ in the UR limit. The dimensionless variables α, β, and γ are defined as

$$\alpha \equiv \frac{Q^2}{m^2} \quad \beta \equiv \frac{\mu^2}{Q^2} \quad \gamma \equiv \frac{\mu^2}{m^2}. \tag{A.92}$$

This integral is straight-forward when taking into account only the leading order terms. For the records we state here the result, keeping in mind that eventually

μ will go to zero. We obtain

$$\begin{aligned} F_1^{\mathrm{ur}\,b}(Q^2,\mu^2) &= -\frac{1}{2}\log^2(2) + \log(2)\log\left(\frac{Q^2}{\mu^2}\right) - \frac{1}{2}\log^2\left(\frac{Q^2}{\mu^2}\right) \\ &\quad - 2\log\left(\frac{Q^2}{\mu^2}\right)\log\left(\frac{Q^2}{m^2}\right) + \log\left(\frac{Q^2}{m^2}\right) + \frac{1}{2}\log^2\left(\frac{Q^2}{m^2}\right) \\ &\quad + \log\left(\frac{Q^2}{m^2}\right)\log\left(\frac{\mu^2}{m^2}\right) + \mathrm{dilog}\left(\frac{Q^2}{m^2}\right) \\ &\quad + \mathrm{dilog}\left(\frac{m^2}{\mu^2}\frac{Q^2}{m^2-Q^2}\right) + \mathrm{dilog}\left(-\frac{Q^2}{\mu^2}\right) - \mathrm{dilog}\left(-\frac{1}{2}\frac{Q^2}{\mu^2}\right) \\ &\quad - \mathrm{dilog}\left(\frac{m^2}{m^2-Q^2}\right) + \frac{\pi^2}{12} - \frac{1}{2}\,. \end{aligned} \tag{A.93}$$

For large $Q^2 \to \infty$, the leading terms are

$$\begin{aligned} \mathrm{dilog}\left(\frac{Q^2}{m^2}\right) &\sim -\frac{1}{2}\log^2(Q^2)\,, \\ \mathrm{dilog}\left(-\frac{Q^2}{\mu^2}\right) &\sim -\frac{1}{2}\log^2(Q^2) \\ \mathrm{dilog}\left(-\frac{1}{2}\frac{Q^2}{\mu^2}\right) &\sim -\frac{1}{2}\log^2(Q^2) \\ \mathrm{dilog}\left(\frac{m^2}{m^2-Q^2}\right) &\sim \frac{\pi^2}{6} \\ \mathrm{dilog}\left(\frac{m^2}{\mu^2}\frac{Q^2}{m^2-Q^2}\right) &\sim \mathrm{dilog}\left(-\frac{m^2}{\mu^2}\right)\,. \end{aligned} \tag{A.94}$$

In the UR limit all terms but one vanish and we get for the form factor contribution

$$F_1^{\mathrm{ur}\,b}(Q^2,\mu^2) \sim -2\log\left(\frac{Q^2}{\mu^2}\right)\log\left(\frac{Q^2}{m^2}\right)\,, \tag{A.95}$$

to leading order. This term will later cancel the infrared divergence appearing in the bremsstrahlung cross section, so we also need the next to leading order from Eq. (A.93) which becomes important after the cancellation.

Now we calculate the contribution $F_1^c(\mu^2)$ from Eq. (A.72). Taking into account

$x + y + z = 1$ we can perform a trivial integration over x, obtaining

$$\begin{aligned}
F_1^c(\mu^2) &= -\int_0^1 dz \int_0^{1-z} dy \frac{m^2(1-4z+z^2)}{m^2(1-z)^2+\mu^2(1-y-z)} \\
&= \frac{m^2}{\mu^2}\int_0^1 dz(1-4z+z^2)\log\left(\frac{1-z}{1-z+\frac{\mu^2}{m^2}}\right) \\
&= \frac{2}{3}\frac{m^2}{\mu^2}\log\left(\frac{m^2+\mu^2}{m^2}\right)+\frac{1}{3}\frac{\mu^4}{m^4}\log\left(\frac{\mu^2}{m^2+\mu^2}\right)+2\log\left(\frac{m^2+\mu^2}{\mu^2}\right) \\
&\quad +\frac{\mu^2}{m^2}\log\left(\frac{m^2+\mu^2}{\mu^2}\right)+\frac{1}{3}\frac{\mu^2}{m^2}-\frac{7}{6} \\
&= \frac{2}{3}\frac{m^2}{\mu^2}\log\left(1+\frac{\mu^2}{m^2}\right)+\left(2+\frac{\mu^2}{m^2}-\frac{1}{3}\frac{\mu^4}{m^4}\right)\log\left(1+\frac{m^2}{\mu^2}\right) \\
&\quad +\frac{1}{3}\frac{\mu^2}{m^2}-\frac{7}{6} \\
&= 2\log\left(\frac{m^2}{\mu^2}\right)-\frac{1}{2}\,, \qquad \text{(A.96)}
\end{aligned}$$

because finally the photon mass μ will go to zero and thus

$$\frac{m^2}{\mu^2}\log\left(1+\frac{\mu^2}{m^2}\right)\to 1\,. \qquad \text{(A.97)}$$

Now we put together the three contributions to the form factor in the limit where $(Q^2/m^2) \gg 1$. Combining Eqs. (A.71), (A.81), (A.93), and (A.96), we obtain

$$\begin{aligned}
F_1^{\rm ur}(Q^2) &= \frac{\alpha}{2\pi}\Bigg[\frac{1}{2}\log\left(\frac{m^2}{Q^2}\right)-\frac{1}{2}\log^2(2)+\log(2)\log\left(\frac{Q^2}{\mu^2}\right) \\
&\quad -\frac{1}{2}\log^2\left(\frac{Q^2}{\mu^2}\right)-2\log\left(\frac{Q^2}{\mu^2}\right)\log\left(\frac{Q^2}{m^2}\right) \\
&\quad +\log\left(\frac{Q^2}{m^2}\right)+\frac{1}{2}\log^2\left(\frac{Q^2}{m^2}\right)+\log\left(\frac{Q^2}{m^2}\right)\log\left(\frac{\mu^2}{m^2}\right) \\
&\quad +\mathrm{dilog}\left(\frac{Q^2}{m^2}\right)+\mathrm{dilog}\left(\frac{m^2}{\mu^2}\frac{Q^2}{m^2-Q^2}\right)+\mathrm{dilog}\left(-\frac{Q^2}{\mu^2}\right) \\
&\quad -\mathrm{dilog}\left(-\frac{1}{2}\frac{Q^2}{\mu^2}\right)-\mathrm{dilog}\left(\frac{m^2}{m^2-Q^2}\right)+\frac{\pi^2}{12} \\
&\quad +2\log\left(\frac{m^2}{\mu^2}\right)\Bigg]\,. \qquad \text{(A.98)}
\end{aligned}$$

So to leading order only the whole UR form factor is just

$$F_1(Q^2,\mu^2) = -\frac{\alpha}{\pi}\log\left(\frac{Q^2}{\mu^2}\right)\log\left(\frac{Q^2}{m^2}\right)\,, \qquad \text{(A.99)}$$

which clearly cancels the infrared divergence in Eq. (A.122).

In the classical limit in which no momentum Q^2 is transferred (Uehling limit) we obtain

$$\begin{aligned} F_1^{\mathrm{cl}}(Q^2) &= \lim_{Q^2\to 0} F_1(Q^2) \\ &= -3 + \frac{1}{2}\frac{\mu^2}{m^2} + 2\log\left(\frac{m^2}{\mu^2}\right) . \end{aligned} \tag{A.100}$$

Let us now evaluate the other form factor $F_2(Q^2)$. From Eq. (A.65) we get by integrating trivially over x

$$F_2(Q^2) = \frac{\alpha}{2\pi}\int_0^1 dz \int_0^{1-z} dy \frac{2m^2 z(1-z)}{-y(y+z-1)Q^2 + (1-z)^2 m^2} , \tag{A.101}$$

The integration over y yields an arctan function which again can be transformed into a linear combination of logarithms. We obtain

$$F_2(Q^2) = \frac{\alpha}{2\pi}\int_0^1 dz \frac{4m^2 z}{\sqrt{Q^2(Q^2+4m^2)}} \log\left[\frac{Q^2 + \sqrt{Q^2(Q^2+4m^2)}}{-Q^2 + \sqrt{Q^2(Q^2+4m^2)}}\right] . \tag{A.102}$$

Almost all terms containing a z cancel and $F_2(Q^2)$ becomes just

$$F_2(Q^2) = \frac{\alpha}{\pi}\frac{m^2}{Q^2}\frac{1}{\sqrt{1+\frac{4m^2}{Q^2}}} \log\left(\frac{\sqrt{1+\frac{4m^2}{Q^2}}+1}{\sqrt{1+\frac{4m^2}{Q^2}}-1}\right) . \tag{A.103}$$

So in the UR limit this form factor becomes small.

Now that we have a regularized expression for the vertex correction amplitude $\mathcal{M}_{\mathrm{vc}}$ we can calculate its product with the elastic scattering amplitude $\mathcal{M}_{\mathrm{Born}}$,

yielding

$$\begin{aligned}
2\mathcal{M}^{\star}_{\mathrm{vc}}\mathcal{M}_{\mathrm{Born}} &= 2\Bigg[\frac{i2Ze^4}{|\mathbf{q}|^2}\int_0^1 dxdydz\delta(x+y+z-1) \\
&\quad \times\bar{u}(p',s')\Bigg\{\frac{\gamma^0}{2(4\pi)^2}\log\frac{1}{\Delta}+\frac{1}{(4\pi)^2\Delta} \\
&\quad \times\Bigg[(1-x)(1-y)q^2\gamma^0+(1-4z+z^2)m^2\gamma^0 \\
&\quad +\frac{i\sigma^{0\nu}q_\nu}{2m}2m^2z(1-z)\Bigg]\Bigg\}u(p,s)\Bigg]^{\star}\left[\frac{iZe^2}{|\mathbf{q}|^2}\bar{u}(p,s)\gamma^0u(p',s')\right] \\
&= 2\left[\frac{-iZe^2}{|\mathbf{q}|^2}\bar{u}(p,s)\left\{\gamma^0F_1(Q^2)+\frac{i\sigma^{0\nu}q_\nu}{2m}F_2(Q^2)\right\}u(p',s')\right] \\
&\quad \times\left[\frac{iZe^2}{|\mathbf{q}|^2}\bar{u}(p,s)\gamma^0u(p',s')\right]. \qquad \text{(A.104)}
\end{aligned}$$

In (A.104) the terms containing the γ^0 matrix are proportional to the purely elastic scattering processes. The term containing the $\sigma^{0\nu}$ tensor needs some more effort. Let us sum over all spins so that we can move the spinors freely,

$$\begin{aligned}
\frac{1}{2}\sum_{s,s'}2\mathcal{M}^{\star}_{\mathrm{vc}}\mathcal{M}_{\mathrm{Born}} &= \frac{Z^2e^4}{|\mathbf{q}|^4}\sum_{s,s'}\bar{u}(p,s)\left[\gamma^0F_1(Q^2)-\frac{i\sigma^{0\nu}q_\nu}{2m}F_2(Q^2)\right] \\
&\quad \times u(p',s')\bar{u}(p',s')\gamma^0u(p,s) \\
&= \frac{Z^2e^4}{|\mathbf{q}|^4}\Bigg\{\mathrm{tr}[(\not{p}+m)\gamma^0(\not{p}'+m)\gamma^0]F_1(Q^2) \\
&\quad +\frac{1}{4m}\mathrm{tr}[(\not{p}+m)[\gamma^0,\gamma^\nu]q_\nu(\not{p}'+m)\gamma^0]F_2(Q^2)\Bigg\}, \qquad \text{(A.105)}
\end{aligned}$$

because $\sigma^{0\nu}=i/2[\gamma^0,\gamma^\nu]$. The first trace is the one from elastic electron scattering (A.5), the other one yields

$$\mathrm{tr}[(\not{p}+m)[\gamma^0,\gamma^\nu]q_\nu(\not{p}'+m)\gamma^0]=(16m^2-16p'\cdot p)m=8mq^2=-8mQ^2\,. \qquad \text{(A.106)}$$

So for the amplitude product (A.105) we obtain

$$\frac{1}{2}\sum_{s,s'}2\mathcal{M}^{\star}_{\mathrm{vc}}\mathcal{M}_{\mathrm{Born}}=\sum_{s,s'}|\mathcal{M}_{\mathrm{Born}}|^2F_1(Q^2)-\frac{Z^2e^4}{|\mathbf{q}|^4}2Q^2F_2(Q^2)\,. \qquad \text{(A.107)}$$

Combining this with Eq. (A.5) we get

$$\begin{aligned}\frac{1}{2}\sum_{s,s'} 2\mathcal{M}^{\star}_{\mathrm{vc}}\mathcal{M}_{\mathrm{Born}} &= \frac{1}{2}\sum_{s,s'}|\mathcal{M}_{\mathrm{Born}}|^2 2F_1(Q^2) \\ &\quad - \frac{Z^2e^4}{|\mathbf{q}|^4}\frac{2Q^2}{4E^2-Q^2}(4E^2-Q^2)F_2(Q^2) \\ &= \frac{1}{2}\sum_{s,s'}|\mathcal{M}_{\mathrm{Born}}|^2 2\left[F_1(Q^2) - \frac{Q^2}{4E^2-Q^2}F_2(Q^2)\right] .\end{aligned} \tag{A.108}$$

The overall factor of 2 comes from the 2 in the first term of Eq. (A.3).

Now we can write down the vertex correction cross section

$$\left(\frac{d\sigma}{d\Omega_{\mathrm{e}}}\right)_{\mathrm{Born}\times\mathrm{vc}} = \left(\frac{d\sigma}{d\Omega_{\mathrm{e}}}\right)_{\mathrm{Born}} 2\left[F_1(Q^2) - \frac{Q^2}{4E^2-Q^2}F_2(Q^2)\right] . \tag{A.109}$$

This is the contribution to the electron scattering cross section corresponding to the first term in Eq. (A.3).

A.3 The bremsstrahlung cross section

The Bethe-Heitler bremsstrahlung cross section can be found in [97]. As mentioned before it diverges in the limit as the energy ω of the bremsstrahlung photon goes to zero. In SPA the cross section reads

$$\left(\frac{d\sigma}{d\Omega_{\mathrm{e}}}\right)_{\mathrm{brems}} = \left(\frac{d\sigma}{d\Omega_{\mathrm{e}}}\right)_{\mathrm{Born}} \frac{\alpha}{\pi}\int d\omega\omega \int \frac{d\Omega_\gamma}{4\pi}\left[\frac{\epsilon\cdot p'}{k\cdot p'} - \frac{\epsilon\cdot p}{k\cdot p}\right]^2 . \tag{A.110}$$

The divergence is a bit hidden: note that k is proportional to ω, too, and k occurs in the denominators which are then squared. So pulling out all contributions to the energy ω, we see that we actually have to integrate over $d\omega/\omega$, which diverges. In order to kill this divergence we introduce a small photon mass μ which will cancel with the photon mass terms from the vertex correction. We obtain

$$\int_0^{\Delta E}\frac{d\omega}{\omega} \to \int_\mu^{\Delta E}\frac{d\omega}{\omega} = \frac{1}{2}\log\left(\frac{\Delta E^2}{\mu^2}\right) . \tag{A.111}$$

The energy ΔE is the largest energy for which the SPA ansatz employed in Eq. (A.110) still holds. A reasonable upper limit for this energy is $|\mathbf{q}|$.

We perform the integral over the photon angles $d\Omega_\gamma$ by introducing unit three-momentum vectors $\hat{\mathbf{k}} \equiv \mathbf{k}/\omega$, and $\beta \equiv \mathbf{p}/E$, such that the factor in square brackets in Eq. (A.110) becomes

$$\frac{1}{\omega^2}\left[\frac{2(1-\beta'\beta)}{(1-\hat{\mathbf{k}}\cdot\beta')(1-\hat{\mathbf{k}}\cdot\beta)} - \frac{m^2}{E^2(1-\hat{\mathbf{k}}\cdot\beta')^2} - \frac{m^2}{E^2(1-\hat{\mathbf{k}}\cdot\beta)^2}\right]. \quad \text{(A.112)}$$

Here we have employed the relation

$$\sum_{\text{pol.}}[\epsilon\cdot a][\epsilon\cdot b] = -a\cdot b\,, \quad \text{(A.113)}$$

which is for instance proven in [98]. Also, we have made use of the fact that $p^2 = p'^2 = m^2$.

The integral over the photon angles $d\Omega_\gamma$ can easily be done. Integrating the last two terms in square brackets in (A.112) is also easy. For the first term we have to insert Feynman parameters again, finally yielding for the cross section

$$\begin{aligned}\left(\frac{d\sigma}{d\Omega_\mathrm{e}}\right)^{\text{spa}}_{\text{brems}} &= \left(\frac{d\sigma}{d\Omega_\mathrm{e}}\right)_{\text{Born}} \frac{\alpha}{2\pi}\log\left(\frac{\Delta E^2}{\mu^2}\right) \\ &\quad\times\left[2(1-\beta^2)\int_0^1 \frac{dx}{1-\beta^2+4\beta^2\sin^2\frac{\theta}{2}x(1-x)} - 2\right].\end{aligned} \quad \text{(A.114)}$$

Please note that in the SPA limit ($\omega \to 0$) β and β' are the same. The integral can be done and we get

$$\begin{aligned}\left(\frac{d\sigma}{d\Omega_\mathrm{e}}\right)^{\text{spa}}_{\text{brems}} &= \left(\frac{d\sigma}{d\Omega_\mathrm{e}}\right)_{\text{Born}} \frac{\alpha}{2\pi}\log\left(\frac{\Delta E^2}{\mu^2}\right) \\ &\quad\times\left[\frac{-2(1-\beta^2)}{\sqrt{F}}\arctan\left(\frac{\beta^2\sin^2\frac{\theta}{2}}{\sqrt{F}}\right) - 2\right],\end{aligned} \quad \text{(A.115)}$$

where

$$F \equiv (\beta^4-\beta^2)\sin^2\frac{\theta}{2} - \beta^4\sin^4\frac{\theta}{2}\,. \quad \text{(A.116)}$$

There is another way to solve the integral over the photon angles. As most of the bremsstrahlung is radiated along the $\mathbf{p}$ and $\mathbf{p}'$ direction we can apply the peaking approximation. It allows us to split the integral

$$\int\frac{d\Omega_\gamma}{4\pi}\left[\frac{2(1-\beta'\beta)}{(1-\hat{\mathbf{k}}\cdot\beta')(1-\hat{\mathbf{k}}\cdot\beta)} - \frac{m^2}{E^2(1-\hat{\mathbf{k}}\cdot\beta')^2} - \frac{m^2}{E^2(1-\hat{\mathbf{k}}\cdot\beta)^2}\right]. \quad \text{(A.117)}$$

The last two terms vanish in the UR limit and integrating over the angle ϕ we obtain for Eq. (A.117)

$$\int_{-1}^{+1} d\cos\theta \frac{1-\beta'\cdot\beta}{(1-\hat{\mathbf{k}}\cdot\beta')((1-\hat{\mathbf{k}}\cdot\beta)} \,. \tag{A.118}$$

We now split this integral and choose the $\theta = 0$ direction parallel to $\mathbf{p}$ and $\mathbf{p}'$, respectively. The details can be found in [42]. We obtain

$$\begin{aligned} & \int_{\cos\theta=\beta}^{\cos\theta=1} d\cos\theta \frac{1-\beta'\cdot\beta}{(1-\beta\cos\theta)((1-\beta\cdot\beta')} \\ + & \int_{\cos\theta=\beta'}^{\cos\theta=1} d\cos\theta \frac{1-\beta'\cdot\beta}{(1-\beta'\cos\theta)((1-\beta\cdot\beta')} \,. \end{aligned} \tag{A.119}$$

Evaluating the integrals we finally get

$$\begin{aligned} & \log\left(\frac{1-\beta'\cdot\beta}{1-\beta}\right) + \log\left(\frac{1-\beta'\cdot\beta}{1-\beta'}\right) \approx 2\log\left[\frac{p\cdot p'}{(E^2-p^2)/2}\right] \\ = \; & 2\log\left(\frac{Q^2}{m^2}\right) \,. \end{aligned} \tag{A.120}$$

So the UR bremsstrahlung cross section reads

$$\left(\frac{d\sigma}{d\Omega_\mathrm{e}}\right)_\mathrm{brems}^\mathrm{ur-spa} \approx \left(\frac{d\sigma}{d\Omega_\mathrm{e}}\right)_\mathrm{Born} \frac{\alpha}{\pi}\log\left(\frac{\Delta E^2}{\mu^2}\right)\log\left(\frac{Q^2}{m^2}\right) \,. \tag{A.121}$$

and together with the estimate for ΔE^2 in the SPA it becomes

$$\left(\frac{d\sigma}{d\Omega_\mathrm{e}}\right)_\mathrm{brems}^\mathrm{ur-spa} \approx \left(\frac{d\sigma}{d\Omega_\mathrm{e}}\right)_\mathrm{Born} \frac{\alpha}{\pi}\log\left(\frac{Q^2}{\mu^2}\right)\log\left(\frac{Q^2}{m^2}\right) \,. \tag{A.122}$$

List of Figures

List of Tables

Abbreviations

3BF	three-body force
AMEGIC++	*Monte Carlo generator simulating* e^+e^- ISR *experiments*
BABAR	*a* SLAC *experiment studying* $b\bar{b}$ *mesons*
CESR	Cornell electron storage ring
CT	colour transparency
DAϕNE	*ϕ-factory in Frascati, Italy*
DWIA	distorted-wave impulse approximation
EUROGRAD	European graduate college Basel – Tübingen
FSI	final-state interactions
FSR	fina-state radiation
ISR	initial-state radiation
KEK-B	ko-enerugi-kasokuki-kenkyu-kiko B-factory, Japan
LNS	Laboratory for Nuclear Science, U.S.A.
MAMI	Mainz Microtron, Germany
MCEEP	$(e, e'p)$ *data analysis code for* TJNAF*'s hall A*
MEC	meson exchange currents
MIT	Massachusetts Institute of Technology, U.S.A.
MIT-Bates	*Bates Linear Accelerator Center*, U.S.A.
NIKHEF	*The National Institute for Nuclear Physics and High Energy Physics*, NL
NLO	next-to-leading-order
PEP-II	*positron-electron project (2),* SLAC*, U.S.A.*
PHOKHARA	*Monte Carlo generator simulating* e^+e^- ISR *experiments*
pQCD	perturbative quantumchromodynamics
PWIA	plane-wave impulse approximation
QCD	quantumchromodynamics
QED	quantumelectrodynamics
SESAME	Synchrotron-light for Experimental Science and Applications in the Middle East
SPA	soft-photon approximation
SLAC	Stanfor Linear Accelerator, U.S.A.
SRC	short-range correclations
SIMC	$(e, e'p)$ *data analysis code for* TJNAF*'s hall C*

SIMC-SEMI	*a* SIMC *version for* $H(e,e'p)\pi^0$ *experiments*
TJNAF	Thomas Jefferson National Accelerator Facility, U.S.A.
TPE	two-photon exchange *(box and crossed box Feynman diagram)*
UR	ultra-relativistic (limit)

Bibliography

[1] P. E. Ulmer, Proc. of the EEP03 conference, Grenoble, France, 1 (2003)

[2] S. Gilad, Proc. to the '5$^{\text{th}}$ workshop on e-m induced two-hadron emission', Lund (2001), nucl-ex/0108025

[3] L. Lápikas *et al.*, Nucl. Phys. A **663**, 337c (2000)

[4] C. J. G. Onderwater *et al.*, Phys. Rev. Lett. **81**, 2213 (1998)

[5] D. Rohe *et al.* (E97-006 Collaboration), Phys. Rev. Lett. **93**, 182501 (2004)

[6] D. Rohe *et al.*, Eur. Phys. J. A **17**, 439 (2003)

[7] S. Okada *et al.*, Nucl. Phys. A **752**, 196 (2005)

[8] P. E. Ulmer *et al.*, Phys. Rev. Lett. **89**, 062301 (2002)

[9] H. Baghaei *et al.*, Phys. Rev. C **39**, 177 (1989)

[10] L. B. Weinstein *et al.*, Phys. Rev. Lett. **64**, 1646 (1990)

[11] C. M. Spaltro *et al.*, Phys. Rev. C **48**, 2385 (1993)

[12] L. Chinitz *et al.*, Phys. Rev. Lett. **67**, 568 (1991)

[13] J. M. Udías *et al.*, Phys. Rev. C **64**, 024614 (2001)

[14] G. van der Steenhoven, Few-Body Syst. **17**, 79 (1994)

[15] V. R. Pandharipande , I. Sick, P. K. A. deWitt Huberts, Rev. Mod. Phys. **69**, 981 (1997)

[16] W. Zuo, A. Lejeune, U. Lombardo, J. F. Mathiot, Nucl. Phys. A **706**, 418 (2002)

[17] C. Carasco *et al.*, Phys. Lett. B **559**, 41 (2003)

[18] J. L. Friar *et al.*, Phys. Lett. B **311**, 4 (1993)

[19] D. P. Watts (for the PIP/TOF group of the Mainz A2 collaboration), Proc. to the '5$^{\text{th}}$ workshop on e-m induced two-hadron emission', Lund (2001)

[20] S. J. Brodsky, Proc. of the 13$^{\text{th}}$ Int. Symp. on Multi-Particle Dynamics, Volendam, The Netherlands (1982)

[21] K. Garrow *et al.*, Phys. Rev. C **66**, 044613 (2002)

[22] J. Arrington, Phys. Rev. C **68**, 034325 (2003)

[23] G. van der Steenhoven *et al.*, Phys. Rev. Lett. **57**, 182 (1986)

[24] V. Frolov *et al.*, Phys. Rev. Lett. **83**, 4494 (1999)

[25] J. Schwinger, Phys. Rev. **75**, 898 (1949)

[26] L. W. Mo, Y. S. Tsai, Rev. Mod. Phys. **41**, 205 (1969)

[27] C. de Calan, H. Navelet, J. Picard, Nucl. Phys. B **348**, 47 (1991)

[28] L. C. Maximon, J. A. Tjon, Phys. Rev. C **62**, 054320 (2000)

[29] P. G. Blunden, W. Melnitchouk, and J. A. Tjon, Phys. Rev. Lett. **91**, 142304 (2003)

[30] P. A. M. Guichon and M. Vanderhaeghen, Phys. Rev. Lett. **91**, 142303 (2003)

[31] R. R. Lewis, Phys. Rev. **102**, 537 (1956)

[32] S. D. Drell, M. A. Ruderman, Phys. Rev. **106**, 561 (1957)

[33] S. D. Drell, S. Fubini, Phys. Rev. **113**, 741 (1959)

[34] J. A. Campbell, Phys. Rev. **180**, 1541 (1969)

[35] Y. S. Tsai, Phys. Rev. **122**, 1898 (1961)

[36] L. C. Maximon, Rev. Mod. Phys. **41**, 193 (1969)

[37] D. R. Yennie, S. C. Frautschi, H. Tsuura, Ann. Phys. **13**, 379 (1961)

[38] S. N. Gupta, Phys. Rev. **99**, 1015 (1955)

[39] J. A. Templon *et al.*, Phys. Rev. C **61**, 014607 (2000)

[40] R. Ent *et al.*, Phys. Rev. C **64**, 054610 (2001)

[41] F. Bloch, A. Nordsieck, Phys. Rev. **52**, 54 (1937)

[42] M. E. Peskin, D. V, Schroeder, *An Introduction to Quantum Field Theory*, Addison-Wesley (1995)

[43] L. I. Schiff, Phys. Rev. **87**, 750 (1952)

[44] L. C. Maximon, D. B. Isabelle, Phys. Rev. **133** B, 1344 (1964)

[45] L. C. Maximon, D. B. Isabelle, Phys. Rev. **136** B, 764 (1964)

[46] A. Afanasev, I. Akushevich, N. Merenkov, Phys. Rev. D **64**, 113009 (2001)

[47] A. Afanasev, I. Akushevich, A. Ilyichev, N. P. Merenkov, Phys. Lett. B **514**, 269 (2001),

[48] A. Afanasev, I. Akushevich, A. Ilyichev, B. Niczyporuk Czech. J. Phys. **53**, B449 (2003)

[49] M. Vanderhaeghen *et al.*, Phys. Rev. C **62**, 025501 (2000)

[50] J. Arvieux *et al.*, Eur. Phys. J. A **26**, 429 (2005)

[51] D. S. Armstrong *et al.*, Phys. Rev. Lett. **95**, 092001 (2005)

[52] J. Küblbeck, M. Böhm, A. Denner, Comp. Phys. Comm. **60**, 165 (1990) `feyncalc` package available at `www.feyncalc.org`

[53] J. Arrington, SIMC 2001 release, TJNAF

[54] G. 't Hooft, Nucl. Phys. B **61**, 455 (1973)

[55] P. E. Ulmer, MCEEP, release 3.8, TJNAF

[56] E. Borie, D. Drechsel, Nucl. Phys. A **167**, 369 (1971)

[57] E. Borie, Z. f. Naturforschung, **30a**, 1543 (1975)

[58] L. D. Landau, E. M. Lifshitz, *Quantenelektrodynamik*, Akademie-Verlag Berlin (1986)

[59] Hall C Physics Vade Mecum; J. Arrington, *A-B-SIMC*, TJNAF (2001)

[60] H. Czyz, J. H. Kühn, E. Nowak, G. Rodrigo, Eur. Phys. J. C **35**, 527 (2004)

[61] M. N. Rosenbluth, Phys. Rev. **79**, 615 (1950)

[62] M. K. Jones *et al.* (Jefferson Lab Hall A collaboration), Phys. Rev. Lett. **84**, 1398 (2000)

[63] O. Gayou *et al.* (Jefferson Lab Hall A collaboration), Phys. Rev. Lett. **88**, 092301 (2002)

[64] R. Segel *et al.*, (Jefferson Lab E01-001 collaboration), Eur. Phys. J. A **24**, 1.55 (2005)

[65] I. A. Qattan *et al.*, Phys. Rev. Lett. **94**, 1142301 (2005)

[66] `http://quasar.physik.unibas.ch/~fwb/thesis/fig52.pdf`

[67] J. Litt *et al.*, Phys. Lett. B **31**, 40 (1970)

[68] W. Bartel *et al.*, Nucl. Phys. B **58**, 429 (1973)

[69] R. C. Walker *et al.*, Phys. Rev. D **49**, 5671 (1994)

[70] L. Andivahis *et al.*, Phys. Rev. D **50**, 5491 (1994)

[71] L. E. Price *et al.*, Phys. Rev. D **4**, 45 (1971)

[72] Ch. Berger *et al.*, Phys. Lett. B **35**, 87 (1971)

[73] I. A. Qattan *et al.*,Phys. Rev. Lett. **94**, 142301 (2005)

[74] F. Borkowski *et al.*, Nucl. Phys. B **93**, 461 (1975)

[75] K. M. Hanson *et al.*, Phys. Rev. D **8**, 753 (1973)

[76] M. E. Christy, Phys. Rev. C **70**, 015206 (2004)

[77] P. G. Blunden, W. Melnitchouk, and J. A. Tjon, Phys. Rev. C **72**, 034612 (2005)

[78] S. Kondratyuk, P. G. Blunden, W. Melnitchouk, J. A. Tjon, Phys. Rev. Lett. **95**, 172503 (2005)

[79] I. Sick and D. Trautmann, Phys. Lett. B **375**, 16 (1996)

[80] I. Sick, Phys. Lett. B **576**, 62 (2003)

[81] R. Rosenfelder, Phys. Lett. B **479**, 381 (2000)

[82] J. Arrington, Phys. Rev. C **69**, 022201 (2004)

[83] `http://quasar.physik.unibas.ch/~fwb/thesis/fig53.pdf`

[84] The world form factor data for the space-like form factors of the nucleons and the full list of references can be found at:
`http://www.jlab.org/~cseely/nucleons.html`.

[85] S. Kondratyuk, P. G. Blunden, nucl-th/0601063 (2006)

[86] E. Tomasi-Gustafsson, G. I. Gakh, Phys. Rev. C **72**, 015209 (2005)

[87] V. Tvaskis *et al.*, Phys. Rev. C **73**, 025206 (2006)

[88] Y. C. Chen *et al.*, Phys. Rev. Lett. **93**, 122301 (2004)

[89] A. Afanasev *et al.*, Phys. Rev. D **72**, 013008 (2005)

[90] M. Guidal, M. V. Polyakov, A. V. Radyushkin, M. Vanderhaeghen, Phys. Rev. D **72**, 054013 (2005)

[91] P. E. Bosted, Phys. Rev. C **51**, 409 (1995)

[92] M. Jones, private communication (2005)

[93] J. H. Kühn, Eur. Phys. J. C **33**, 659 (2004)

[94] B. Aubert *et al.* (BABAR collaboration), Phys. Rev. D **73** 012005 (2006)

[95] The code and a manual is available at:
`http://grodrigo.home.cern.ch/grodrigo/phokhara/`.

[96] A. Schälicke, F. Krauss, R. Kuhn, and G. Soff, J. High Energy Phys. **12**, 013 (2002)

[97] C. Itzykson, J.-B. Zuber, *Quantum Field Theory*, McGraw-Hill (1980)

[98] J. D. Bjørken, S. D. Drell, *Relativistic quantum fields*, McGraw-Hill (1965)